8-24-2021 9:30 AM

Stochastic Source Modelling and Tsunami Analysis of the 2012 Mw 7.8 Haida Gwaii Earthquake

Karina Martinez Alcala, *The University of Western Ontario*

Supervisor: Goda, Katsuichiro, *The University of Western Ontario*
Joint Supervisor: Mora-Stock,Cindy, *The University of Western Ontario*

A thesis submitted in partial fulfillment of the requirements for the Master of Science degree in Geophysics

Recommended Citation
Martinez Alcala, Karina, "Stochastic Source Modelling and Tsunami Analysis of the 2012 Mw 7.8 Haida Gwaii Earthquake" (2021). *Electronic Thesis and Dissertation Repository*. 8145.
https://ir.lib.uwo.ca/etd/8145

Abstract

The Mw 7.8 2012 Haida Gwaii Earthquake triggered a tsunami that highlighted the importance of tsunami hazard assessment on Canada’s Pacific coast. Stochastic source modelling serves as a valuable method to assess future tsunami hazard and has not been performed for this region. The source models characterize the uncertainty of earthquake ruptures by considering variability in fault geometry and slip heterogeneity, which, in turn, allows the consideration of a wide range of tsunami scenarios in the Haida Gwaii region. The model predictions are constrained by observational data and past source inversion studies. One hundred twenty-eight stochastic tsunami scenarios are generated using the stochastic source modelling method to assess tsunami hazard via tsunami inundation simulations of the target region and conduct sensitivity analyses of tsunami height variability. The resulting models can promote better-informed risk management decisions and future probabilistic tsunami hazard analysis in this region.

Keywords

Stochastic source modelling, stochastic models, tsunami hazard, Monte Carlo tsunami simulation, 2012 Haida Gwaii earthquake, tsunamis, slip distributions

Summary for Lay Audience

On October 28, 2012, an Mw 7.8 earthquake hit the region of Haida Gwaii, Canada. The tsunami triggered by the earthquake was recorded across the Pacific Ocean. Horizontal and vertical deformations were obtained months after the earthquake and, during post event field surveys, run-up levels were measured at several locations within the rupture zone. This study conducts a tsunami analysis of the Haida Gwaii region using stochastic source modelling and performs Monte Carlo tsunami simulation to develop source models that generate tsunami waves in close match with the recorded observations. The developed stochastic earthquake source model can be applied to evaluate tsunami hazards due to future tsunamigenic events in Haida Gwaii. The methodology encompasses the wavenumber analysis of six existing earthquake slip models to define a generic fault model for the synthetic slip source generation. The stochastic source parameters are based on earthquake source scaling relations derived from global models. The stochastic method uses spectral synthesis, where key slip characteristics are specified in slip statistics, slip distribution parameters, and asperity areas. For a given set of stochastic synthesis parameters, slip distributions are generated by a Fourier integral method. The derived stochastic models can capture realistic asperity zones and source parameters close to those of the 2012 event. Asperity zones are mainly located on the shallow ocean side of the fault, which is consistent with the epicentre location constrained by seismic and deformation data. Consequently, simulated tsunami waves at different stations show that first wave amplitudes are in agreement with the observations. Simulated tsunami run-ups are generally consistent with those observed at sites sheltered from storm waves, with differences ranging from 0.5–3 m. In contrast, the differences become significant at sites exposed to storm waves with a discrepancy of up to 7 m. The discrepancy may be attributed to the possibility that run-up survey observations at exposed bays might include effects due to major storm events that hit Haida Gwaii between the earthquake and the survey. Moreover, source parameters and models that are calibrated for the 2012 event can be adopted to evaluate tsunamis due to future large events in the region.

Co-Authorship Statement

The present thesis, along with the MATLAB codes used in the research were done in co-authorship with Dr. Katsuichiro Goda. Dr. Goda provided feedback on all thesis chapters as well as provided the base MATLAB codes used for the synthesis of stochastic models and tsunami simulations.

Acknowledgments

I want to express my deep gratitude to my supervisor Dr. Katsuichiro Goda for his support and guidance, as well as, the time and effort he put into helping me develop the computer codes needed for the research and revising my thesis. This project could not have been accomplished without his help and dedication. It has been a true honour to be your student.

To my co-supervisor, Cindy Mora-Stock, and the research group, Yusong Yang and Elisa Dong, who listened to my presentations and gave me ideas for improvement, thank you for your extensive help. A special gratitude goes to Payam Momeni; without your countless guidance, patience, and encouragement, this thesis would not have been completed. I am forever grateful to your help.

I also want to thank the three members of my thesis committee, Dr. Schincariol, Dr. Assatourians, and Dr. McBean, for taking the time to read my thesis and provide useful comments for improvement.

I want to extend my thanks to SHARCNET and Ocean Networks Canada for their continued support to Dr. Goda and the rest of the research group.

To my friends Rhys Paterson, Melissa Contreras, Gerardo Garay, and Pedro Ibarra thank you for being by my side and always believing in me even when I didn't. You have been a genuine emotional support throughout this journey.

Finally, to my family and partner. There are no words to express how grateful and in debt I am with you. Mom and Dad, thank you for all your sacrifices that have allowed me always to reach my dreams. This accomplishment is yours. Cruz Estrella, thank you for always being there for me, the countless words of encouragement, the immense support, and for constantly pushing me to be better; without you, I couldn't have started this Master’s.

Table of Contents

List of Tables

List of Figures

List of Appendices

Chapter 1

1 Introduction

Tsunamis, a combination of two Japanese words translated in English as ‘wave in harbour,’ are a series of water waves caused by seismic activities, landslides, and volcanic eruptions. Earthquakes are the principal source of tsunamis and cause the largest wave amplitudes (Leonard et al., 2014). During an earthquake rupture, tsunamis are generated by transforming large-scale elastic deformation to potential energy within the water column (Levin & Nosov, 2009). The initial dislocation of a large volume of water then propagates spatially due to gravity. During this process, a large amount of water is displaced and eventually causes substantial flooding along coastlines. Thus, making tsunamis one of the most destructive and deathly phenomena (Bernard & Titov, 2015). Coastal flooding is caused by a shoaling process in which, as the tsunami approaches the coast, the wave propagation speed decreases while the tsunami height increases. The increase in the tsunami’s height is because the wave’s amplitude is a function of the propagation velocity, which depends on depth. On the other hand, the tsunami wave loses its energy due to bottom friction and turbulence.

Historical records show that tsunamis have had a significant socio-economic impact on human history, as evidenced major destruction of coastal communities. Recent significant tsunami events have also reminded us of the importance of tsunami hazard assessment, particularly in highly populated coastal areas. For example, the 2004 Indian Ocean mega-thrust earthquake of moment magnitude (Mw) 9.3 triggered a massive tsunami that reached a maximum run-up of 30 m (Titov et al., 2005; Wang & Liu, 2006). This tsunami left hundreds of thousands of deaths and billions of dollars in damages across 19 countries. The lack of proper risk management decisions and early-warning system made the 2004 Indian Ocean earthquake and tsunami one of the most devastating natural disasters in human history (Ghobarah et al., 2006). This catastrophe prompted scientists and engineers to design better early warning systems and develop new tsunami analysis techniques. The most recent major event, the 2011 Tohoku earthquake and tsunami in Japan, left more than 19,000 fatalities and hundreds of billions of dollars in damages (Takabatake et al., 2019).

This event highlighted another issue in tsunami hazard assessment, the difficulty of assessing the characteristics of future events. The Tohoku event was extreme because the actual event was greater than what scientists and engineers previously thought this subduction zone could generate. Therefore, the tsunami scenarios considered when preparing the 2005 Japanese tsunami hazard maps were smaller, significantly underestimating the tsunami hazard. An example was Iwate Prefecture of Japan, where more than 65% of the casualties were outside the major inundation zones (Goda & Song, 2016). The uncertainty of future events affects risk management decisions, which could ultimately fail to prevent major devastation and significant human casualties.

The western coast of North America is at risk of potential earthquakes and tsunamis. The tsunami hazard is significantly higher in the Cascadia and Haida Gwaii region (Figure 1.1). In the north, the Haida Gwaii region is located on a plate boundary between the North American and Pacific Plates known as the Queen Charlotte Fault (QCF). The QCF is characterized by its primary right-lateral shear in its northernmost part (Brothers et al., 2020). The largest instrumentally recorded earthquake in Canada occurred in this region (i.e. 1949 Mw 8.1 Queen Charlotte earthquake; Figure 1.1), and several other major earthquakes of Mw>7 struck the region (i.e. 1899 Mw 8 Yakutat earthquake, 1958 Mw 7.7 Lituya earthquake, 1972 Mw 7.5 Sitka earthquake, 2013 Mw 7.5 Craig earthquake; Szeliga, 2013; Cassidy et al., 2014). The southern part of the QCF is characterized by a convergent component which resulted in the 2012 Haida Gwaii earthquake. Several tectonic models have been suggested for the evolution and mechanics of this part of the QCF. Hyndman (2015) suggested that the convergence is accommodated by a subduction of the Pacific Plate under the North American Plate. In contrast, other models suggest a partitioning of the slip-motion on the QCF and convergent deformation on thrust and reverse faults in Queen Charlotte Terrace (QCT; Tréhu et al., 2015, Brothers et al., 2020).In short, Haida Gwaii is the most seismically active zone on the western coast.

South of the triple junction among the North American, Pacific, and Juan de Fuca Plate, the Cascadia Subduction Zone (CSZ) exists. The CSZ results from the convergence of the North American Plate onto the Juan de Fuca Plate and extends 1100 km along the coastal margin from Vancouver Island, Canada, to the Mendocino Escarpment, northern

California, United States. The CSZ poses a triple seismic threat. Firstly, the subduction earthquakes from the Juan de Fuca-North American convergence. Secondly, from the faults in the overriding North American Plate. Lastly, from the intersection of the subduction zone with the Mendocino transform fault on the San Andreas Fault in the south and the QCF in the north (Petersen, 2002; Atwater et al., 2015). The CSZ is known to rupture in great Mw 8-9 thrust earthquakes with a recurrence period between 100 to 800 years (Goldfinger, 2012), the last one being the 1700 Mw 9 event. Thus, the subduction zone has the potential to rupture in a mega-thrust subduction earthquake with an imminent threat of a tsunami, which would cause extensive damage to highly populated zones along the Pacific coast.

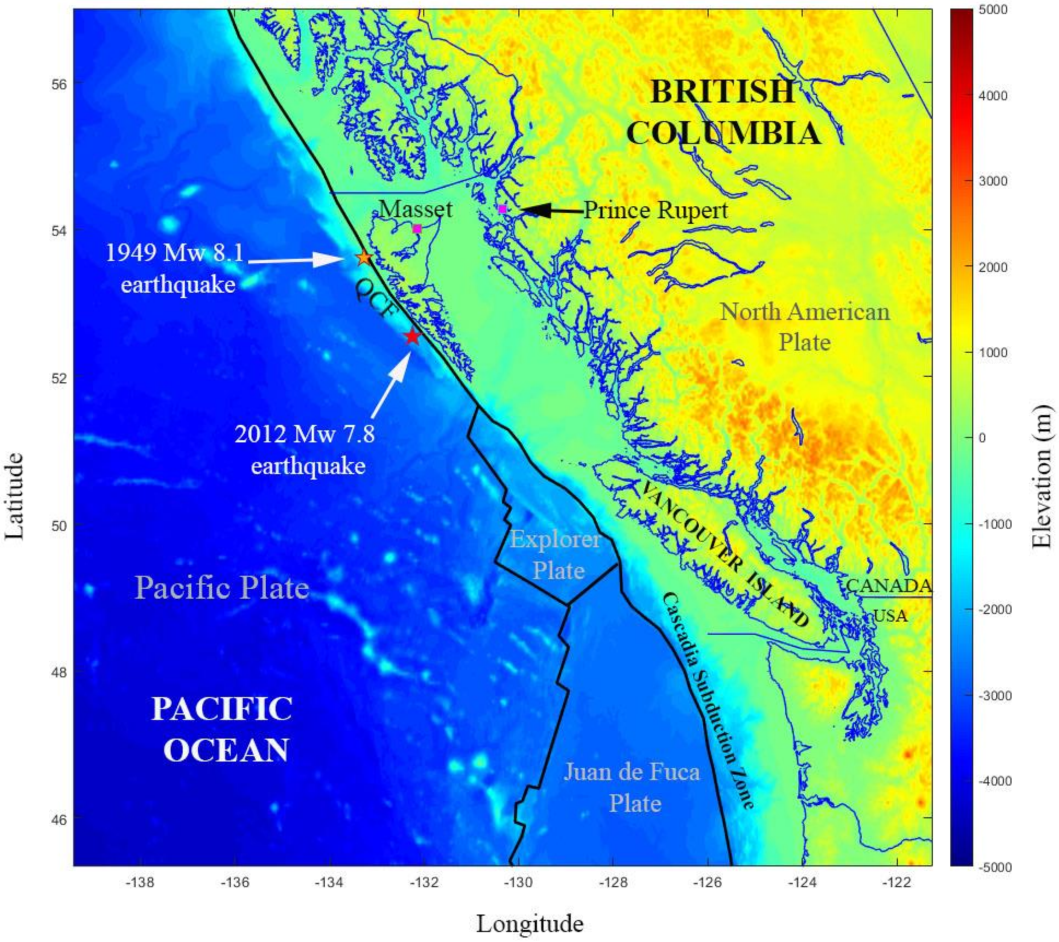

Figure 1.1 Haida Gwaii region on the Pacific Ocean northwest, showing epicentre of the largest earthquakes in the zone (red and orange stars). The locations of the longest ground motions are also shown (pink rectangle).

Although Haida Gwaii is not a highly populated area, earthquakes and tsunamis produced in the region can provide a valuable case study. It can help scientists and engineers better understand the hazard and potential risks of similar or much larger earthquakes and tsunamis in the CSZ (Leonard & Bednarski, 2014). Therefore, the geophysical and geological information from the QCF past events can help validate forecasting models for CSZ future events since the zone lacks information on past earthquakes (Leonard et al., 2014). Tsunami hazard assessment in the Pacific's northwest is critical because of the development that has taken place in coastal communities. This development makes the social and economic impact of future tsunami events more severe than in the past. Therefore, it is crucial to plan and assess for future scenarios. Furthermore, such assessments will inform communities of inundation zones and possible hazards (Bernard & Titov, 2015). Consequently, making the Haida Gwaii region an interesting and important zone for research.

Tsunami inversion and simulation studies are essential for enhancing tsunami preparedness in vulnerable regions. The information used in these models can constrain potential rupture geometry and recurrence rate of future events, which can be used to simulate tsunami propagation and inundation. This information can then help produce tsunami hazard maps for coastal communities (Geist, 2005). However, one of the biggest challenges in tsunami hazard assessment is accurately predicting the occurrence and properties of future events (Goda et al., 2014, Goda & Song, 2016). In tsunami analysis, many sources of uncertainty arise (Geist, 2005; Mueller et al., 2015; Goda & Song, 2016). During the tsunami generation, the uncertainties include the location, occurrence, the downdip rupture extent, fault rupture velocity, rock's shear modulus in the subduction zone, fault geometry, magnitude, and slip distribution (Suppasri et al., 2010, Goda et al., 2014, Mueller et al., 2015). The most important property is the earthquake slip because it significantly influences earthquake ground motions and tsunami propagation and inundation (Satake et al., 2013, Goda & Song, 2016). In tsunami propagation and inundation, factors, such as dispersion of wave propagation, bottom friction, Coriolis force, tides, wave equations, and variability in run-up (Dao & Tkalich, 2007, Løvholt et al., 2012, Mueller et al., 2015), influence the accuracy of the tsunami simulations. Therefore, by including uncertainties in tsunami generation, propagation and inundation, the model complexity increases, which in turn increases the need for high-quality data. More detailed bathymetry and digital elevation models (DEM) could reduce error margins in tsunami simulations, making it possible to have a better tsunami hazard assessment (Mueller et al., 2014, Fine et al., 2018).

For the 2012 Mw 7.8 Haida Gwaii tsunami, multiple studies have been carried out in the past decade. Lay et al. (2013) analyzed the interplate earthquakes of the QCF region and the aftershock sequence of the 2012 event. The study used teleseismic broadband P waves, shear waves with displacement in the horizontal plane (SH), short-period projections, and tsunami observations to determine the coseismic slip distribution and slip partitioning. Nykolaishen et al. (2015) revised the source model of Lay et al. (2013) based on GPS data by shifting the earthquake source. Shao & Ji (2012) and Wei (2012) used teleseismic P-waves and SH waves for their inversion models. However, in both studies, the tsunami sources were too close to the shoreline of the Haida Gwaii Islands, and the source models were not consistent with deformation observations. Fine et al. (2015) studied the near-field characteristics of the 2012 tsunami on the coasts of British Columbia, using a "fast-track" numerical tsunami model by referring to the inversion model by Hayes (2013). The model was constrained using the observations from bottom pressure sensors and some DART stations, and the source location of Hayes (2013) was revised to match the GPS observations by Nykolaishen et al. (2015). Gusman et al. (2016) used a new data assimilation method and compared it against a traditional tsunami forecasting method to evaluate the performance of both approaches to deliver timely and accurate forecasting on the nearby coast. The models accurately matched the tsunami observations of the 2012 earthquake, and both methods were reliable for tsunami forecasting. However, one drawback of the model is the large resolution of the subfaults in the inversion model; having larger subfault areas limits the resolution in which the models can go into during tsunami simulations and their usage for other types of studies such as fragility analysis.

It is important to note that no study has carried a stochastic source modelling methodology to constrain the asperity and source parameters of the region, nor generated models that could match as many observations as possible. The previous studies did not quantify variability and uncertainty associated with source parameters nor with tsunami forecasting. These are the main objectives of this thesis and constitute the novelty of the thesis. The quantified variability is helpful for the prediction of future scenarios for which no observations are available.

1.1 Objectives

The thesis aims to carry stochastic source modelling to constrain possible source scenarios for the 2012 Haida Gwaii tsunami by taking into account the variability and uncertainties of the source region. Then a Monte Carlo tsunami simulation is carried out to validate if the stochastic source models generate realistic tsunami waves similar to those of the 2012 event. Furthermore, using the constraints and validation that the stochastic source models can produce realistic events, the forecasting tsunamis for larger events in the zone is performed by examining the tsunami amplitudes and wave time arrivals. A summary of the objective is as follows and involves four tasks:

1. Develop stochastic slip models for the 2012 Haida Gwaii earthquake using a spectral synthesis approach.

2. Run Monte Carlo tsunami simulations and compare the results with existing observations (tide gauges, DART buoys, ONC BPRs, and vertical and horizontal deformations).

3. Evaluate the earthquake slip and fault geometry effects by analyzing near-shore tsunami heights along the Haida Gwaii coast.

4. The previous tasks are repeated to generate future Mw 8 tsunami scenarios.

1.2 Thesis Structure

This thesis consists of five chapters on stochastic source modelling and tsunami simulations to understand the tsunami hazard off Haida Gwaii’s coast and provide better knowledge of future events in the region. The chapters are organized as follows:

Chapter 1 summarizes the objectives of the thesis and introduces the Haida Gwaii region. A summary of the region’s tectonics is given to understand better the processes involved during the 2012 Haida Gwaii event and possible future events.

Chapter 2 provides a broad overview of key concepts and techniques in earthquake source modelling, tsunami simulation, and tsunami forecasting. The chapter describes available approaches in the literature, highlighting their merits and demerits. This chapter introduces key concepts that are used in this thesis.

Chapter 3 presents the analyses of the 2012 Haida Gwaii earthquake. First, an overview of the 2012 Haida Gwaii event and the key observations recorded during and after the earthquake. Then inversion models from the literature are analyzed. Next, the methodologies used in this study are explained in detail. Based on the characteristics of inversion models, a generic fault model for stochastic modelling is developed. Subsequently, stochastic models are synthesized using statistical scaling relationships and implemented in a Monte Carlo tsunami simulation. Finally, results are analyzed and compared with the observations. The chapter’s primary goal is to link observations to parameters in stochastic source modelling and tsunami simulation.

In Chapter 4, the parameters constrained in Chapter 3 are used to develop stochastic models for possible future Mw 8 events in the zone. The same methodology as Chapter 3 is used. First, a new asperity zone is set up using the synthetic fault and then new stochastic source models are generated to carry the Monte Carlo simulation. Finally, the tsunami waves produced by the models are analyzed.

In Chapter 5, the main conclusions from this thesis are discussed. Then, the limitations of the present study are mentioned, and possible improvements for future studies are explained. Finally, a discussion of possible future work is presented.

Chapter 2

2 Overview of Principal Concepts and Techniques for Stochastic Source Modelling and Tsunami Simulation

Tsunami simulation is a complex process involving tsunami generation, propagation, and inundation along the coast. It is an essential tool in the forecasting and mitigation of tsunami hazards and can help decrease human and economic losses. There are various methodologies in which this can be achieved.

There are two methods for tsunami hazard assessments. The first is based on the largest tsunami event or 'worst-case scenario' (i.e. Heidarzadeh et al., 2009) and might be a relatively conservative approach. This method uses the maximum plausible earthquake and tsunami. It is favoured for early warning, short-term forecast, tsunami mitigation measures, and evacuation planning because the rupture length and displacement are based only on the moment magnitude (Heidarzadeh et al., 2009, Leonard, 2010). However, a significant drawback is that it focuses on a single or a few scenarios. Therefore, the probability for this 'worst-case scenario' to happen is small and is difficult to quantify (Mori et al., 2018).

Furthermore, the method has fewer computational requirements as it does not need the simulation of hundreds of rupture scenarios. It often adopts a simple first-order approximation model with a uniform (homogenous) average slip distribution over a rectangular fault plane (Blaser et al., 2010, Leonard, 2010, An et al., 2018). However, by having a uniform slip, the tsunami's potential energy is underestimated, and the tsunami amplitudes might be underpredicted, which are the most crucial factor in tsunami forecasting (Melgar et al., 2019, Nakata et al., 2019). Additionally, the models do not represent real earthquake kinematics and dynamics. This simplification of the slip adds to the uncertainty of the event since the earthquake source characteristics might not be constrained effectively, affecting the tsunami inundation and run-up simulations, making it challenging to convey the risk and damage to coastal communities adequately.

The second method is probabilistic. It evaluates the probabilistic tsunami characteristics, such as tsunami wave heights and inundation extent (Selva et al., 2016, Mori et al., 2018).

There are three approaches to this method. First is the historical approach, which uses historical records from past earthquakes to constrain possible future scenarios. However, historical records might not be available or sufficient to develop a credible model. The second is a logic-tree approach based on weighted slip conditions and slip scenarios based on expert opinions and historical records (Leonard et al., 2014, Park et al.,2017). Finally, the third is the random phase approach. In this case, a suite of stochastic models with areas on the fault with increased friction (i.e. asperities; Løvholt et al., 2012, Goda et al., 2014, Mueller et al., 2014, Davies et al., 2015) are generated using a slip wavenumber spectrum (e.g. von Karman correlation function) with random phases. The asperities typically cause higher vertical displacements and thus higher initial tsunami amplitudes. Therefore, the definition of asperity zones is necessary because source characteristics significantly influence earthquake ground motion and tsunami propagation (Frankel et al., 2019). The source models are constrained by available scientific evidence of past events and the likelihood of the events occurring (Geist, 2005, Melgar et al., 2019).

Although the use of known earthquake scenarios can constrain some of the uncertainty in tsunami analysis, there is considerable uncertainty about the observational data, how the next earthquake could unfold compared to previous events and the model outcomes (Walsh et al., 2000, Griffin et al., 2017, Lapusta et al., 2019). Therefore, quantifying the uncertainties inherent in earthquake characteristics is essential for robust interpretation, particularly in fault areas with limited observations, such as subduction-zone forearcs and seismogenic zones (Lapusta et al., 2019). Consequently, rather than determining a single preferred model with a chosen set of physical properties that match the observations, a set of models with a range of probable physical properties that fit the observations would be more informative and would incorporate uncertainties by considering errors in the modelling process (Goda et al., 2014, Lapusta et al., 2016).

Stochastic earthquake models based on spectral analysis of slip heterogeneity and spectral synthesis of random slip fields (Mai & Beroza, 2002) can generate multiple possible scenarios with different earthquake slips and fault geometry using synthetic fault models. Thus, by including multiple source scenarios, the stochastic source models can capture the uncertainties associated with earthquake source properties for future events (Goda et al., 2014, Goda & Song, 2016, Sanchez-Linares et al., 2016). This approach, combined with Monte Carlo tsunami simulations, is desirable in developing effective tsunami risk reduction strategies. It promotes informed decisions by communicating the uncertainty of hazard predictions and the consequences in different scenarios (Goda & Song, 2016, Mori et al., 2017b).

This chapter is organized as follows. First, an overview of earthquake source modelling is given, and the steps in the process are explained. Second, an explanation of how stochastic source modelling can be used in earthquake source characterization and its advantages are given. Third, explanations of tsunami simulations and how tsunami generation, propagation, and inundation are calculated are given.

2.1 Earthquake Source Modelling

One of the major uncertainties and challenges in tsunami simulation analysis is predicting source characteristics, such as location, magnitude, geometry, and slip distribution of future tsunamigenic events (Mori et al., 2018, Melgar et al., 2019). These uncertainties are originated from the resolution and coverage of present data, non-uniqueness of the inversion processes, and lack of data (Lapusta et al., 2019). Furthermore, tsunami generation, propagation, and inundation processes are not easy to quantify based on limited knowledge of the rupture zone and due to inevitable variability of future events (Goda & Song, 2016). Therefore, it is vital to develop earthquake source models that integrate all available knowledge about the rupture zone, such as field observations, fault characteristics and major past events (Mori et al., 2018). The first step in developing earthquake source models is to find appropriate scaling relations that capture the structural complexities of the fault and earthquake processes (Lapusta et al., 2019). Then, the scaling relationships are used to develop the source parameters, such as length, width, slip, and correlation lengths.

These scaling relationships define uncertain earthquake source characteristics in tsunami hazard assessment and help characterize earthquake models for future events (Goda et al., 2016). Therefore, the relations need to (1) clearly define the spatial scales of fault slip or other kinematic variables, (2) identify the physical mechanisms, and (3) capture the coupled effects in formulated relations (Lapusta et al., 2019). Wells & Coppersmith (1994) derived scaling relationships based on a large dataset, especially for crustal events. However, they did not include thrust faulting events in subduction zones. Mai & Beroza (2002) developed scaling relationships for slip distribution by analyzing 44 finite-fault models and modelling the wavenumber spectra using von Karman, Gaussian, exponential, and fractal models. They found that the von Karman autocorrelation function was the most consistent with the data and that parameters, such as correlation length along-strike and downdip, correlate with source dimension and earthquake size, which can be used to generate scenario earthquakes for ground motion simulations. The study focused on non-tsunamigenic crustal events of magnitudes of up to 8. Blaser et al. (2010) analyzed 283 earthquakes, mainly focused on subduction-zone events to develop scaling relationships. They used orthogonal regression to account for epistemic uncertainties. However, recent major events were not included in the study. Strasser et al. (2010) also focused on subduction-zone environments and developed scaling relationships between rupture area, length, width, and moment magnitude. Leonard et al. (2010) develop scaling relations that are self-consistent in which the parameters are estimated from each other and are consistent with the seismic moment. However, these relationships do not characterize heterogeneous slip distributions. Murotani et al. (2013) developed scaling relationships by focusing on seven Mw 9 subduction-zone earthquakes; however, they only used Japanese earthquake data for smaller Mw events. Finally, Goda et al. (2016) analyzed finite rupture models compiled in the SRCMOD database (Mai & Thingbaijam, 2014). They evaluated various source parameters to develop scaling relationships for earthquake source parameters, such as fault area, width, length, mean slip, maximum slip, Box-Cox power, correlation lengths along-dip and along strike, and Hurst number. These scaling relationships are helpful for multivariate probabilistic models as they statistically evaluate the variability and dependency of multiple source parameters. The source parameters are then useful for synthesizing realistic stochastic earthquake source models that can be applied in probabilistic tsunami hazard and risk assessments.

The second challenge in earthquake source modelling is to develop computational approaches (i.e. earthquake source simulations) that can solve the time evolution and spatial distributions of the slip/deformation, stresses, and other phenomena (Lapusta et al., 2019). For example, dynamic rupture simulations have been used to study large earthquake ruptures and focus on the fault's rupture propagation and initial conditions. The simulations adjust the fault parameters to match the predicted and observed ground motion records and provide constraints on coseismic stress changes, rupture velocity, and released energy (Lapusta et al., 2019). The resulting models offer insight into the physics of the rupture and slip processes (Oglesby & Day, 2002). However, it requires a complete description of the initial conditions of the fault, which is challenging to constrain with observations because the fault’s characteristics are not entirely known, and the analyses must be based on physical assumptions (Lapusta et al., 2019). Another drawback is that it is challenging to implement and computationally demanding (Causse et al., 2013). Another example is kinematic rupture simulations, which use slip boundary conditions and require implementing the spatio-temporal evolution of slip on the fault during an earthquake (Schmedes et al., 2013).

The third challenge is determining relevant mechanisms and parameters by interpreting the models compared to field observations (i.e., seismic, paleoseismic, geodetic, and geologic data; Lapusta et al., 2019). These field observations provide important information about the earthquake source behaviour. Therefore, models that can reproduce a wide range of observations help discriminate between relevant and irrelevant model parameters (i.e. Goda et al., 2017b).

Finally, the fourth challenge is having models that incorporate the uncertainties involved in forecasting potential future events and earthquake source modelling. Since the last major tsunami events (e.g. 2011 Mw 9 Tohoku tsunami), there has been a particular interest in the robustness of tsunami simulations and the inclusion of uncertainties in the simulated models (Goda et al., 2014, Mori et al., 2017b).

2.2 Stochastic Source Models

In tsunami simulations, earthquake slip is a complex parameter because it is governed by the fault’s pre-rupture stress conditions, geometry, and frictional properties that sometimes are not completely understood. The impact of heterogeneous earthquake slip in tsunami inundation (Geist & Dmowska, 1999) has been increasingly relevant in recent studies (Løvholt et al., 2012, Goda et al., 2014, 2015, Mueller et al., 2015, Davies et al., 2015, Mori et al., 2017b). The focus has been put on the generation of source models that can represent multiple future rupture scenarios with different earthquake slip distributions and fault geometry, and that can capture the uncertainties and variability associated with earthquake source properties and tsunami generation and propagation (Geist & Oglesby, 2014, Goda et al., 2014, Griffin et al., 2017, Mori et al., 2017a). Frequently, the slip distributions are obtained as a set of slip vectors over multiple sub-rupture sources. Stochastic earthquake source models facilitate this process by generating multiple source models with different characteristics that do not require expert judgement (Mori et al., 2018). The input parameters for source models depend on the specific study and the availability and quality of the observations.

Studies have shown that the stochastic method based on spectral random-phase synthesis (e.g. Mai & Beroza, 2002, Lavallée et al., 2006) is a reliable method in generating a large number of synthetic slip distributions with either a static or kinematic slip (Geist et al., 2014). In this method, the slip distribution is characterized as a power spectral density in the wavenumber domain, which captures realistic earthquake slip characteristics, stress drop distribution and a range of fault geometry (Geist & Oglesby, 2014, Mori et al., 2017a). Various algorithms with different parametrizations for generating stochastic source models have been developed in recent literature (e.g. Mai & Beroza, 2002, Lavallee et al., 2006, Goda et al., 2014, Davies et al., 2015, Griffin et al., 2017).

Mai and Beroza (2002) investigated the validity of source parameters using Gaussian, exponential, von Kármán, and fractal autocorrelation functions of available slip distributions and a proposed a random-field approach to model the slip distributions of the source models. The study found that the method can produce predictive slip distributions and that the fractal dimension and correlation lengths were related to the moment magnitude (Mw) as well as the fault’s width and length. Lavallee et al. (2006) derived stochastic models of various earthquakes. They indicated that a heavy-tail Levy distribution produces a closer match to slip inversions compared to Gaussian distributions that previous studies primarily used. However, the study only used four events with Mw between 6.0 and 7.2. Goda et al. (2014) compared tsunami wave profiles from a range of stochastic earthquake slip models for the 2011 Tohoku earthquake using the spectral analysis approach of Mai & Beroza (2002). The study was able to quantify the bias in the synthetic finite fault models by carrying out various transformations to ensure that the models had similar properties to those from previous events. The study highlighted the sensitivity of tsunami amplitudes and inundation to site location, variations in dip, and slip characteristics. A drawback was that the study used coarse bathymetry and elevation data, adding potential errors to the tsunami simulations. Goda et al. (2015) improved this by using higher-resolution bathymetry and elevation data and assessing the spatial inundation processes to produce more detailed tsunami hazard information. Goda et al. (2017a) further improved the method by considering the rupture process in both strong motion and tsunami simulations, thus facilitating the assessment and sensitivity analysis of the shaking and tsunami hazard parameters to uncertain features of slip concentrations. Davies (2019) studied the variability of tsunami observations of 18 events using three different approaches. The first approach assumed a uniform slip distribution and rupture area as a deterministic function of magnitude using the scaling relationships by Stasser et al. (2010). The second approach used a uniform-slip distribution and a variable area to account for the variability of the earthquake fault geometry by using scaling relation prediction errors. The third approach accounted for both rupture size variability and slip heterogeneity. The study showed that the first two approaches underestimated simulated tsunami amplitudes at all magnitudes, which was not apparent in the third approach, confirming that slip heterogeneity and fault geometry affect the tsunami amplitude in both near and far observations. They also found that the modifying the rupture area variability improves the second approach, producing results comparable to the third approach. These findings suggest that the inclusion of this variability in both approaches could potentially capture the epistemic uncertainty of the models.

2.3 Tsunami Simulations

Tsunami simulations and tsunami warning systems have become essential in research considering past major tsunami events (e.g. 2004 Indian Ocean, 2010 Maule, and 2011 Tohoku tsunamis). A challenge in tsunami early warning systems and tsunami preparedness is to account for multiple tsunami scenarios for a given area to understand the tsunami hazard better. Advances in tsunami hazard analysis have aimed to generate multiple scenarios to evaluate tsunami risk effectively and to produce reliable hazard and risk maps (Goda et al., 2017b). Moreover, particular interest has been put into tsunami simulations that can make effective real-time predictions of wave arrival times, amplitudes, and wave interactions with surrounding structures (Yolsal-Çevikbilen & Taymaz, 2012). In addition to the source models' uncertainties, the tsunami inundation characteristics can also add some uncertainty to the predictions because of the non-linear behaviour of tsunamis and their interaction with the variable surrounding (Mori et al., 2018). Hence, both tsunami source model parameters (i.e. slip distributions, fault geometry, surface and area, location, and seismic moment) and the coastal morphology are critical in the simulations, and an evaluation of such parameters is necessary. Furthermore, tsunami models for warning systems require generation and propagation data of past events to accurately predict future events and the risks to facilities and human lives (Gisler, 2008).

Tsunami modelling consists of three steps. First, the tsunami generation is simulated, where the initial conditions are calculated to obtain the water displacement due to earthquake rupture. Second, the propagation of the tsunami waves at different locations is simulated by solving the shallow water equations. Finally, the third step is tsunami inundation, calculated by dry/wet conditions determined by water depth. After synthesizing the earthquake source models, the tsunami initial condition is simulated by calculating the elastic displacement of the ocean floor. First, source parameters are calculated to set initial conditions (Section 2.1). Then, the transfer of the ocean bottom deformation to the water column is evaluated. This deformation causes water displacement and the exchange of energy and momentum from rock to water (Geist, 2005). In tsunami generation, the water displacement is often assumed to be identical to the ocean bottom's vertical deformation. The assumption comes from the fact that tsunamis are considered long waves because their wavelength is much greater than the water depth due to the difference between the fault plane (several tens to hundreds of kilometres) and the ocean depth in the source region (several kilometres). Thus, the horizontal movement of the ocean bottom due to faulting is assumed to be negligible in tsunami generation. Therefore, for long waves, the vertical acceleration of the water particles can be neglected compared to the gravitational acceleration, and the horizontal motion of the water mass from the ocean bottom to the surface (displacement) is assumed to be uniform.

An elastic theory of dislocation is used to calculate the surface displacement (u_i) on an elastic half-space due to a dislocation Δu_j across a surface Σ (i.e., crustal deformation due to faulting). Steketee (1958) obtained the following equation for the surface displacement:

$$u_i = \frac{1}{F}\iint_{\Sigma} \Delta u_j \left[\lambda\delta_{jk}\frac{\partial u_i^n}{\partial \xi_n} + \mu\left(\frac{\partial u_i^j}{\partial \xi_k} + \frac{\partial u_i^k}{\partial \xi_j}\right)\right] v_k \mathrm{d}\Sigma \qquad (2.1)$$

where δ_{jk} is the Kronecker delta, λ and μ are Lame's constants, v_k is the direction cosine of the normal to the fault surface element dΣ, and u_k^i denotes the *k*th component of the surface displacement due to the *i*th component of point force whose magnitude is F.

The Okada (1985) formulae are the preferred method to calculate the displacements u_i in three directions i.e. horizontal displacements U_1, U_2 and vertical displacement U_3 (Figure 2.1). They can be used to evaluate the displacement at an arbitrary point on the surface or inside the semi-infinite elastic medium due to a finite-fault source analytically. In this method, the earthquake is regarded as the rupture of a single fault plane with a set of physical parameters (dip, strike, rake, width, length, and depth).

The parameters that determine this displacement are the strike angle (represented by the x axis in Figure 2.1), the dip angle (δ), rake angle (θ), the angle γ between the Burger's vector ($D = U_1, U_2, U_3$), and the fault plane (W, L). In Figure 2.1, each vector (U_1, U_2, U_3) represents the movement of the hanging-wall side relative to the foot-wall side (D) and is related to D as: $U_1 = |D| cos\gamma \cdot cos\theta, U_2 = |D| cos\gamma \cdot sin\theta, and\ U_3 = |D| sin\gamma.$

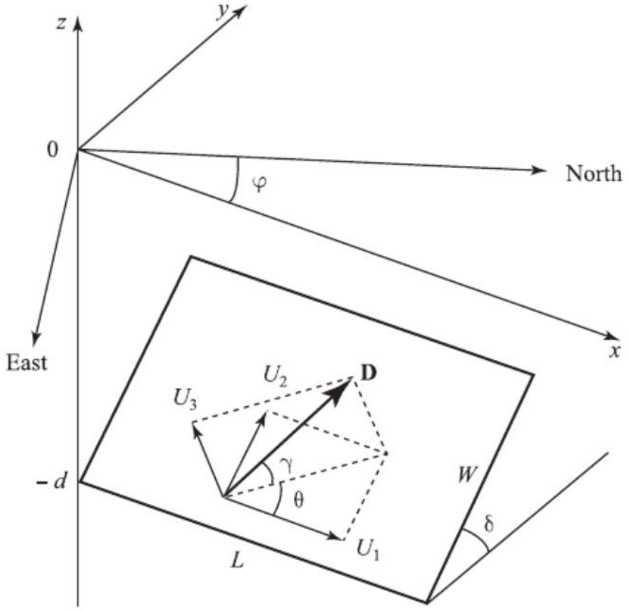

Figure 2.1 Geometry of the source model. From Physics of Tsunamis (p. 46) by Levin, B. & Nosov, M., 2009, Springer. Copyright 2009 by Springer Science + Business Media B.V

For a finite rectangular fault, the results condensed into a compact form are listed using Chinnery's notation || to represent the substitution:

$$f(\xi,\eta)|| = f(x,p) - f(x,p-W) - f(x-L,p) + f(x-L,p-W) \tag{2.2}$$

For strike-slip,

$$\begin{cases} u_x = -\frac{U_1}{2\pi}\left[\frac{\xi q}{R(R+\eta)} + \tan^{-1}\left(\frac{\xi\eta}{qR}\right) + l_1 \sin\delta\right]\Big\| \\ u_y = -\frac{U_1}{2\pi}\left[\frac{\tilde{y}q}{R(R+\eta)} + \left(\frac{q\cos\delta}{R+\eta}\right) + l_2 \sin\delta\right]\Big\| \\ u_z = -\frac{U_1}{2\pi}\left[\frac{\tilde{d}q}{R(R+\eta)} + \left(\frac{q\sin\delta}{R+\eta}\right) + l_4 \sin\delta\right]\Big\| \end{cases} \tag{2.3}$$

For dip-slip,

$$\begin{cases} u_x = -\frac{U_2}{2\pi}\left[\frac{q}{R} - l_3 \sin\delta\cos\delta\right]\Big\| \\ u_y = -\frac{U_2}{2\pi}\left[\frac{\tilde{y}q}{R(R+\xi)} + \cos\delta\tan^{-1}\left(\frac{\xi\eta}{qR}\right) - l_1 \sin\delta\cos\delta\right]\Big\| \\ u_z = -\frac{U_2}{2\pi}\left[\frac{\tilde{d}q}{R(+R+\xi)} + \sin\delta\tan^{-1}\left(\frac{\xi\eta}{qR}\right) - l_5 \sin\delta\cos\delta\right]\Big\| \end{cases} \tag{2.4}$$

For tensile fault,

$$\begin{cases} u_x = \frac{U_3}{2\pi}\left[\frac{q^2}{R(R+\eta)} - l_3\sin^2\delta\right]\| \\ u_y = \frac{U_3}{2\pi}\left[\frac{-\tilde{d}q}{R(R+\xi)} - \sin\delta\left\{\frac{\xi q}{R(R+\eta)} - \tan^{-1}\left(\frac{\xi\eta}{qR}\right)\right\} - l_1\sin^2\delta\right]\| \\ u_z = \frac{U_3}{2\pi}\left[\frac{\tilde{y}q}{R(R+\xi)} + \cos\delta\left\{\frac{\xi q}{R(R+\eta)} - \tan^{-1}\left(\frac{\xi\eta}{qR}\right)\right\} - l_5\sin^2\delta\right]\| \end{cases} \tag{2.5}$$

where

$$\begin{cases} l_1 = \frac{\mu}{\lambda+\mu}\left[\frac{-1}{\cos\delta}\frac{\xi}{R+\tilde{d}}\right] - \frac{\sin\delta}{\cos\delta}l_5 \\ l_2 = \frac{\mu}{\lambda+\mu}\left[-\ln(R+\eta)\right] - l_3 \\ l_3 = \frac{\mu}{\lambda+\mu}\left[\frac{1}{\cos\delta}\frac{\tilde{y}}{R+\tilde{d}} - \ln(R+\eta)\right] + \frac{\sin\delta}{\cos\delta}l_4 \\ l_4 = \frac{\mu}{\lambda+\mu}\frac{1}{\cos\delta}\left[\ln\left(R+\tilde{d}\right) - \sin\delta\ln(R+\eta)\right] \\ l_5 = \frac{\mu}{\lambda+\mu}\frac{2}{\cos\delta}\tan^{-1}\left(\frac{\eta(X+q\cos\delta)+X(R+X)\sin\delta}{\xi(R+X)\cos\delta}\right) \end{cases} \tag{2.6}$$

If cos (δ) = 0,

$$\begin{cases} l_1 = -\frac{\mu}{2(\lambda+\mu)}\frac{\xi q}{\left(R+\tilde{d}\right)^2} \\ l_3 = \frac{\mu}{2(\lambda+\mu)}\left[\frac{\eta}{R+\tilde{d}} + \frac{\tilde{y}q}{\left(R+\tilde{d}\right)^2} - \ln(R+\eta)\right] \\ l_4 = -\frac{\mu}{\lambda+\mu}\frac{q}{R+\tilde{d}} \\ l_5 = -\frac{\mu}{\lambda+\mu}\frac{\xi\sin\delta}{R+\tilde{d}} \end{cases} \tag{2.7}$$

$$\begin{cases} p = y\cos\delta + d\sin\delta \\ q = y\sin\delta - d\cos\delta \\ \tilde{y} = \eta\cos\delta + q\sin\delta \\ \tilde{d} = \eta\sin\delta - q\cos\delta \\ R^2 = \xi^2 + \eta^2 + q^2 = \xi^2 + \tilde{y}^2 + \tilde{d}^2 \\ X^2 = \xi^2 + q^2 \end{cases} \tag{2.8}$$

Okada (1985) solutions are used for horizontal bottom deformation. In slope gradients of less than 1/3, the tsunami generation is dominated by the vertical motion of water, and the horizontal motion of water is negligible (Iwasaki, 1982). However, if an earthquake happens on a steep slope (continental or coastal slopes) and the horizontal displacements due to faulting are relatively large and cause the slope to shift, the effects become significant and must be accounted for (Tanioka & Satake, 1996). Hence, the vertical displacement of water due to the horizontal movement of the slope (u_h) is calculated as:

$$u_h = u_x \frac{\partial H}{\partial x} + u_y \frac{\partial H}{\partial y} \tag{2.9}$$

The resulting displacement is then applied to generate the initial tsunami wave instantaneously or over a specified rupture time. Static tsunami generation assumes the earthquake (vertical deformation of the ocean bottom) to occur instantaneously, assuming that the phase speed of the tsunami is slower than the propagation velocity of the earthquake rupture. Some simulations use dynamic rupture models for an evolutionary tsunami generation process, using frictional parameterizations and fault stress distributions (Geist et al., 2014). Dynamic tsunami generation is usually done for ruptures of great length (i.e. 2004 Sumatra earthquake).

After the tsunami generation, the second step in tsunami simulation is the tsunami propagation across the ocean. Tsunami waves are formed after the release of a large amount of energy, in this case, an earthquake. The released energy is transferred to the water column in the form of waves that have wavelengths on the order of hundreds of kilometres (fault size = wavelength) and small amplitudes on the order of 1 m in deeper portions (water depth = amplitudes). Thus, tsunami waves typically have a ratio of water depth to wavelength of at least 1:20 ($\lambda \gg H$ where λ is the wavelength and H is the depth; Levin & Nosov, 2009). As the tsunami waves move along the ocean, they lose very little energy at greater depths, because of the great difference between wavelength and water depth, allowing them to preserve most of their energy while travelling. Thus, tsunamis can travel great distances. However, as the tsunami approaches shallow depths, it starts to slow down since the wave speed depends mainly on the depth of the water ($c = \sqrt{gH}$ where g is gravitational acceleration). As the tsunami front velocity decreases, the wavelength becomes shorter because the tail of the tsunami catches up with the slower front and increases the waves' amplitudes. The energy is then transferred into potential energy following the conservation of energy, and as the wave continues to slow down, it eventually breaks. A part of the tsunami is reflected back to the ocean, while the remaining part inundates the land.

The propagation of the waves is carried out in two surface dimensions over varying depth and distances. Tsunami waves are long waves; therefore, the shallow-water theory is valid when the wavelength is larger than the water depth. In tsunami simulations, the vertical accelerations are negligible compared to the gravitational acceleration and curvature trajectories. Thus, the vertical motion does not affect the pressure distribution, and the pressure is assumed to be hydrostatic and, therefore, a linear function of depth. The following equations further explain this:

$$\frac{\partial u}{\partial t} + u\frac{\partial u}{\partial x} + v\frac{\partial u}{\partial y} + g\frac{\partial \eta}{\partial x} + \frac{\tau_x}{\rho} = 0 \tag{2.10}$$

$$\frac{\partial \eta}{\partial t} + \frac{\partial[u(h+\eta)]}{\partial x} + \frac{\partial[v(h+\eta)]}{\partial y} = 0 \tag{2.11}$$

$$\frac{\partial v}{\partial t} + u\frac{\partial v}{\partial x} + v\frac{\partial v}{\partial y} + g\frac{\partial \eta}{\partial y} + \frac{\tau_y}{\rho} = 0 \tag{2.12}$$

where x and y are the two horizontal directions, respectively, g is the scalar vertical acceleration due to gravity, h is the height relative to the mean ocean depth, t is time, η is the vertical displacement, u and v are the water particle velocities in the x and y directions, respectively, ${}^{\tau_x}/_{\rho}$ and ${}^{\tau_y}/_{\rho}$ are the bottom frictions in both x and y directions. The bottom friction is expressed as an analogy to the uniform flow as:

$$\frac{\tau_x}{\rho} = \frac{1}{2g}\frac{f}{D}u\sqrt{u^2+v^2} \quad , \quad \frac{\tau_y}{\rho} = \frac{1}{2g}\frac{f}{D}v\sqrt{u^2+v^2} \tag{2.13}$$

where $D = h + \eta$ is the total water depth, f is the friction coefficient which can be described by using n is Manning's roughness coefficient. n depends on roughness of the bottom surface and is expressed as:

$$n = \sqrt{\frac{fD^{1/3}}{2G}} \tag{2.14}$$

Finally, the bottom friction is expressed as:

$$\frac{\tau_x}{\rho} = \frac{gn^2}{D^{4/3}} u\sqrt{u^2+v^2} \ , \ \frac{\tau_y}{\rho} = \frac{gn^2}{D^{4/3}} v\sqrt{u^2+v^2} \tag{2.15}$$

Typically, the Manning's coefficient is simplified and assumed to be 0.025 s/m$^{1/3}$. Furthermore, the coast is assumed to be free of dense vegetation which in some cases might not be applicable.

Equations (2.10) to (2.12) are not commonly used since when discretized, the equations might not satisfy the conservation of mass. Goto et al. (1997) recommended the following equations instead since they have no effect on the conservation of mass and satisfy the conservation of momentum as well.

$$\frac{\partial \eta}{\partial t} + \frac{\partial M}{\partial x} + \frac{\partial N}{\partial y} = 0 \tag{2.16}$$

$$\frac{\partial M}{\partial t} + \frac{\partial}{\partial x}\left(\frac{M^2}{D}\right) + \frac{\partial}{\partial y}\left(\frac{MN}{D}\right) + gD\frac{\partial \eta}{\partial x} + \frac{gn^2}{D^{7/3}} M\sqrt{M^2+N^2 = 0} \tag{2.17}$$

$$\frac{\partial N}{\partial t} + \frac{\partial}{\partial x}\left(\frac{MN}{D}\right) + \frac{\partial}{\partial y}\left(\frac{N^2}{D}\right) + gD\frac{\partial \eta}{\partial y} + \frac{gn^2}{D^{7/3}} N\sqrt{M^2+N^2 = 0} \tag{2.18}$$

where M and N are the discharge fluxes in the x and y directions, respectively, and are expressed as:

$$M = u(h+\eta) = uD \quad , \ N = v(h+\eta) = vD \tag{2.19}$$

The non-linear shallow-water equations allow the effective propagation analysis of the tsunami waves that increase the resolution in the wave height as the tsunami approaches the shore. In the deeper parts of the ocean, the linear long-wave theory gives good results since bottom friction does not influence tsunami propagation. However, as the depth decreases, the equations should switch to a shallow-water theory with bottom friction. Shallow-water equations are suitable for simulating maximum run-up and inundation; however, they are not sufficient to estimate wave forces (Shuto, 1991). In addition, as the distance of propagation increases, Earth's curvature and Coriolis effect should be incorporated into the tsunami propagation model.

As the tsunami approaches the coast tsunami amplitudes increase, which determines the danger of the tsunami to coastal communities. The increase in amplitude is due to the compression of the wave train in space as the wave propagation velocity decreases due to a decrease of depth (Levin & Nosov, 2009). This increase of height leads to the third step, which is the tsunami shoaling, inundation, and run-up over the coastlines. Tsunami interaction with the coastal zone has been one of the most challenging problems relevant to tsunami dynamics. There are three types of run-up along the coast: First is spilling, characterized by the breaking of the wave's crest, and flowing down the frontal slope and is particular to gently sloping bottoms. The second type is plunging which happens when the wave's crest surpasses foot and curls down; this type is particular to inclined bottom slopes. Finally, the third type is surging, which is the most common type, the wave floods the coast without breaking, particular to steep slopes.

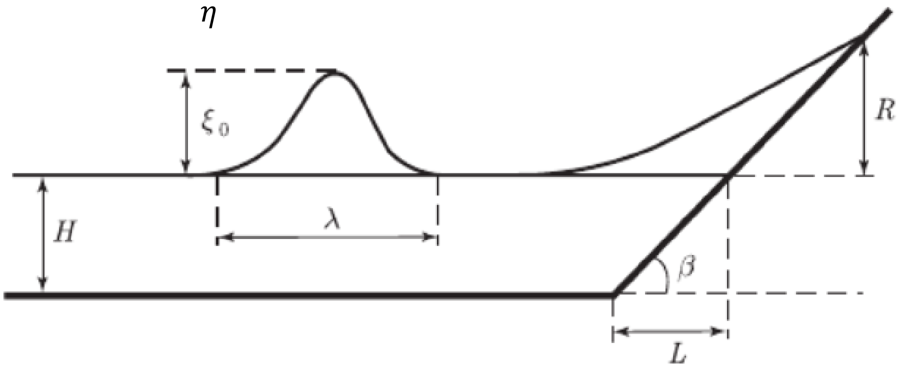

Figure 2.2 Formulation of the problem of a tsunami run-up on the coast (Levin & Nosov, 2009)

Most models describe the wave dynamics in the coastal zone by using the non-linear shallow-water equations (Equations 2.17-2.19). Since, as the tsunami wave approaches the coast, the amplitudes may be proportional to the depth (Levin & Nosov, 2009). Therefore, run-up is considered only in non-linear computations (Goto et al., 1997). The shallow water equations can then lead to the wave speed equation: $\sqrt{gD}$ from which a variety of conclusions can be drawn based on geometrical optics since wave refraction happens as the tsunami travels around different morphology (Geisler, 2008). This interaction of the tsunami with the surrounding topography highlights the importance of detailed knowledge of bathymetry and elevation in the zone of interest.

Moreover, the shallow water equations can help determine boundary conditions for the tsunami inundation simulations. Generally, during run-up simulations, the initial water level is equal to the ground height, and a widespread boundary condition, the ‘vertical wall approximation,’ for tsunami run-up is used. This approximation imitates the continental slope (Figure 2.2). Therefore, the tsunami run-up is modelled considering a slope connected with a smooth horizontal ocean bottom. However, this is a considered a idealistic situation and it is not necessarily guaranteed when realistic tsunami simulations using bathymetry data are considered. Furthermore, the run-up can be modelled by a moving boundary approach where the computational cell’s dry/wet is determined based on the total water depth relative to the elevation following the expression: $D = h + \eta > 0,$ then the cell is submerged, whereas $D = h + \eta \ \leq 0$ the cell is dry. When coastal structures are modelled, the discharge overflowing the structure should be incorporated explicitly in the simulations.

There are some difficulties in run-up simulations to have realistic results. The first difficulty is the quality of the bathymetry and topographical data. The necessity of having detailed datasets comes from the fact that there is a significant reduction of the tsunami wave’s wavelength in shallow-water zones and the influence of topographic features in the interaction of the waves with the coast. The second difficulty is the availability and quality of run-up measurements of past events in the area of interest, in addition to water flow parameters information. The third is the inclusion of coastal structures in tsunami simulations. Finally, the fourth difficulty is the erosion that tsunamis waves can cause since that can change the aspect of the coast (i.e., demolition of buildings and destruction of vegetation) and how the waves will interact with the coast.

Chapter 3

3 Stochastic Source Modelling and Tsunami Analysis of the 2012 Mw 7.8 Haida Gwaii Earthquake

On October 28th, 2012, off the western coast of Moresby Island (Figure 3.1) an Mw 7.8 earthquake occurred on a thrust fault beneath the Queen Charlotte Terrace (QCT) beneath the Queen Charlotte Fault (QCF). The earthquake was the second largest instrumentally recorded in the region after the 1949 Mw 8.1 earthquake. The 2012 earthquake triggered a tsunami that was recorded all along the Pacific Ocean. On the northwestern Pacific, the tsunami was recorded on tide gauges, bottom pressure recorders and deep-ocean buoys. Furthermore, coseismic deformation measurements were obtained during the consequent months by GPS stations (Nykolaishen et al., 2015) and intertidal biological organisms level measurements (Haussler et al., 2015). The tsunami run-up was measured by field surveys (Leonard & Bednarski, 2014). Multiple past studies have constrained the source fault using different methods. In the present chapter, a tsunami analysis of the Haida Gwaii region using stochastic source modelling and Monte Carlo tsunami simulation is conducted to develop stochastic source models that generate tsunami waves in close match with the recorded observations. The methodology involves the synthesis of stochastic sources constrained by deformation measurements, aftershock sequences, and thermal measurements. The synthesized source models are then used in Monte Carlo tsunami simulations with run-up to simulate the tsunami waves at different offshore and offshore locations.

The chapter is organized as follows: First, an overview of the 2012 Haida Gwaii event; and the region's seismicity and tectonics. Secondly, the finite fault models from the literature are presented. Thirdly, the methodology for evaluating the existing source models, the stochastic source modelling, and Monte Carlo tsunami simulation for the present study is explained in detail. Finally, the results of the tsunami analysis of the 2012 earthquake are explained in detail for offshore and onshore observations.

3.1 2012 Haida Gwaii Event

At 8:04 P.M Pacific daylight time on October 28, 2012, an Mw 7.8 earthquake hit the region of Haida Gwaii, British Columbia, Canada (Figure 1.1). The perceived shaking in the Haida Gwaii Islands lasted between 1.5 to 2 minutes, with strong shaking for about 30 seconds (Bird & Lamontagne, 2015). The earthquake was felt throughout British Columbia, and some accounts indicated that it reached as far as Yukon, Alberta and Montana (Bird & Lamontagne, 2015). Due to the far distance between the epicentre and the populated areas, this earthquake resulted in minimal residential house damages in the region (Bird & Lamontagne, 2015). In addition, the epicentre was close to other thrust events of the zone, such as the 2001 Mw 6.2 earthquake south of the QCF (Lay et al., 2013).

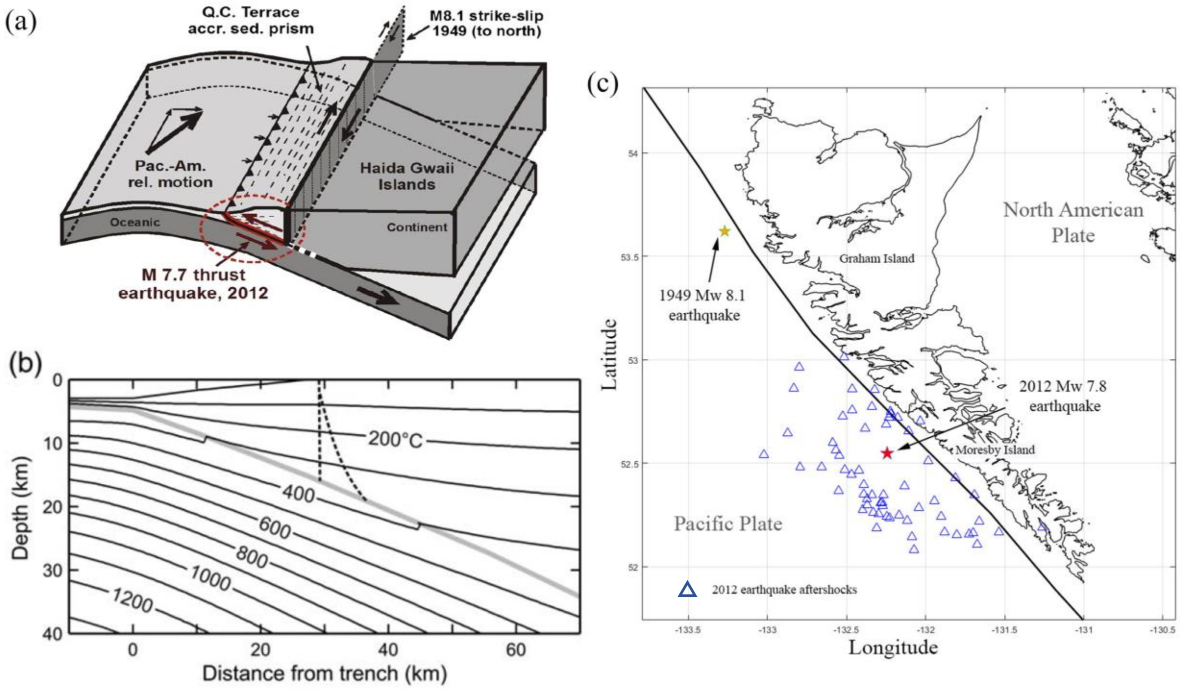

Figure 3.1 a) location of the thrust fault beneath the QCT in which the 2012 earthquake occurred, the relative plate motions in this area, and location of the near-vertical QFC (Cassidy et al., 2014). (b) Surface temperatures, two possible geometries of

The 2012 earthquake nucleated below the western coast of Moresby Island. However, most of the slip occurred 20 km off the coast of Haida Gwaii at a depth of 23 km, below the sedimentary wedge, and about 230 km north of the triple junction between the Explorer, Pacific, and North American Plates (Lay et al., 2013, Bird & Lamontagne, 2015, Haeussler et al., 2015; see Figure 3.1a). The United States Geologic Survey (USGS) reported a fault area of about 140 km by 30 km. In comparison, Kao et al. (2015) reported fault area dimensions of ~120 km by 30 km based on the epicentre location and the aftershock's spatial distributions. The mainshock's epicentre was located at 52.622°N, 132.103°W, at a depth of 14 km (Kao et al., 2015). Ground motions with the highest amplitudes were observed on the western coast of Moresby Island, in Masset and Prince Rupert (Figure 1.1), and reached the maximum horizontal accelerations of 0.2 g in the region (Leonard & Bednarski, 2014, Bird & Lamontagne, 2015, Barth et al., 2020). After the mainshock, thousands of aftershocks followed, the largest being an Mw 6.3 event on October 28, 2012, and an Mw 6.1 event in October 2019 (Cassidy et al., 2014, Barth et al., 2020; see Figure 3.1c).

Global Positioning System (GPS) data indicated southwestward coseismic surface displacement of 3 to 115 cm on the western coast of Moresby Island. In addition, seismic waveforms, aftershocks, and coseismal deformation from GPS measurements indicated that the earthquake had a low angle thrusting motion, with a slip partitioning in the transgressive boundary (James et al., 2013, Lay et al., 2013, Kao et al., 2015, Nykolaishen et al., 2015). This was consistent with the coseismic offset expected from an offshore shallow-thrust earthquake (Cassidy et al., 2014, Nykolaishen et al., 2015). Moreover, the shallow angle of the 2012 Mw. 7.8 Haida Gwaii earthquake confirmed oblique convergence and underthrusting (James et al. 2013, Cassidy et al. 2014). Lay et al. (2013) performed a series of teleseismic P-wave seismic inversions and estimated the earthquake rupture parameters, such as fault dimensions, rupture velocity, and dip and hypocentre, by fitting their simulations with the observations at DART buoys. The P-wave projection imaging indicated a non-uniform rupture expansion toward the southeast and northwest. Leonard et al. (2014) calculated a recurrence rate of ~ 760 years for Mw 7.7 strike-slip earthquakes based on the convergence rate and the average earthquake slip.

The tsunami triggered by the earthquake was recorded on tide gauges, Bottom Pressure Recorders (BPRs) by Ocean Canada's Neptune network and Deep-ocean Assessment and Reporting of Tsunamis (DART) buoys across the Pacific Ocean (Figure 3.2). Horizontal and vertical deformations were also obtained using GPS measurements (Nykolaishen et al., 2015) and intertidal biological indicators (Haeussler et al., 2015). Moreover, the run-up level was defined by natural and artificial ocean debris and reached more than 7 m at locations like Mike Inlet in Moresby Island (James et al., 2013, Lay et al., 2013, Leonard & Bednarski, 2014; see Figure 3.8). Leonard et al. (2014) predicted that events of the magnitude of the 2012 earthquake could yield run-ups of 3–7 m for coastlines within 40 km of the rupture zone.

3.2 Tectonics and Seismicity of the Haida Gwaii Region

The QCF is a primarily right-lateral transform fault boundary of the Pacific and North American Plates. It extends more than 800 km from the triple junction north of Vancouver Island to the Alaskan Subduction Zone (Cassidy et al., 2014, Hyndman, 2015). Towards southern Alaska, the QCF becomes the Fairweather Fault (Walton et al., 2013). To the north, the QCF strikes at 338º and is mainly a transform fault plate boundary with ocean crust seaward and continental crust landward (Cassidy et al., 2014). Most earthquakes in the northern region, have occurred in the vertical QCF parallel to the Pacific-North American Plate’s motion, with a nearly pure strike-slip rupture as mechanism (Hyndman, 2015). The south of the QCF is marked by the triple junction of the Pacific-North American-Explorer plate and a slow margin convergence known as the Winona basin (Hyndman, 2015, Kao et al., 2015).

3.2.1 Margin Convergence and Underthrusting

Before the 2012 earthquake, there had been evidence of subduction in the region, later confirmed by the 2012 earthquake. The evidence included: gravity and heat flow data, the existence of a bathymetric trench and accretionary prism, and receiver-function analyses showing dipping oceanic slab (Leonard & Bednarski, 2014).

Hyndman (2015) further explains the oblique convergence accommodated by underthrusting by the following factors:

1. An offshore ocean plate fore bulge, which is characteristic of subduction underthrusting.
2. A trough with characteristics of a subduction trench.

3. The QCT appears to be a compressive sedimentary fold and thrust belt.
4. The gravity pattern across the margin has a linear low over the Queen Charlotte trough and terrace and large highs over the western coast of the islands.
5. The heat flow pattern across the margin and the offshore high head decreases landward under the terrace.
6. Landward-dipping boundaries are interpreted to delineate the underthrust.
7. GPS-derived displacement vectors on the islands are oriented 10° to 30°clockwise from the margin trend.
8. The uplift in the western coast of the islands and the high and steep topography along the western coast of Haida Gwaii are the result of the oblique convergence (Motazedian et al., 2016).

In addition to the factors stated above, the plate motion kinematics in the QCF match the down-dip transition of the seismogenic behaviour of the megathrust, which is thermally controlled. The landward part of the QCF accommodates the oblique motion of the oceanic plate beneath the continental crust and exhibits creep (Wang et al., 2015; see Figure 3.1b). While the seaward shallow thrust accommodates the normal component relative to the plate motion, noting that this portion produced the 2012 Haida Gwaii earthquake, and the QCF accommodates the strike-slip component. Lastly, the recurrence period for this type of earthquake might be 760 years, assuming thrusting and no creeping in the plate convergence (Leonard et al., 2014).

3.2.2 Fault Geometry

The complexity of the evolving triple junction with the Explorer Plate and the changes in relative motion between the Pacific and North America Plates make it difficult to constrain the regional plate boundaries (Lay et al., 2013). Rohr (2015) identified that the northern part of the Revere-Dellwood Fault zone overlaps the southern end of the QCF and is close to the southmost extent of the 2012 thrust earthquake, which might be the southern limit of the main underthrusting. Furthermore, coseismic subsidence on the western coast of Haida Gwaii suggested that the main rupture did not extend landward from the QCF (Nykolaishen et al., 2015). Based on coseismic subsidence and arrival times at local seismograph stations, Kao et al. (2015) suggested a relocated position for the epicentre 5 km further seaward, which implies that the Haida Gwaii mainshock was near the bottom of the seismogenic interface. The aftershock distribution also indicated that the earthquake ruptured mainly offshore with a limited extension landward just under the coast (Hyndman, 2015). Moreover, the lack of aftershocks down-dip landward and thrust-aftershocks might also indicate that the total stress was located on the shallow part of the thrust plane (Lay et al., 2013; see Figure 3.1).

GPS data recorded 30 cm subsidence on the southern part of Moresby Island, further implied that the rupture was entirely offshore (Nykolaishen et al., 2015). The aftershock distributions defined a rupture zone area of ~150 km in length and a width of 30 km (about the width of the QCT). The width of the fault is constrained by thermal models, which suggest a landward limit of the rupture (Cassidy et al., 2014, Kao et al., 2015, Wang et al., 2015). Furthermore, thermal constraints of the potential seismogenic zone as well as the kinematics of the slip partitioning, which is predominantly orthogonal to the margin, assume that the Haida Gwaii rupture was limited mainly updip of the intersection of the thrust fault with the QCF (Cassidy et al., 2014, Nykolaishen et al., 2015, Wang et al., 2015). In addition, there have not been thrust events associated with the plate interface in the landward part of the QCF (Wang et al., 2015). The Global Centroid Moment Tensor Project reports this event as a shallow thrust mechanism with strike = 318°, dip = 25°, and rake = 104° (Nykolaishen et al., 2015).

3.3 Observations

The 2012 Haida Gwaii earthquake generated a tsunami that was recorded on Fisheries and Ocean Canada (FOC) tide gauges throughout the Haida Gwaii Islands, Vancouver Island, and the mainland. In addition, NEPTUNE, Ocean Network Canada (ONC) bottom pressure sensors (BPRs) recorded the event along southwestern Vancouver Island (Leonard and Bednarski, 2014, Fine et al., 2015). On the American side, the 2012 tsunami event was recorded at National Oceanic and Atmospheric Administration (NOAA) tide gauges; at least 110 instrumental records of this event are located on the NOAA tsunami database (Fine et al., 2015). Across the Pacific Ocean, Deep-ocean Assessment and Reporting of Tsunami (DART) stations recorded the event (Figure 3.2). Deformation was also measured along the main island in the months following the earthquake by GPS measurements

(Nykolaishen et al., 2015) and biological intertidal indicators (Haussler et al., 2015). In addition, Leonard and Bednarski (2014) conducted field surveys to measure the tsunami run-up along bays and inlets several weeks after the earthquake. Therefore, the 2012 Haida Gwaii event was well documented, providing important information for the validation of tsunami simulations, which can help constrain the source parameters for possible future events in the zone.

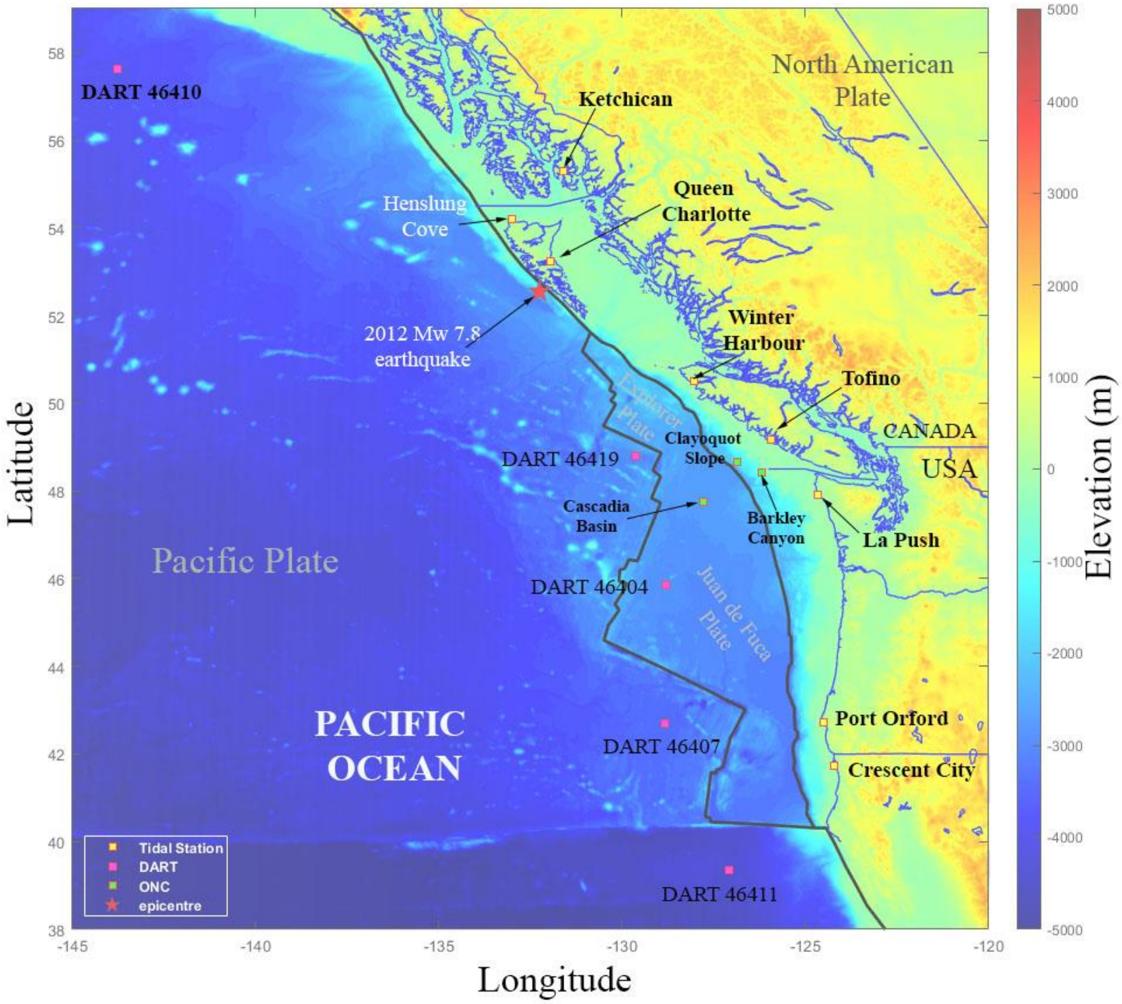

Figure 3.2 Map of Haida Gwaii showing the locations of FOC and NOAA tide gauges, Ocean Network Canada BPRs and DART buoys that recorded the 2012 Haida Gwaii tsunami

3.3.1 Deformation

The horizontal and vertical deformations of the 2012 Haida Gwaii earthquake were recorded using GPS measurements in the following months after the event (Table 1.1). Nykolaishen et al. (2015) investigated the coseismic and postseismic displacements at a series of GPS stations along Moresby Island, southern Haida Gwaii (Figure 3.3). However, there was only one continuously operating GPS station (BCSS) about 80 km from the epicentre in the region. Therefore, to complement this station and monitor the aftershock sequences, a set of GPS stations along temporary seismic stations was placed in the Haida Gwaii region two weeks after the earthquake by the Geological Survey of Canada (GSC) of Natural Resources Canada (NRCan; James et al.2013). The results show a coseismic displacement of 22 cm in the south-southwest part of the Haida Gwaii for the continuously GPS station (BCSS) with horizontal deformations ranging from 3 cm to 115 cm, whereas the vertical deformations showed subsidence of 1 cm to 30 cm (except for BCPR that presented uplift). The site (BARI) closest to the epicentre (30 km) recorded a coseismic displacement of 115 cm to the south-southwest and subsidence of 30 cm (Figure 3.3a). The cumulative postseismic horizontal displacements for seven GPS sites were up to 6 cm over one year (Nykolaishen et al., 2015). The results suggest that multiple processes might be involved, like long-term processes that might include elastic deformation that did not contribute to the coseismic displacement during the earthquake and started a few days after the earthquake indicating an aseismic after-slip of the deeper portion of the fault beneath Moresby Island.

Table 3.1 Coseismic offsets at GPS stations in the Haida Gwaii region

Site	Longitude°	Latitude°	dN (cm)	dE (cm)	dHGHT (cm)
BCPR	-130.435	54.277	-0.024	-0.013	0.007
YAKA	-131.837	54.071	-0.052	-0.026	-0.011
BCSS	-131.808	53.254	-0.19	-0.104	-0.007
NCRS	-131.960	53.144	-0.283	-0.15	-0.06
MORE	-132.087	53.020	-0.482	-0.262	-0.107
BARI	-131.753	52.5766	-0.931	-0.682	-0.303
STJA	-131.016	51.937	-0.068	0.019	-0.054

dH, north component offset; dE, east component offset, dHGHT, vertical component offset

The vertical coseismic deformations (Figure 3.3b) were also measured by the upper growth limits of two intertidal organisms (rockweed and barnacle) at 25 different sites on the western coast of Moresby Island (Haussler et al., 2015). The mean elevations of the organism with respect to the mean sea level were evaluated by a linear fit to find the vertical deformation. Lower elevations between the organism and the mean sea level were correlated to subsidence after the earthquake. The results show coseismic subsidence of around 40 cm to 60 cm along the entire western coast. There are also differences in elevation between the upper limits of each organism in the northern and southern parts, with decreasing elevations from north to south. Lower elevations were measured in the rupture region. These lower values in the south of the island were consistent with the GPS measurements in the southern part of the Haida Gwaii region.

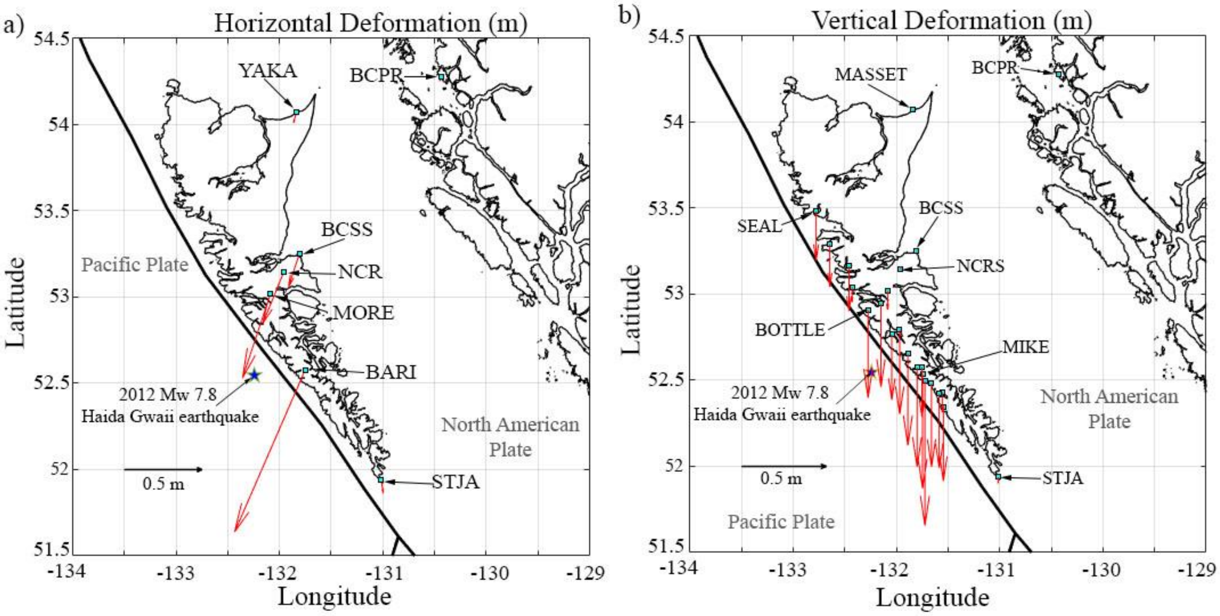

Figure 3.3 a) Horizontal deformation by GPS measurements. b) vertical deformation by intertidal biological indicators and GPS measurements

3.3.2 Tide Gauges

The tsunami waves were recorded on FOC and NOAA tide gauges scattered throughout the Pacific Ocean (Figure 3.2). Eleven FOC tidal stations recorded the tsunami waves around British Columbia (BC), with nine Permanent Water Level Network (PWLN) stations and two temporary stations. All FOC stations exposed on the BC western coast recorded tsunami amplitudes, including some onshore locations, such as Queen Charlotte. The tsunami signals at FOC stations had a sampling rate of 1 minute (Figure 3.4).

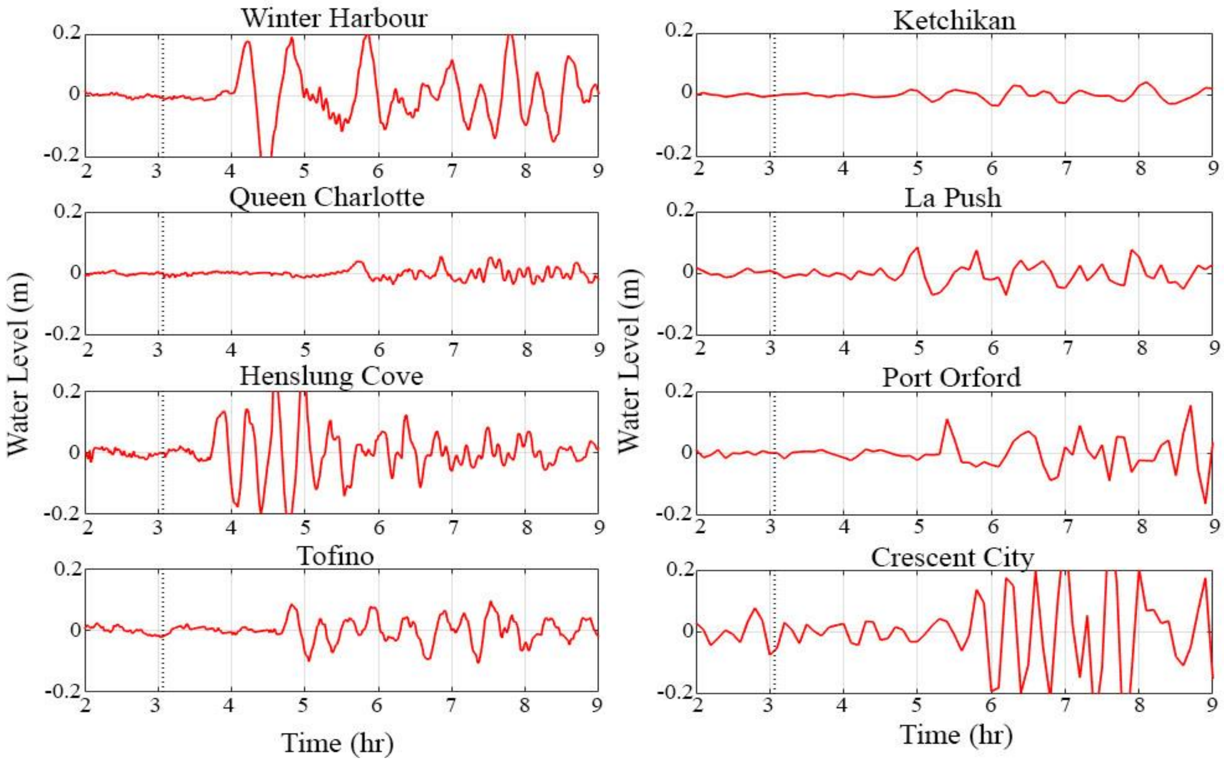

Figure 3.4 Time histories of the 2012 Haida Gwaii tsunami waves at FOC and NOAA tide gauges

NOAA stations recorded amplitudes at coastal locations in Alaska, California, Oregon, Washington, and Hawaii. High amplitudes were recorded away from the source at stations in Hawaii, and smaller amplitudes were recorded north of the rupture zone (i.e., Ketchikan; Figure 3.4). While the highest amplitudes were recorded on stations south of the rupture (i.e., Port Orford, Crescent City, Figure 3.4). The tsunami signals for NOAA stations had a sampling rate of 6 minutes.

In this study, only stations close to the rupture area are analyzed. The stations were further scrutinized by the data quality, wave periods, wave amplitudes, and distances to the source area (4 FOC and 4 NOAA stations). The tidal records were processed to extract the tsunami wave amplitudes from the time series. The tidal records were processed using a Butterworth high-pass filter to attenuate low-frequency signals associated with tidal atmospheric processes. Since the records had different sampling rates, the signals were resampled to a sampling rate of 1 second, respecting the Nyquist frequency. Despite the earthquake's magnitude, the amplitudes recorded at the chosen stations (Figure 3.2) were relatively small. Fine et al. (2015) noted that the low amplitudes are related to the directivity of the tsunami source region, which radiated the tsunami energy in an offshore direction, and the shadowing effect of Haida Gwaii. The maximum amplitudes were recorded on Henslung Cove (28 cm) and Winter Harbour (20 cm). Furthermore, it is also important to note that the region's topography is constituted mainly of fjords and cliffs, which can shield the stations from the tsunami waves. The travel path can also explain these low amplitudes since the tsunami waves had to travel around the southern and northern tips of Haida Gwaii to reach some of the stations. The time arrivals of the first tsunami wave at different stations ranged between 1 and 3 hours after the earthquake (Table 3.2).

Table 3.2 Wave parameters of the October 28, 2012 Haida Gwaii tsunami derived from tide gauge observations on the northwestern Pacific

Stations	First Wave	
	Arrival Time (UTC)	Maximum Amplitude (m)
Winter Harbour (FOC)	4:13	0.18
Queen Charlotte (FOC)	5:42	0.04
Henslung Cove (FOC)	3:52	0.13
Tofino (FOC)	4:49	0.09
Ketchikan (NOAA)	4:54	0.018
La Push (NOAA)	5:00	0.09
Port Orford (NOAA)	5:24	0.11
Crescent City (NOAA)	5:48	0.14

3.3.3 Deep-Ocean Observations

Deep-sea observations were recorded on both ONC BPRs and DART stations (Figure 3.5). ONC BPRs located to the west of Vancouver Island had the highest resolution and highest sampling rate at 1 second. While the DART stations had a standard sampling rate of 15 minutes, that switched into a 1-minute sampling mode at the time of the earthquake and then switched back to the standard 15-minute sampling rate. The tsunami signals for both ONC and DART records were filtered with a high-pass filter. Since the DART stations had different sampling rates, the signals were re-sampled to 1-second intervals to match the sampling rate of the other observation stations. Three out of the four ONC BPRs were picked based on data quality and the amount of background noise present. The three stations are located on the shelf, continental slope, and in deep water. Five DART stations were chosen for the present study based on data quality and distance from the source. The closest stations to the source zone were picked due to the limitations of the tsunami simulation code, and the present bathymetry of the northern regions, which presented clear distortion in the Alaska region.

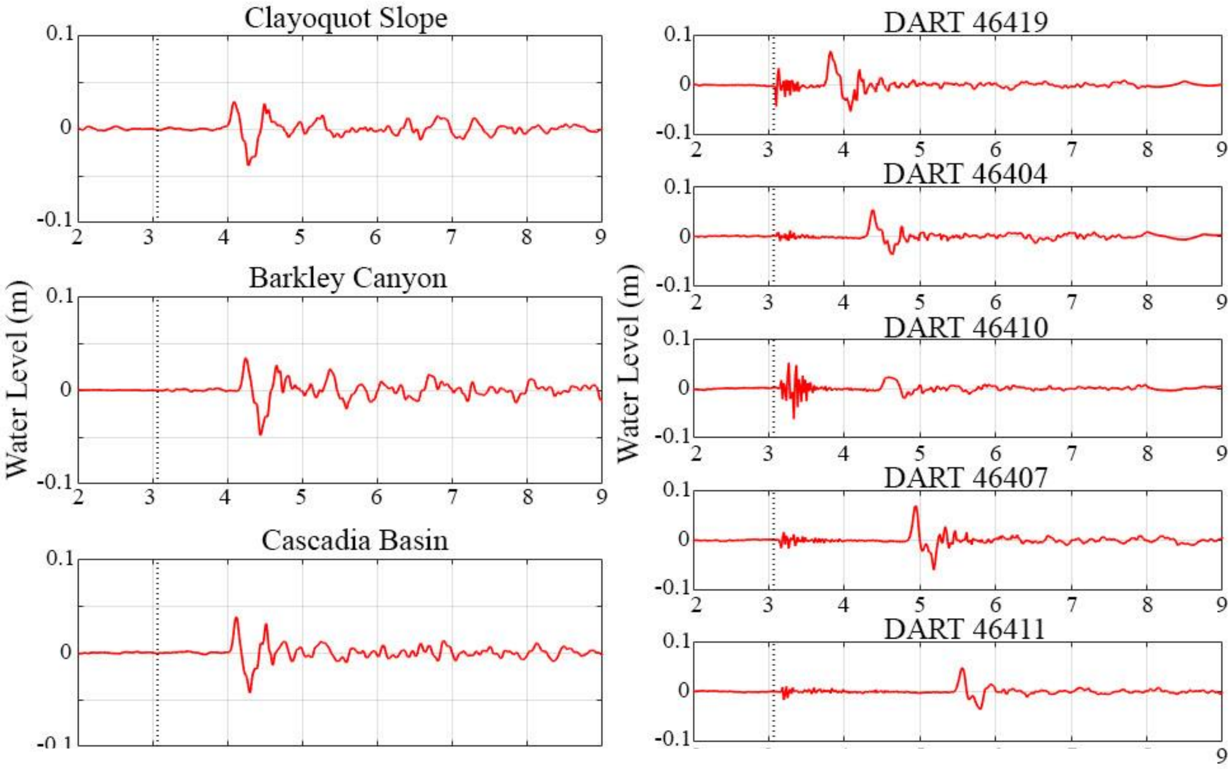

Figure 3.5 Time histories of the 2012 Haida Gwaii tsunami waves at ONC's BPRs and DART buoys

The recorded tsunami amplitudes were relatively small due to the stations not being located directly in the tsunami propagation path. The highest amplitudes were recorded at stations DART 46407 and DART 46419 (Figure 3.5, Table 3.3). Furthermore, both observations had relative low background noises since they are not affected by coastal effects in comparison to the coastal tide gauges (Fine et al., 2015); thus, deep-sea observations provide accurate tsunami waves information.

Table 3.3 Wave parameters of the October 28, 2012 Haida Gwaii tsunami derived from deep-sea observations on the northwestern Pacific

Stations	First Wave		
	Water Depth (m)	Arrival Time (UTC)	Maximum Amplitude (m)
Clayoquot Slope	1258	4:22	0.05
Barkley Canyon	392	4:57	0.07
Cascadia Basin	2660.5	4:34	0.02
DART 46404	3738	5:34	0.05
DART46407	3300	3:49	0.07
DART46410	3755	4:05	0.03
DART 46411	4325	4:14	0.03
DART 46419	2795	4:06	0.04

3.3.4 Run-up Observations

Leonard and Bednarski (2014) conducted the post-tsunami field surveys, obtaining the near-field observations. Unfortunately, the lack of eyewitness accounts, the limited accessibility of the terrain, and the fact that the Haida Gwaii region is prone to large storms made post-tsunami surveys difficult to carry out. Thus, the run-up data were limited to a small number of sheltered bays and heads of long inlets (Leonard & Bednarski, 2014, Fine et al., 2015). The run-up was measured based on disturbed forest floor, evident erosion, depositional evidence, and natural or manmade debris with a clear oceanward origin (Figure 3.6). The run-up sites were divided into two categories. The first was sites that were exposed to storm waves; these sites had the larger measured run-up. The second was sites sheltered from storms, where smaller values were observed (Table 3.4). The maximum run-up at sites open to storm waves was 13 m at Davison Inlet, whereas the maximum measured run-up in sheltered from storm waves sites was 7.6 m at Mike Inlet.

Table 3.4 Tsunami runup and inundation data of the 2012 Haida Gwaii tsunami

Sites	Run-up (m)	Inundation from shore(m)
	Sites Sheltered from Storm Waves	
Seal Inlet	3.6	28.5
Sunday Inlet	4.8	23.6
Pocket Inlet	5.3	29.1
Mike Inlet	6.4	22.8
Puffin Cove	3.4	5
Goski Bay	4.3	27.4
Staki Bay	3.1	25.5
Louscoone Inlet	3.7	12.8
	Sites Exposed Storm Waves	
Otard Bay	6.8	34.8
Gudal Bay	6.9	8.5
Saunders Island	7.3	29
Davidson Inlet	9	21.1
Kwoon Cove	6.5	5
Ta'dasl	8.1	14
Gilbert Bay	7.3	30.8

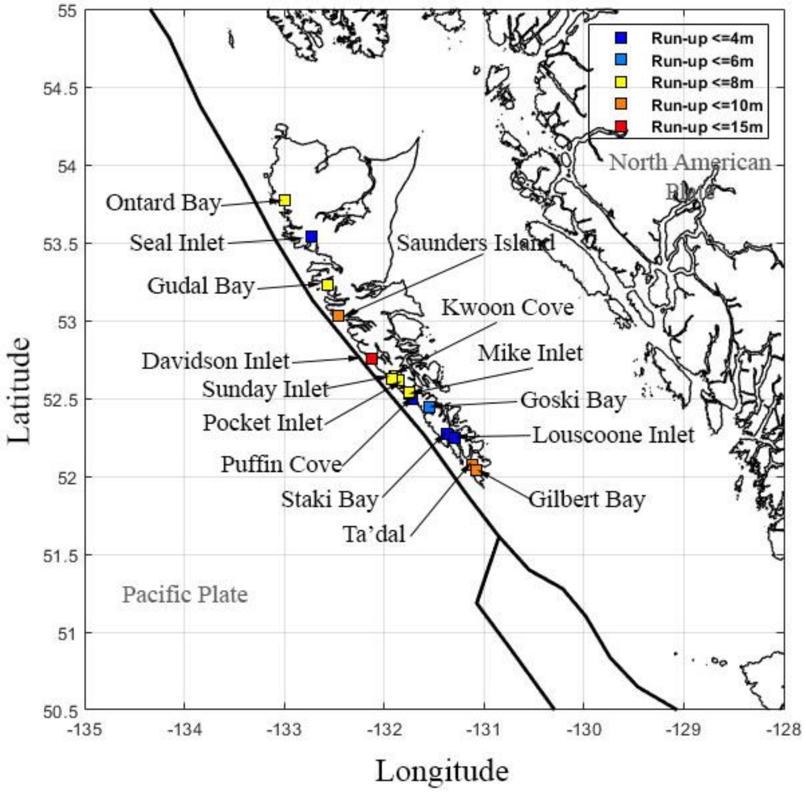

Figure 3.6 Run-up sites with colors depending on amount of run-up

These high tsunami run-ups might result from the natural resonant periods of the inlets that promote wave amplification. Another plausible explanation is that before the post-tsunami surveys, a large storm occurred in the region, possibly overprinting the tsunami evidence, especially in the sites that were exposed to storm waves.

3.4 Inversion Models

Inversion models are an important tool in tsunami simulation analysis, as they are based on past seismic events. These models attempt to produce close approximations of earthquake rupture processes by combining observed data (i.e. teleseismic data, strong motion, geodetic observations, and tsunami observations) and geophysical model predictions (Goda et al., 2016). However, it is important to note that finite fault models have limitations due to their resolution and robustness (Lay et al., 2013, Goda et al., 2016, Mori et al., 2018). Nevertheless, in the literature, earthquake databases with finite fault models are vastly available, such as SRCMOD finite-source rupture model database (Mai & Thingbaijam, 2014) and the United States Geological Survey National Earthquake Information Center (Hayes, 2017). There are various finite fault models for the 2012 Haida Gwaii earthquake (Table 3.5). Most of the literature models used in this study were obtained from the SRCMOD database. Six inversion models were gathered, analyzed, and used as constraints for the stochastic source models.

Table 3.5 Parameters of inversion models from literature

Model	Length (km)	Width (km)	Strike, Dip, Rake	Seismic moment (Nm)
Lay et al., (2013)	144	52	320,18.5,109	6.74×10^{20}
Wei, (2012)	210	90	319,29,112	7.00×10^{20}
Shao & Ji, (2012)	144	60	325,29,112	4.27×10^{20}
Hayes, (2013) (Fine et al. 2015)	252	82	323,30,120	7.33×10^{20}
Gusman et al., (2016)	165	60	317,18.5,103	5.30×10^{20}
Hayes, (2017)	252	82	323,30,125	7.33×10^{20}

Lay et al. (2013) used teleseismic broadband P waves and SH waves to generate a finite fault model of the 2012 event (Figure 3.7a). The model was constrained using W-phase solutions, information from short-period back projections, and tsunami observations off the coast of Hawaii and DART buoys. The fault geometry, rupture velocity, and hypocentre were matched to the near and far-field characteristics using DART buoys observations. Overall, the final model matched broadband teleseismic P waves, short-period projections, and tsunami observations near Hawaii. However, the model had some uncertainty in the location of the hypocentre. Wei (2012) used teleseismic P waveforms and 63 SH waveforms for the inversion model (Figure 3.7b). The data were then used to obtain the slip distribution of the fault plane using the inversion algorithm by Ji et al. (2002), which introduces a wavelet transform to constraint the time and frequency characteristics of the seismic waveforms. Shao and Ji (2012) used teleseismic broadband P waveforms, SH waveforms, and long-period surface waves for the inversion of the finite fault model (Figure 3.7c). The data were converted to displacement, and the finite-fault inverse algorithm (Ji et al., 2002) was used to constrain the slip distributions in the fault plane. Similar to the Wei (2012) model, Shao and Ji (2012) only compared their finite fault model results with the waveforms of seismographs.

Fine et al. (2015) focused on studying the near-field characteristics of the Haida Gwaii tsunami. Tsunami observations (DART and ONC buoys) and numerical model simulations were used to study the physical properties of the Haida Gwaii event and test the accuracy of the inversion models present at the time. A modified version of the inversion model of Hayes (2013) was used to define the vertical displacement in the source region (Figure 3.7d). The modelled amplitudes of the study agreed with four observations at DART stations. However, the modelled arrival times differed from the observations. The late arrival time of the tsunami simulations suggested that the location of the earthquake epicentre was different from the one used by Hayes (2013). The inverse isochrones method was used to estimate the exact location and source boundaries. The results indicated that the actual epicentre was 23–25 km to the southeast of the original source model by Hayes (2013). The final finite-fault model was in better agreement with GPS measurements obtained by Nykolaishen et al. (2015). However, the study did not use fine nested grid formulations nor high-resolution bathymetry for tsunami simulations. Thus, the study did not present a detailed comparison between the simulated tsunamis and the observations at each coastal station nor calculated run-up and inundation.

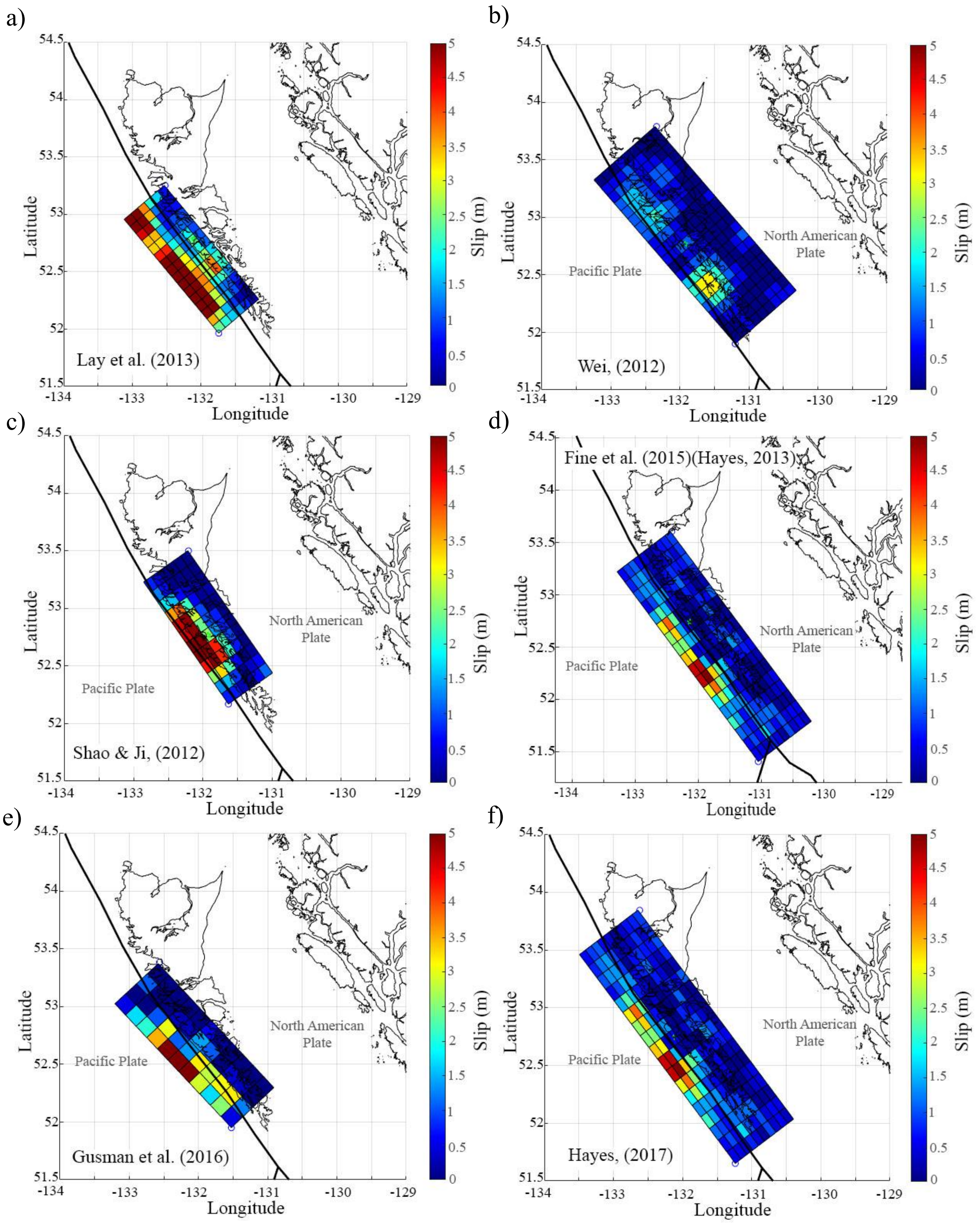

Figure 3.7 Figure 3.8 Finite fault models a) Lay et al., (2013). b) Wei (2012). c) Shao & Ji (2012). d) Hayes (2013) (Fine et al., 2015). e) Gusman et al., (2016). f) Hayes (2017)

Gusman et al. (2016) used tsunami waveforms recorded on seafloor pressure gauges off-shore Oregon and California to test two different real-time tsunami-forecasting methods. The first tsunami source was estimated by inversion of the recorded tsunami waveforms, while in the second method, the data were assimilated to produce tsunami wave-fields (Figure 3.7e). The data used were the tsunami waveforms recorded on DART buoys and absolute pressure gauges. The model had a forecast accuracy vs the data of 94% on average at stations near the coast, which decreased on stations further away. The study demonstrated that tsunami records on dense pressure gauge arrays could deliver timely and accurate forecasts on the nearby coast. However, as this study focused on early warning purposes, the resolution of the finite fault model was coarse. The Hayes (2017) model is preferred for the USGS studies. It used broadband teleseismic data for the inversion analysis, and the finite fault inversion approach was that of Ji et al. (2002) (Figure 3.7f).

3.5 Earthquake Scenario

Several source models that define the Haida Gwaii region can be found in the literature. For the present study, six finite-fault models (Section 3.4) were analyzed. The fault boundaries of most finite-fault models were generated using tsunami data, whereas ground motions were only used in two models (i.e. Shao & Ji, 2012, Wei, 2012). The models' source parameters can be found in Table 3.5. The 2012 Haida Gwaii earthquake occurred on a previously unknown thrust fault dipping to the northeast (Hobbs et al., 2015). The strike of the rupture zone was parallel to that of the QCF. The models' strike ranged from 317º to 325º, consistent with that of the southern segment of the fault where the earthquake occurred. Their hypocentral depth ranged from 15 km to 18 km. The dip of the rupture zone was not well constrained despite the seismic structure and gravity data across the margin (Hyndman, 2015). The model's dip angles ranged from 18º to 30º. Finally, solutions from the Global Centroid Moment-Tensor (CMT) and USGS centroid moment tensor showed almost pure thrust faulting with rakes of 104° and 100°, respectively. However, solutions from Kao et al. (2015) indicated a larger oblique component with the slip vector turning toward the north. These higher values are more compatible with the relative plate motion of the Haida Gwaii region. Thus, the literature models presented larger rakes ranging from 109° to 125° (Table 3.5).

The source parameters such as the fault length (L), width (W), mean slip (Da), maximum slip (Dm), Box-Cox parameter (λ), correlation length along strike direction (Az), correlation length along dip direction (Ax), and Hurst number (H) are evaluated as a function of moment magnitude using the methodology outlined by Goda et al. (2016) (Table 3.6).

Table 3.6 Summary of the finite fault source parameters for the 2012 Haida Gwaii earthquake

Model	Mw	L (km)	W (km)	Da (km)	Dm (km)	λ	Az (km)	Ax (km)	H
Lay et al. (2013)	7.82	144	52	2.88	7.67	0.3	11.52	11.52	0.69
Wei (2012)	7.83	210	90	0.8	3.16	0.1	17.6	17.6	0.99
Shao & Ji (2012)	7.72	144	60	2.15	6.29	0.4	12	12	0.99
Hayes (2013) (Fine et al. 2015)	7.83	252	82	1.12	5.6	0.3	14.28	14.28	0.61
Gusman et al. (2016)	7.8	165	60	1.38	5.43	0.4	10.5	10.5	0.68
Hayes (2017)	7.83	238	65.6	1.12	5.61	0.3	14.28	64.26	0.61

First, the maximum usable wave number is defined based on the original grid resolution of the literature models to check the slip values. Then, the subfaults with zero slips at the edge of the fault are removed to focus on the main slip features of the original model. The slip is evaluated using the effective width and length (Mai & Beroza, 2000).

$$W_E = \frac{\int_{-\infty}^{\infty}(f_W * f_W)ds}{f_W * f_W|_{s=0}} \quad , \; L_E = \frac{\int_{-\infty}^{\infty}(f_L * f_L)ds}{f_L * f_L|_{s=0}} \tag{3.1}$$

where f_W and f_L are the one-dimensional slip function along dip and strike, respectively. $f_W * f_W$ and $f_L * f_L$ are the auto-correlation function of the one-dimensional slip, respectively.

Secondly, the row/ column at the fault's edge is trimmed to find the largest dimension (W or L) that fits the autocorrelation dimensions. The largest fitted dimension is determined, so the difference between the dimension and the autocorrelation is less than or equal to the subfault size. Depending on the size of the model, the effective dimensions can be smaller than the original dimensions. Da and Dm are then evaluated using the new effective dimensions.

Subsequently, the Box-Cox parameter is calculated using a Box-Cox transformation to characterize the probability distribution of slip values on the fault plane and find the best power parameter to transform a non-normal variable into a normal variable.

$$Y = \frac{X^{\lambda-1}}{\lambda} (\lambda \neq 0) \tag{3.2}$$

where X is the original variable, Y is the transformed variable, and λ is the power (Box-Cox) parameter. When $\lambda = 0$ the Box-Cox transformation equates to the lognormal transformation.

Finally, Az, Ax, and H are calculated using a von Karman wavenumber spectrum P(k) (Mai & Beroza, 2002)

$$P(k) \propto \frac{AzAx}{(1+k^2)^{H+1}} \tag{3.3}$$

where k is the wavenumber and is expressed as $k = (A_z^2 k_z^2 + A_x^2 k_x^2)^{0.5}$. Az, Ax, and H are estimated by minimizing the difference between the observed down-dip/along-strike spectrum and the theoretical spectrum. The H is constrained to range between 0 and 1. Finally. a two-dimensional Fast Fourier Transform (FFT) is carried, and the amplitude spectrum is normalized to the maximum value.

Based on the geometry of the finite-fault models, a generic fault model of the Haida Gwaii region is defined for the synthetic source generation (Figure 3.8). The usage of various existing models is favourable because the epistemic uncertainty of source models is considered. The generated fault model covers the whole Haida Gwaii Islands, and its L and W are 315 km and 95 km, respectively. The fault model's geometry is larger than the one predicted for the 2012 Haida Gwaii event (Table 3.6) to allow for a range of geometry for the stochastic source models and to fit various asperity areas for different case scenarios.

The slip at the edge of the models is tapered to zero to avoid abrupt changes in slip values at the fault boundaries (Hayes, 2017). The top edge of the fault plane is positioned at a depth of 3 km, and the strike (325º) and dip (20º) are kept constant. The fault is discretized into 5 km by 5km subfaults for the stochastic modelling and Monte Carlo tsunami simulation.

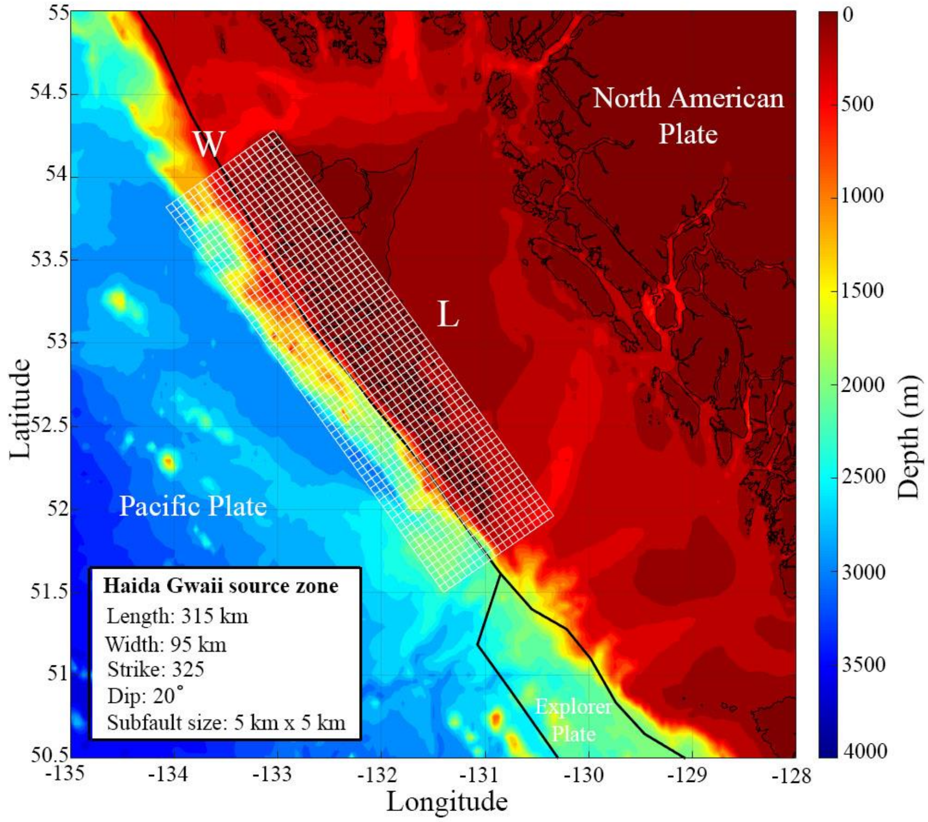

Figure 3.8 Tsunami source zone model for the Haida Gwaii region

Subsequently, the scenario moment magnitude is selected according to the objective of the analysis. For the present study, an Mw range of 7.7-7.9 is considered. Furthermore, within the fault model, an asperity zone is defined (Figure 3.9). The asperity zone constrains the slip concentration within the generated source models, and its definition is not straightforward. The asperity zone needs to accommodate a certain amount of slip that is greater than the specified threshold within the target region and must reflect the seismological characteristics of the region. Thus, the asperity zone must be defined carefully based on geophysical aspects of the 2012 Haida Gwaii earthquake, such as the aftershock sequences (Figure 3.1c). Kao et al. (2015) divided 18 strike-slip aftershocks into four groups: the first group occurred at shallow depths near the surface trace of the QCF with a right-lateral component. The second group occurred on secondary fault zones adjacent to the QCF. The third group occurred within the underthrusting Pacific Plate. The final group was located directly beneath the surface trace of the QCF. All aftershocks occurred on the southern part of Moresby Island, with depths ranging from 5 km to 25 km, just underneath the island’s western coast.

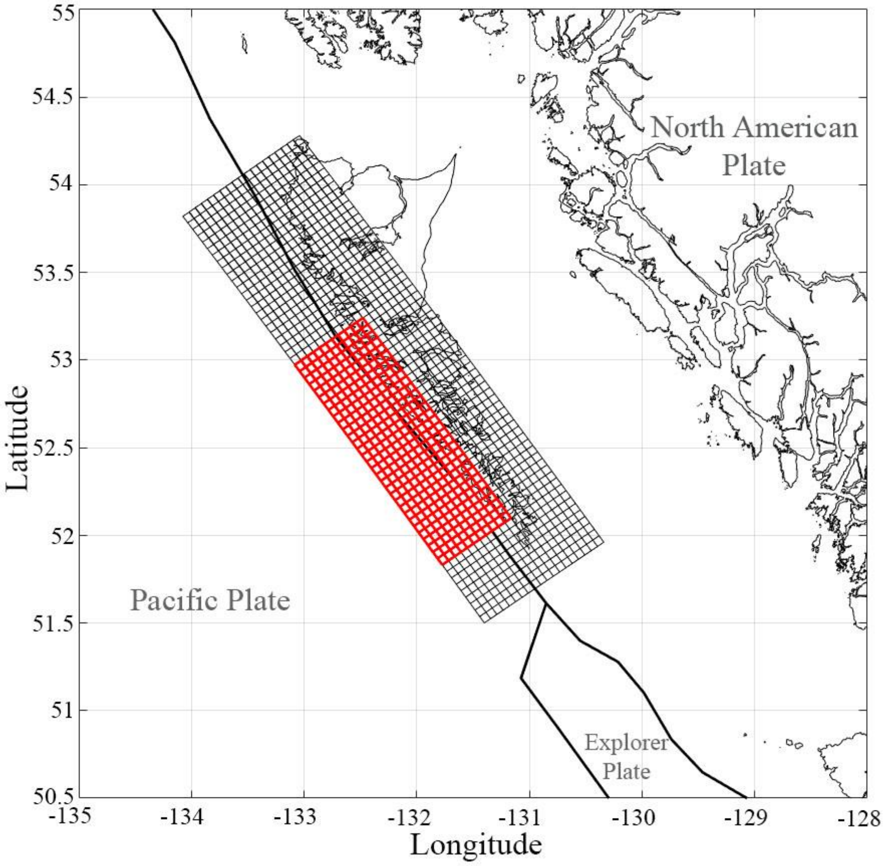

Figure 3.9 Map showing the synthetic fault plane (black) and the asperity zone (red)

Furthermore, the depth of the asperity zone is constrained by high temperatures of the deeper portion that exhibit mostly creep behaviour (Wang et al., 2015). Wang et al. (2015) estimated a depth range of 15-20 km for the depth limit of the rupture zone based on three large strike-slip earthquakes along the fault; thus, confining the rupture zone to a shallow down-dip area (Hyndman, 2015).

The asperity rectangle for the source models is specified as fractions of the fault length and width. In contrast, the extent of the slip concentration around the asperity is specified as a percentage of slip within the asperity rectangle with respect to the total sum of slip over the fault plane. The slip needed to be concentrated within the asperity zone 70% to 100% for the present scenario.

3.6 Source Parameters

After defining the earthquake scenario, fault model and asperity zone. The earthquake source parameters (W, L, Da, Dm, Az, Ax, λ, and H) are generated as a function of Mw using the following scaling relationship derived from global source models (Goda et al., 2016):

$$\log_{10} W = -0.4877 + 0.3125 M_w + 0.1464 \varepsilon_W \tag{3.4}$$

$$\log_{10} L = -\,1.5021 + 0.4669 M_w + 0.1717 \varepsilon_L \tag{3.5}$$

$$\log_{10} Da = -5.7933 + 0.7420 M_w + 0.2502 \varepsilon_{Da} \tag{3.6}$$

$$\log_{10} Dm = -\,4.5761 + 0.6681 M_w + 0.2249 \varepsilon_{Dm} \tag{3.7}$$

$$\log_{10} Az = -\,1.0644 + 0.3090 M_w + 0.1592 \varepsilon_{Az} \tag{3.8}$$

$$\log_{10} Ax = -1.9844 + 0.4520 M_w + 0.2204 \varepsilon_{Ax} \tag{3.9}$$

where the first and second constants are the regression parameters, the third constant is the standard deviation of regression residuals, and ε is the standard normal variable and represents the randomness of the scaling equations. It is important to note that uncertainty associated with the regression models should be considered (Mori et al., 2017b). Furthermore, since some regression residuals are highly correlated, the correlation matrix of such residuals needs to be considered to avoid unrealistic source parameters. Thus, random numbers for ε are sampled from the multivariate standard normal distribution function with the correlation coefficients listed in Table 3.7.

The geometry of the fault is defined by L, W, strike, and dip. The parameters Da and Dm define the characteristics of the slip values. Az and Ax control the power spectrum level by capturing the anisotropic spectral features of the slip distribution in the low wavenumber range. λ is taken as a random variable and is the best power parameter that achieves the maximum linear autocorrelation coefficient. Finally, H is used to model the heterogeneity of the slip values by determining the power spectral decay in the high wavenumber range (Goda et al., 2016). H takes either a deterministic value of 0.99 with a probability of 0.43 or a random value with a mean of 0.714, a standard deviation of 0.172 and a probability of 0.57. Moreover, the prediction errors of λ and H are treated as uncorrelated with other source parameters. Consequently, the generated source models have heterogeneous slip parameters (Goda et al., 2016).

Table 3.7 Linear correlation coefficients of regression residuals of the scaling relationships for the earthquake source parameters

Variables	ε_W	ε_L	ε_{D_a}	ε_{D_m}	ε_{A_z}	ε_{A_x}
ε_W	1.0	0.139	-0.680	-0.545	0.826	0.035
ε_L	0.139	1.0	-0.680	-0.516	0.249	0.734
ε_{D_a}	-0.680	-0.595	-0.595	0.835	-0.620	-0.374
ε_{D_m}	-0.545	-0.516	1.0	1.0	-0.564	-0.337
ε_{A_z}	0.826	0.249	-0.564	-0.564	1.0	0.288
ε_{A_x}	0.035	0.734	-0.337	-0.337	0.288	1.0

3.7 Stochastic Sources

Following the flowchart (Figure 3.10), the slip distributions are synthesized after generating the source parameters. In this step, random-field slip distributions with desirable spectral features are generated. The slip distribution analysis is based on a spectral synthesis of random fields, following Mai & Beroza (2002) and Goda et al. (2014) procedures. First, a Fourier integral method generates random-field slip distributions with desirable spectral features (Pardo-Iguzquiza & Chica-Olmo,1993). The target amplitude spectrum is defined with estimated values Az, Ax and H (Equation 3.3), while phase spectrum is represented by a random phase matrix between 0 and 2π. Subsequently, the constructed matrix of complex Fourier coefficients is transformed into the spatial domain via a 2D inverse FFT (Goda et al., 2014). Multiple random fields are generated until the asperity of the synthesized field falls within the designated asperity zone and its spatial concentration satisfies the slip concentration criteria. Subsequently, the synthesized slip distribution is converted via Box-Cox transformation to achieve realistic features of the slip distribution having positive skewness (Goda et al., 2014). As this transformation potentially leads to very large slip, the transformed slip distributions are adjusted to achieve the target Da and avoid large slip values of Dm. Moreover, the position of the synthesized fault plane is determined (floated) randomly over the allowed fault plane, assuring the slip distributions and locations of the source models are varied.

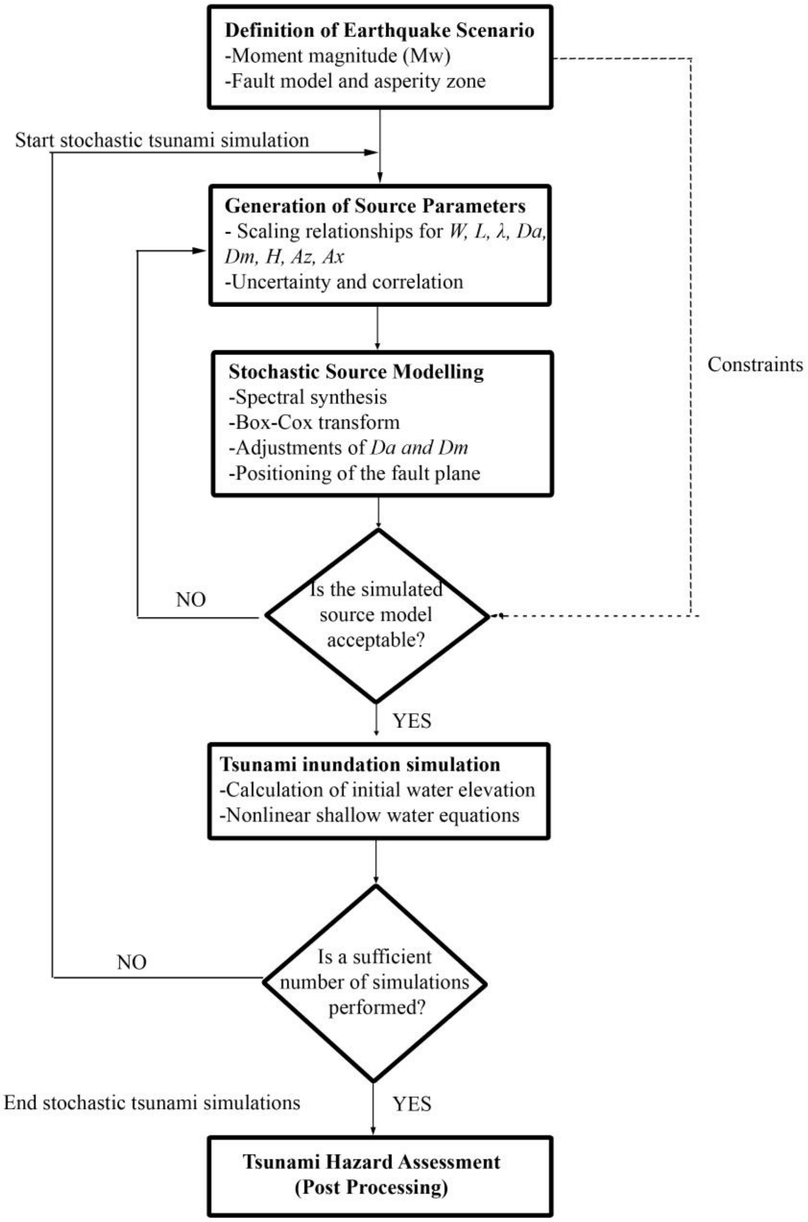

Figure 3.10 Flow chart of the stochastic method

At this stage, the consistency of source parameters (W, L, and Da) is checked by comparing the simulated seismic moment $\left(Mo = \mu WLDa;\ \mu = 4x10^{10}\, {}^{N}\!/_{m}{}^{2}\right)$ against the target moment magnitude of 7.7–7.9. If the simulated Mo does not meet the criteria, the source parameters are generated until the simulated magnitude falls within the target magnitude. Other criteria are implemented at this step to ensure that the synthesized slip distribution is realistic with respect to the seismotectonic characteristics of the region. The first criterion is that the Sa/S ratio of the simulated slip distribution falls within 0.194 and 0.286, where Sa is the average fault area and S is the fault area. The second criterion is that 70% to 100% of the simulated earthquake slip must concentrate in asperity regions. The third criterion is that the difference between the observed and simulated vertical and horizontal deformations must be less than 0.5. Lastly, additional adjustments of slip values are carried out by a taper function to deeper segments of the fault plane. Finally, these steps are repeated until enough acceptable stochastic source models are generated. An acceptable slip distribution is required to have a Dm and similar slip concentration within the asperity zone.

3.8 Monte Carlo Tsunami Simulations

After generating a sufficient number of source models, tsunami simulations are performed using a complete bathymetry and digital elevation models (DEM) dataset. The data are presented as nested grid formulations, covering the entire western coast of Canada all the way to California, USA. The steps for the tsunami simulations are presented in the following sub-sections.

3.8.1 Bathymetry

Tsunami propagation and inundation modelling are highly sensitive to bathymetry and elevation. The resolution of the bathymetry data can introduce significant uncertainty that is difficult to quantify (Griffin et al., 2017). Therefore, accurate high-resolution DEM and bathymetry datasets are required to generate realistic results (AECOM, 2013). For tsunami modelling, the bathymetry data for Pacific coast is obtained from the General Bathymetric Chart of the Oceans (GEBCO) dataset (2020) and is used for deep to shallow water regions. The spatial resolution of the GEBCO dataset is 15 arc-seconds (≈450m). However, a high-resolution onshore elevation is needed for an accurate simulation of tsunami run-up in the shoaling regions near the coastline. Therefore, a 0.75-arc (~20 m) Canadian Digital Elevation Model (CDEM) is used for the onshore topography of the Canadian regions. The

CDEM original data are in orthometric height; the horizontal reference datum is the North American Datum 1983 (NAD83), while the vertical reference datum is the Canadian Geodetic Vertical Datum 1928 (CGVD28). The altimetric accuracy of the CDEM ranges from 0 m to 10 m. Furthermore, 1-arc Shuttle Radar Topography Mission (STRM) DEM is used for the regions in the USA. STRM data are in orthometric heights, the horizontal datum is the WGS84, and the vertical datum is the Earth Gravitational Model 1996 (EGM96).

Potential errors can be introduced in the simulation depending on the dataset resolution (in this case 450 m vs 30 m vs 20 m), the sources from which they are obtained, and the collection date since the morphology and topology are likely to change over time (AECOM, 2013). Hence, the integration of bathymetry and elevation data are not trivial. In addition, the effects of interpolation between the data sets can be significant at shallow depths near the shoreline (Mori et al., 2017b.). Therefore, to minimize the errors in combining the datasets, first, the three datasets are merged without interpolation, and the points are spaced neither regularly nor uniformly. The duplicated values are eliminated during this step. Secondly, at shallow depths, the values of the coarser dataset (GEBCO) are replaced by those of the higher resolution datasets (CDEM for Canadian coasts and STRM for American coasts) and the shoreline data are set as zero elevation data points. Finally, a linear interpolation is performed for the combined datasets to provide a set of nested grids. Linear interpolation is preferred over more complicated methods because it prevents the over-interpolation of topographical features.

3.8.2 Nested Grid Formulations

The tsunami simulations are based on nested computational domains or nested grid formulations. The nested grid system for the Haida Gwaii region uses four grid levels, i.e. 810 m-270 m-90 m-30 m (Figure 3.11). The grid formulations are nested by dividing the large-scale coarse numerical grid by an integer of 3 (1/3 ratio rule) to avoid interference problems in the tsunami simulations (Goda et al., 2016, Fine et al., 2018).

3.8.2.1 810 m Grid

The crudest level is 810 m region and covers the entire Haida Gwaii Islands and part of Alaska, Oregon, Washington, and California. Six 270 m regions, thirteen 90 m regions, and thirty-six 30m are defined within this grid. The extension of the 810 m grid must be sufficient to resolve the feed-back effects from the smaller nested grids on the 810m grid. The deformation due to fault ruptured is computed at the 810 m resolution using Okada (1985) and Tanioka & Satake (1996) equations (Chapter 2). The 810 m grid is enough to simulate deep-ocean tsunami waves since the effects from the topography are not as relevant.

3.8.2.2 270 m Grid

The maximum wave amplitudes for the offshore observations (especially tide gauge observations) are obtained in the six 270 m grids since a finer resolution is needed as the observations are closer to the coast. The location and coverage of the grids are based on the distances of the tide gauges. That is, all stations are within one of the 270 m grids. It is important to note that grids with the same resolution must overlap with each other to ensure that the solutions of the tsunami waves are propagated across different regions properly (i.e. from deep ocean to shelf and into the coast) during the simulations, and no trapping of shorter waves at the boundaries occur (Mori et al., 2017b, Fine et al., 2018).

3.8.2.3 90 m Grids and 30 m Grids

Thirteen 90 m grids are nested within the 270 m grid system. The 90 m grids are used to propagate the tsunami wave from the 270 m grid resolution to 30 m resolution.

The low-elevation coastal areas are covered by thirty-six 30 m grids and have the highest spatial resolutions of all grid formulations. This resolution is used for tsunami run-up simulations as it can properly simulate the wave shoaling process along the coast.

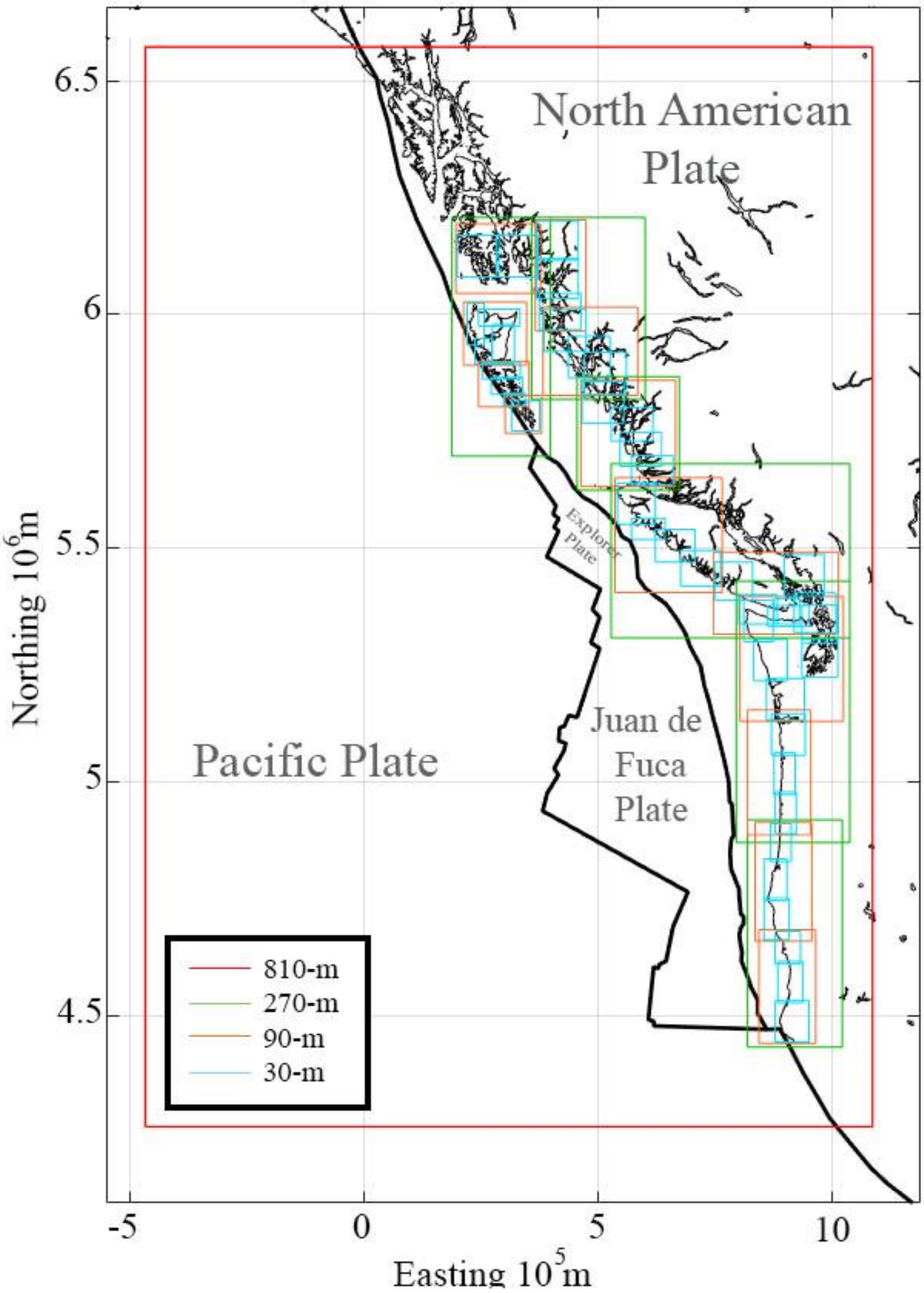

Figure 3.11 Tsunami computational domains (810 m-270 m-90 m-30 m)

3.8.3 Tsunami Inundation Simulation

Tsunami simulations are performed for a set of acceptable source models. First, the initial deformation is computed. The initial boundary conditions for tsunami simulations (initial water elevation) are evaluated using Okada (1985) and Tanioka & Satake (1996) (Equations 2.3-2.9). Afterward, the calculated surface elevation is smoothed using a 9-cell by 9-cell moving average function to avoid steep initial water surface profiles. The numerical computational code developed by Goto et al. (1997) is used for tsunami propagation and inundation. The code uses a leap-frog staggered-grid finite-difference scheme to solve the non-linear shallow-water equations (Equations 2.17-2.19) and simulates the tsunami propagation from the source region to the offshore observation locations and into coastal areas. The run-up is calculated by a moving boundary approach, where a dry/wet condition of a computational cell is determined based on the total water depth relative to the elevation. The bottom friction is evaluated using Manning's formula with a uniform Manning's coefficient of 0.025 $m^{-1/3}/s$. It is important to note that the shallow-water formulations of tsunami propagations by Goto et al. (1997) cannot model the dispersive tsunami waves for far-field tsunami wave profiles (Løvholt et al., 2012)

In the present study, two different simulation set-ups are used; the fault rupture is assumed to occur instantaneously in both cases. The first simulation is to obtain the tsunami wave amplitudes for offshore observation locations (tide gauges, DART buoys, and ONC's BPRs); the resolution of the 270 m grids is sufficient for this case. The numerical calculation is performed for a duration of 6 hours with an integration time step of 1 second. The integration time step is determined by satisfying the Courant-Friedrichs-Lewys criterion. The second simulation case is to obtain the run-up levels. The resolution of the 30-m grids is used for the second simulation. The calculation is set for 2 h for the northern sites and 1 hr for the southern sites, both with an integration time step of 0.1 seconds. No tidal variation is considered for both simulation cases.

The steps mentioned above are repeated for all acceptable source models, and the tsunami amplitudes and inundations at the observational locations are evaluated.

3.9 Results

Performance tests of the stochastic simulations are conducted by evaluating results from the existing finite-fault models against observations (Section 3.4). The best matching model is then compared against the stochastic models. The model by Gusman et al. (2016) agrees well with the 2012 Haida Gwaii tsunami observations and thus is used to test the ability of the stochastic source models to match the observations (further explanation in the following section).

A brief discussion of the key features of the synthetic/stochastic earthquake slip models for the 2012 Haida Gwaii earthquake is given. Then, the synthetic tsunami characteristics are analyzed by comparing the tsunami simulation results with the existing observations of the 2012 event. Finally, to highlight the sensitivity of tsunami inundation to asperity areas, an evaluation of the earthquake slip and fault geometry effects on coastal tsunami wave heights along the Haida Gwaii region is carried out by comparing tsunami inundation against run-up measurements (i.e. large slip areas).

3.9.1 Literature Finite-Fault Models

First, the tsunami simulations from the six literature source models are carried out for the 16 offshore observation stations (Figure 3.2). Then, the results and the observations are compared against each other to find the best matching model (see Appendix A for the complete results). Six observation sites (i.e. Queen Charlotte, Henslung Cove, Crescent City, Cascadia Basin, Barkley Canyon, DART 46410; see Figure 3.2 for locations) are chosen to illustrate the variation of the tsunami amplitudes based on their location along the northwestern Pacific and to show the performance of each of the model to be able to produce tsunami waves close to those of the 2012 event.

Special attention is given to the Queen Charlotte station (Figure 3.12) since the amplitudes right after the rupture present negative values (a trough), which is interpreted as the subsidence after the earthquake. The Gusman et al. (2016) model is the only model that does not present this. Thus, a greater weight was given to this station in choosing which is the best model to test the performance of the stochastic source models.

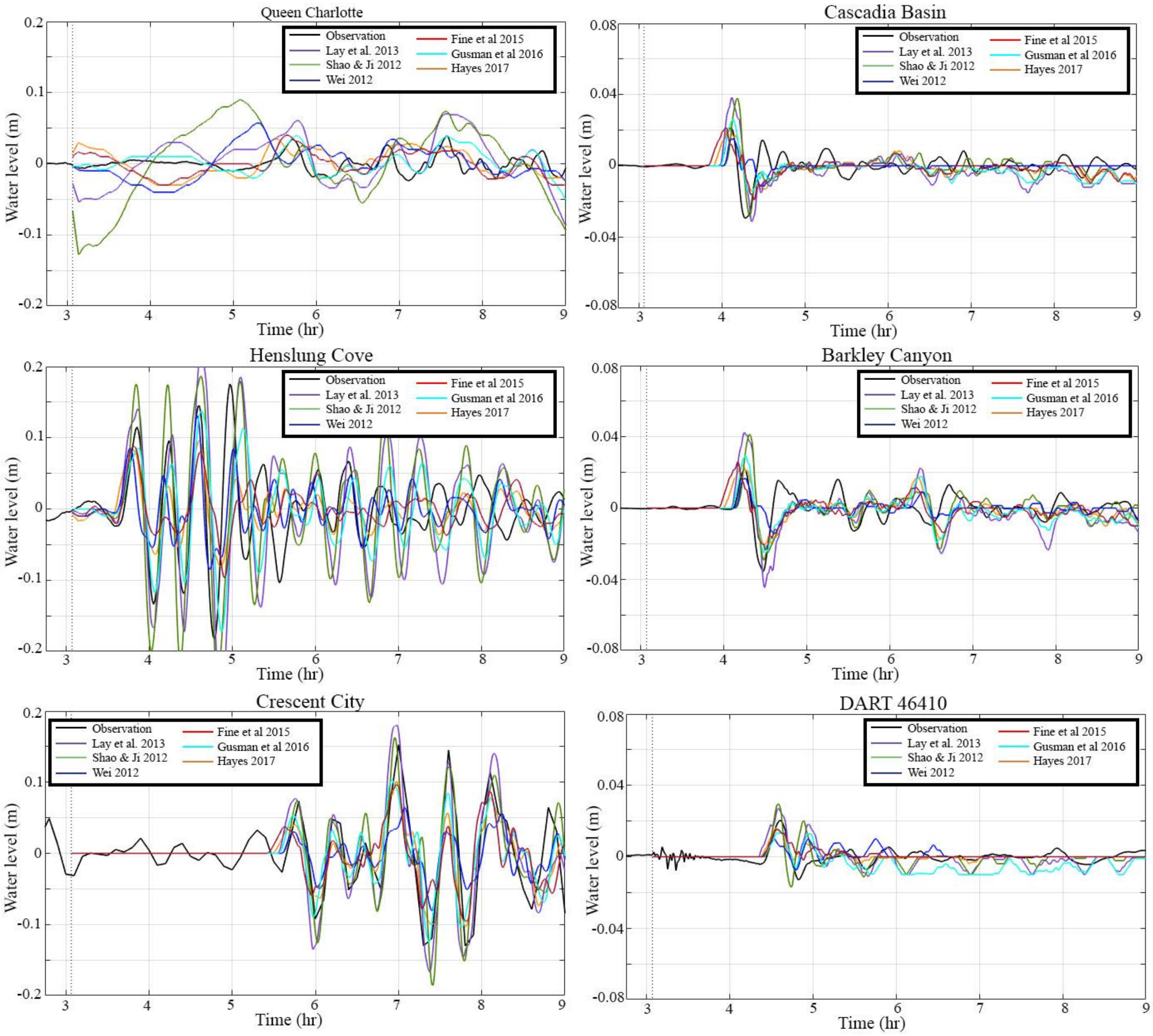

Figure 3.12 Tsunami waveforms at Queen Charlotte, Henslung Cove, Crescent City, Cascadia Basin, Barkley Canyon and DART 46410 stations and literature models

Next, the horizontal and vertical deformation of the models (Figure 3.13) are compared to the observed deformations (See Appendix A for complete results). Some models (i.e. Wei, 2012, Shao & Ji, 2012, Hayes, 2013 [Fine et al., 2015], Hayes, 2017) have uplift on the northern and southern parts of the island, which was not present in the observations. The uplift presented in some models on the northern part of Haida Gwaii can be explained by the source models' length extending more than the actual rupture zone. In contrast, the source models extending significantly beneath the island can explain the uplift on the southern part. Whereas the models by Lay et al. (2013) and Gusman et al. (2016) present only subsidence, which means that the extension of the fault plane is limited to right beneath the coastline.

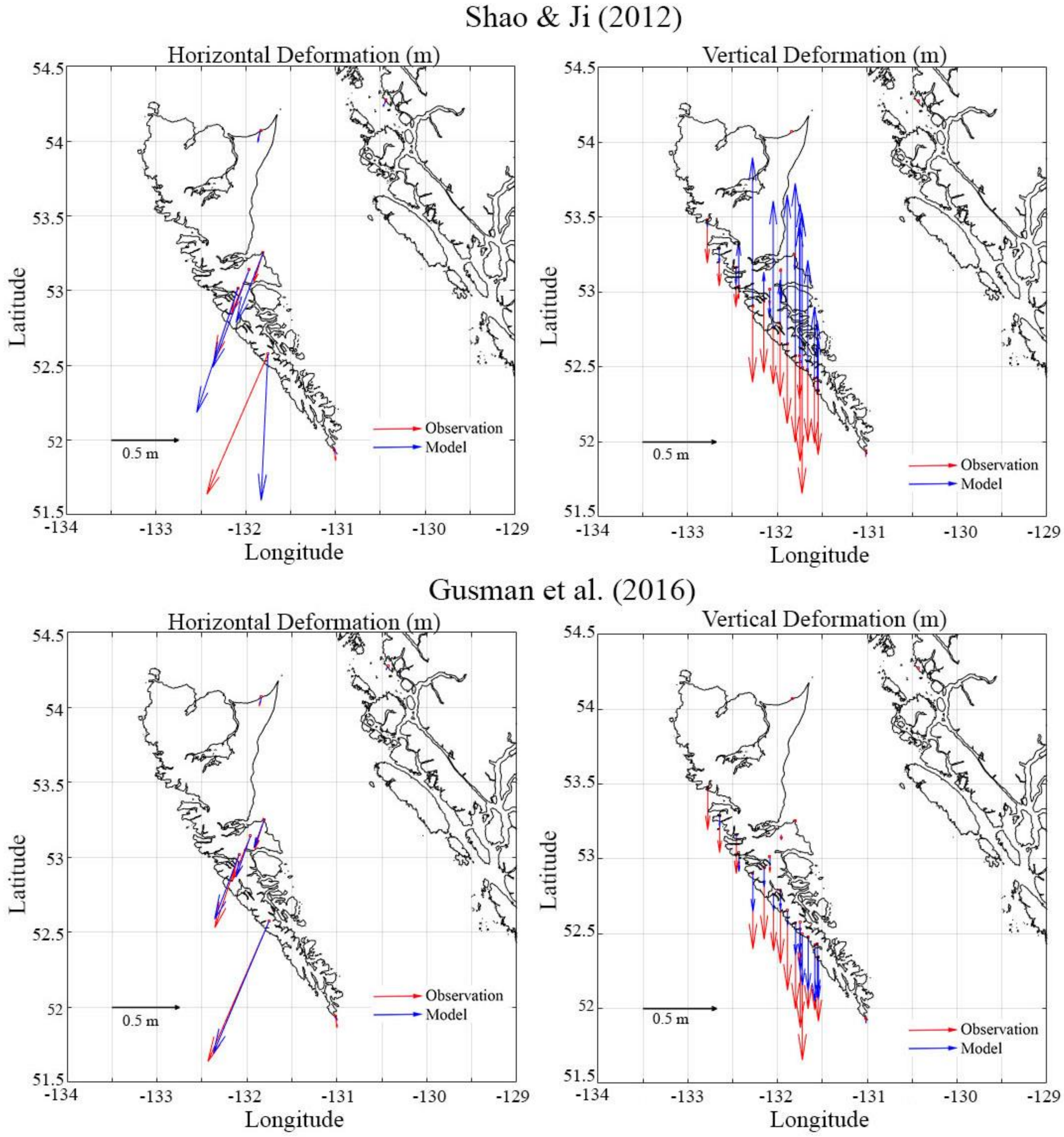

Figure 3.13 Horizontal and Vertical deformation vectors of the observations and source models from the literature

The sum of square errors (sse) between the observations and the literature models is calculated to find the best matching model. In addition, the error ratio between the deformation observed and the simulated by the models is also considered. The model with the lowest sse (0.902) is the Gusman et al. (2016) model. Therefore, based on the tsunami simulations, the deformation, and the Queen Charlotte station, the Gusman et al. (2016) model was deemed the best matching model; thus, it was used to investigate the performance of the stochastic source models to match both the observed deformations and tsunami amplitudes.

3.9.2 Simulated Stochastic Source Models

A total of 1000 stochastic sources are generated for Mw 7.7 to 7.9 earthquakes, out of which 128 stochastic sources are chosen to perform Monte Carlo tsunami simulations. A summary of the simulation parameters for the stochastic slip synthesis is presented in Table 3.8. The simulation parameters are determined based on the six literature models, temperature gradients, and aftershock sequences. All stochastic models consider uncertainty and have diverse dimensions, slip distributions, slip heterogeneity, and locations. The slip distributions used for Monte Carlo tsunami simulations are chosen based on the maximum slip that fits the scenario Mw. The chosen slip distributions show how the slip values and fault planes differ for similar Mw values. Consequently, the variations in slip distributions can better account for the uncertainties of the source region. The models' features are controlled by the stochastic synthesis parameters and target slip, which significantly influence the tsunami simulation results (Goda et al., 2014). Figure 3.14 shows the variations in location, asperity sizes, and the maximum slip of some examples of the stochastic source models. In general, models that closely match the observations are constrained to the oceanward part of the fault and have major slip values within the asperity region. The extension of the fault is also limited by the coastline and does not extend too far beneath the islands, consistent with the coseismic subsidence deformation (Figure 3.14).

Table 3.8 Summary of stochastic earthquake slip simulation parameters

Model Parameter	[Lowe, Upper]
Mw	[7.7,7.9]
Slip ratio	[0.7,1.0]
Ratio L/W	[0.5,3.0]
Az to W range	[0.35,0.5]
Ax to L range	[0.2,0.5]

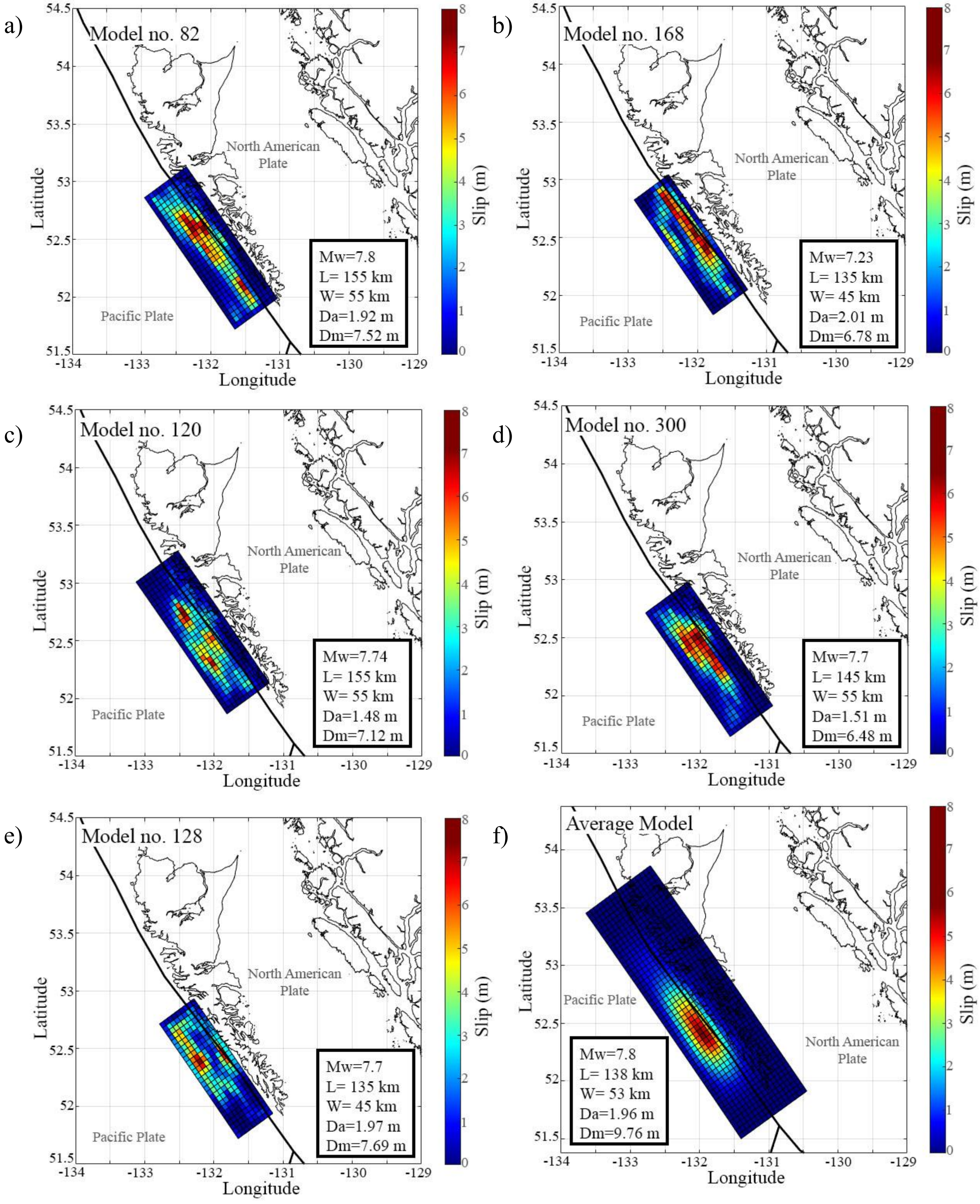

Figure 3.14 (a-e) Five stochastic models (Mw 7.7-7.9), and (f) overall average slip models based on the 1000 stochastic sources

The vertical and horizontal deformations are constrained to an error ratio of 0.5 between the target and simulated deformation values. Therefore, the source models have slip distributions that produce deformations close to that of the 2012 event. Furthermore, models that closely match the deformation also match the tsunami simulations (Figure 3.15).

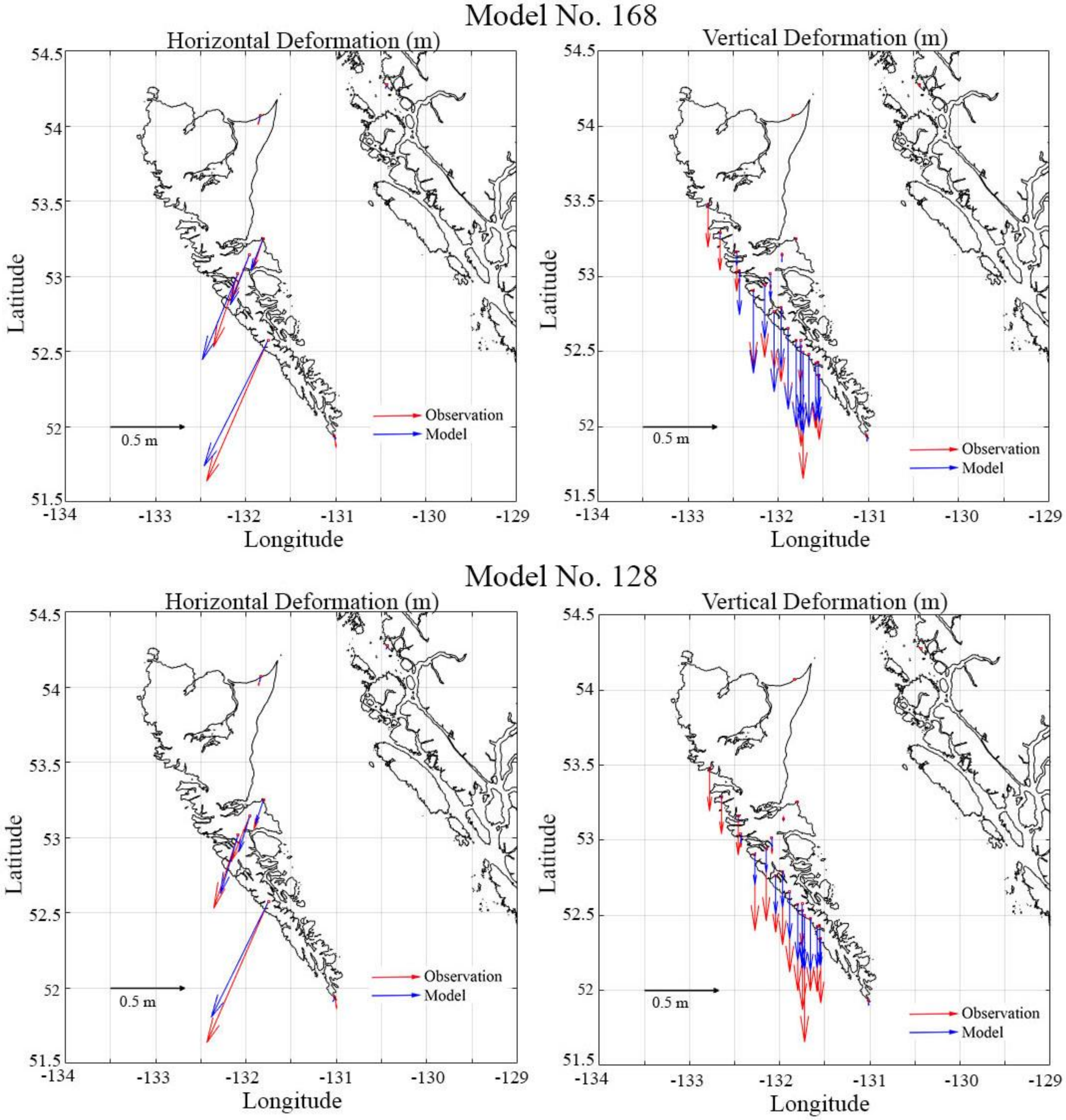

Figure 3.15 Horizontal and vertical deformations of observations and stochastic models

Figure 3.14f shows the average source model generated by calculating the average slip of every subfault of each of the 1000 stochastic source models. Most of the slip is concentrated in the asperity region and is limited to the fault's shallow side, consistent with the observed aftershock sequences and thermal gradients of the zone. The overall Da is 1.96 m and falls within the ranges used in past studies (Table 3.6).

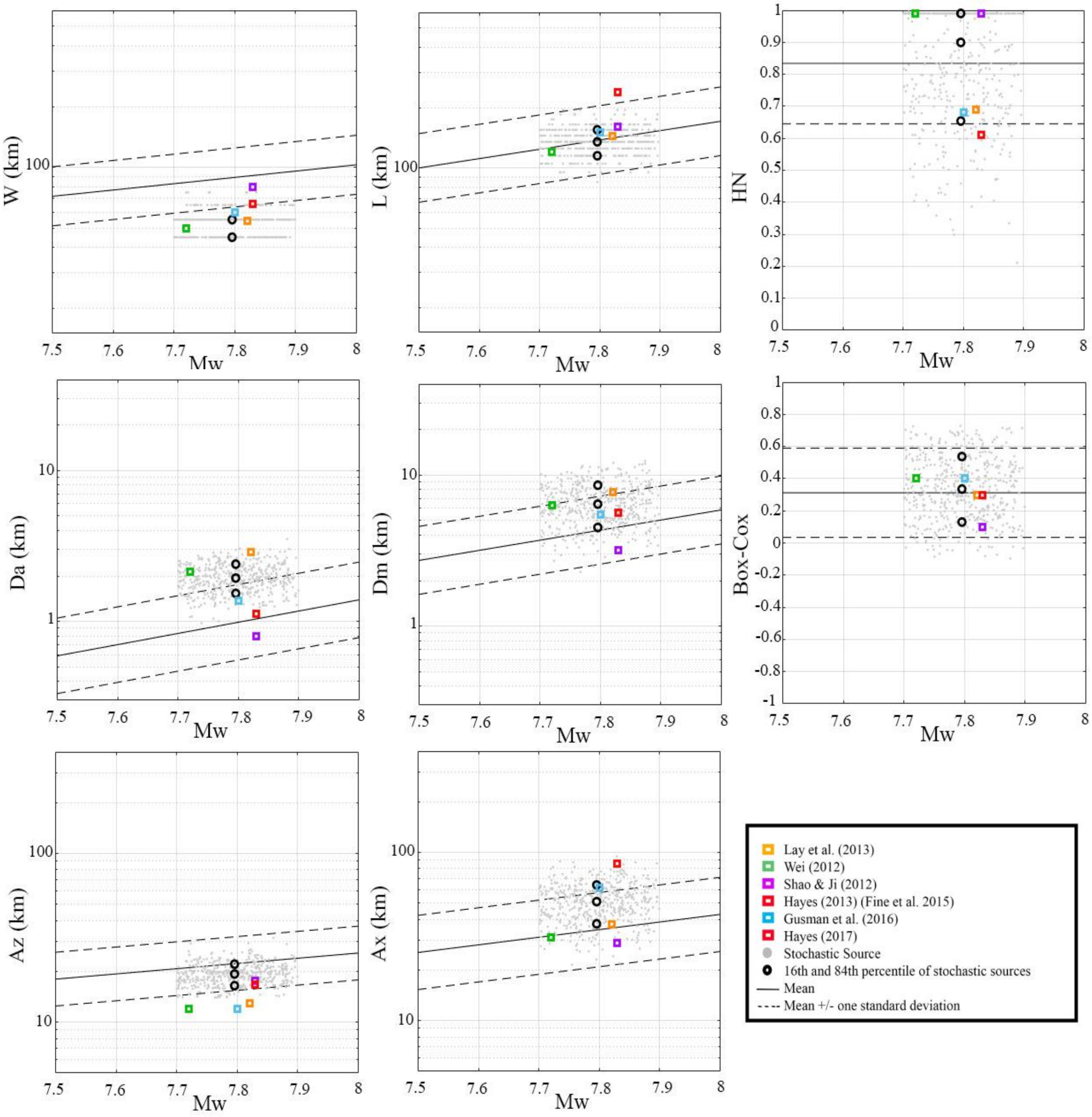

Figure 3.16 Comparison of estimated source parameters for the stochastic models and six models from literature against the corresponding global scaling relationships

The overall Dm of all the slip distributions is 9.97m, and it is larger than Dm of the past models. It is important to note that the models used for the Monte Carlo tsunami simulations are chosen based on whether the model's Dm fell within the ranges of the global scaling relationships for events of the same magnitude (Equation 3.7). The overall Mw is 7.76, consistent with Mw considered in the six literature models (Mw 7.8). The overall length is 138 km, while the width is 53 km. Both dimension parameters are smaller than the ones from the six literature models. However, they better fit the dimensions of the predicted fault plane of 120–145 km length and 30 km width (Kao et al., 2015). The vertical and horizontal deformations are constrained to an error ratio of 0.5 between the target and simulated deformation values. Therefore, the slip models have slip distributions deformations close to those of the 2012 event. Furthermore, models that present uplift are not accepted during the stochastic source synthesis, further scrutinizing the stochastic models. Consequently, models that closely match the deformation also match the tsunami simulations (Figure 3.15).

Figure 3.16 shows how the stochastic and literature models compare with the global scaling relationships developed by Goda et al. (2016). The parameters for most stochastic source models fall within the scaling equations' prediction intervals (16th and 84th percentiles) in comparison to the six models. The models by Hayes (2017) and Hayes (2013) (Fine et al., 2015) have larger lengths than those expected from earthquakes of the same magnitude and larger Az, which can contribute to the uplift present on the northern part of the islands. The models' width (W) is considerably smaller than those of the scaling relationships, especially for the models of Shao & Ji (2012) and Lay et al. (2013). Thus, an increase in slip values (Da and Dm) and a decrease in Ax values are expected. The increase in slip concentrates tsunami waves (Momeni et al., 2020), which explains the higher amplitudes produced by both Shao & Ji (2012) and Lay et al. (2013) models (Figure 3.12). On the other hand, the larger W of Wei (2012) model results in lower Da and Dm, hence the overall lower tsunami amplitudes.

3.9.3 Offshore Tsunami Result: Comparison with Observations

Due to time constraints from the 1000 stochastic source models, only 128 models are chosen for Monte Carlo tsunami simulation based on their Dm. Thus, models that have Dm within the expected Dm value for earthquakes of the same magnitudes are chosen over those that have exceeding Dm. The tsunami wave characteristics of the 128 models are first examined for offshore locations (i.e. tide gauges, DART stations, and ONC BPRs). In general, the observations can be enclosed by the stochastic method. However, some models perform better than others. Therefore, a comparison between the observations and each model is preferred to find a set of the best matching models. The sum of squared errors (sse; Equation 3.10) between the observed and simulated first wave amplitude are calculated to identify the best matching source model for the 2012 event among the stochastic slips (Table 3.9).

$$sse = \sum\left(Observation(amplitude) - simulation\ (amplitude)\right)^2 \qquad (3.10)$$

Special attention is given to the Queen Charlotte station since some models start with trough. Therefore, the *sse* of the first-hour wave amplitudes at the Queen Charlotte station is also calculated and given greater weight. The tsunami waves that do not present this trough at Queen Charlotte are the primary indicator for identifying the best matching source model for the 2012 event. The *sse* values of all the stations for a given model are summed. The stochastic source models are then ranked based on their calculated error metrics (examples of best models are given in Figure 3.14). The deformation *sse* during the stochastic source modelling is also considered in finding the best matching models. Ultimately, two source models are chosen as the best models for offshore observations and deformation. Model 168 has the lowest sse values (Table 3.9; Figure 3.14b); the model matches the deformation best out of the models chosen for the tsunami simulation. In contrast, Model 128 best matches the tsunami observations (Table 3.9; Figure 3.14e).

Figures 3.17 and 3.18 show the simulated time series of wave amplitudes at different stations (i.e. Henslung Cove, Queen Charlotte, Winter Harbour, La Push, Port Orford, Crescent City, Barkley Slope, Clayoquot Canyon, Cascadia Basin, DART 46419, DART 46410, DAR4611; see Figure 3.2 for location). The stations are chosen to illustrate the variability in wave amplitudes with relation to the distance from major asperity zones. In Figures 3.17 and 3.18, the individual tsunami wave profiles are shown in gray, the wave profiles of the Gusman et al. (2016) model are shown in red, the best matching models in green and orange, while the statistics (mean, 90th percentile, and 10th percentile) of the tsunami simulation results are indicated in black to show major trends of the tsunami wave profiles.

Table 3.9 Sum of square errors of the tsunami observations and deformation for the six literature models and best stochastic source models

Models	Deformation	Tsunami Observations	Total
	sse	sse	
Lay et al. (2013)	1.602	1.221	2.824
Wei (2012)	7.024	1.096	8.119
Shao & Ji (2012)	12.268	1.13	13.397
Hayes (2013) [Fine et al. 2015]	2.232	1.211	3.443
Gusman et al. (2016)	0.69	0.212	0.902
Hayes (2017)	2.331	1.225	3.556
Model 82	0.427	1.138	1.564
Model 120	0.533	1.121	1.654
Model 128	0.564	0.189	0.753
Model 168	0.303	0.208	0.511
Model 300	0.555	0.201	0.756

The results indicate that the mean wave amplitudes are similar to the observations. Therefore, the simulations can closely match the observations. Although the average wave profiles are not so large, some tsunami waves have larger amplitudes than the 90th percentile wave. Nevertheless, the difference between the exceeding waves and the observations is still small because the observation amplitudes are relatively small. As expected, stations closer to the source (asperity areas) have relatively larger amplitudes (i.e. Winter Harbour and Henslung Cove). Moreover, the high amplitudes might also be related to the stations' location in the direct path of tsunami propagation. For the Queen Charlotte station (Figure 3.17), some models capture the deformation (subsidence) during the earthquake, interpreted as the slip distributions extending too far beneath Haida Gwaii's western coast (comparison between Figure 3.14 and 3.19), explaining the negative values at the beginning of the simulations.

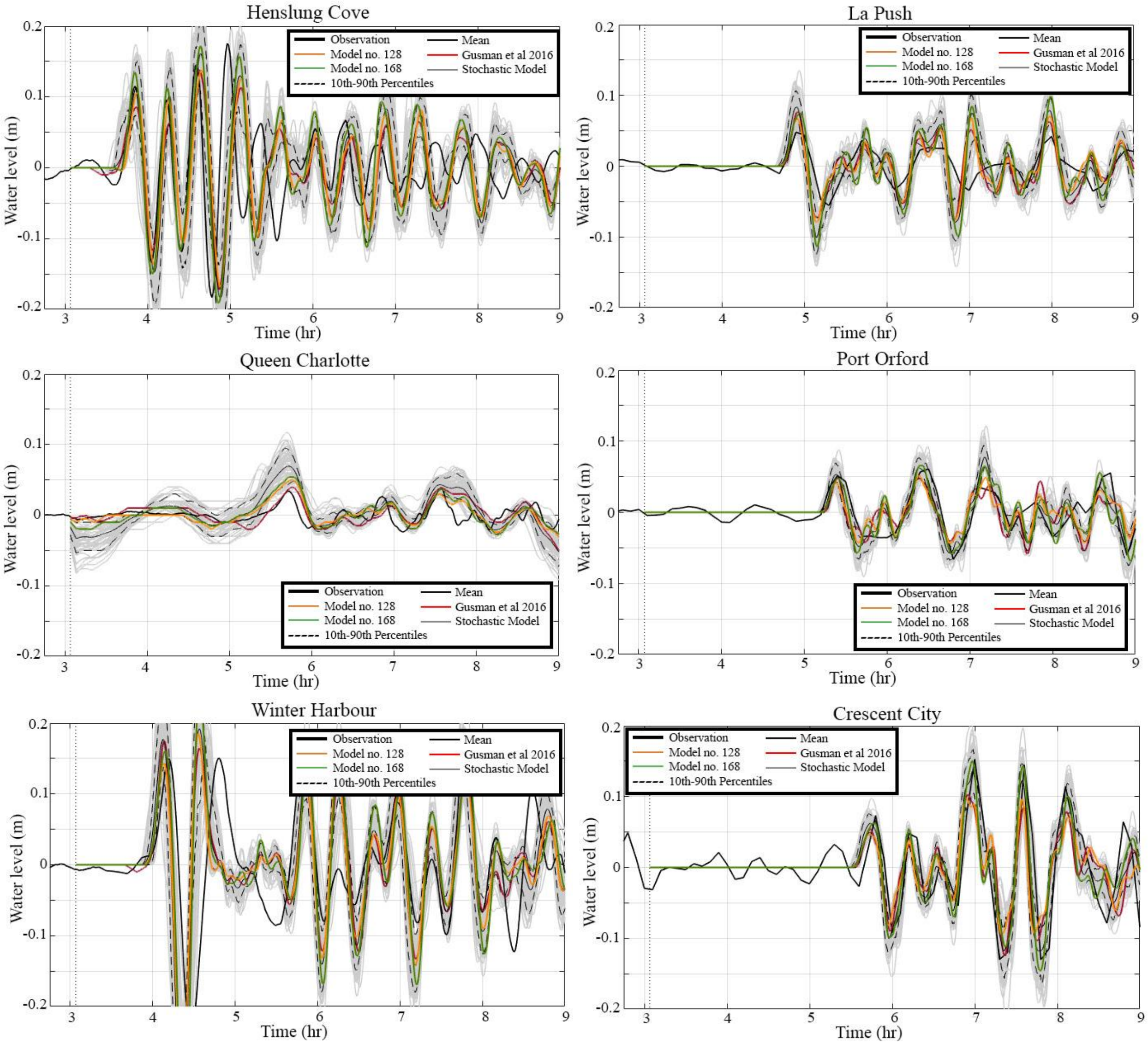

Figure 3.17 Comparison of time histories of tsunami wave for the 128 and 168 stochastic models (mean, 90th percentile, and 90th percentile) and the Gusman et al. (2016) model with the observations at different tide gauges

Furthermore, the first wave amplitudes and the mean arrival times of the first wave are close to the observations. However, the arrival times of the simulated first wave for the station Ketchikan (Appendix A) are all early. Stations like DART 46410 and DART 46411 (Figure 3.19) have the most models with the smallest *sse*, while stations like Henslung Cove and Winter Harbour (Figure 3.18) have the most stations with the largest *sse*. The

Model 128 better matches the observations at stations like DART 46410, Cascadia Basin, Henslung Cove, Barkley Canyon, and Cascadia in comparison with the Gusman et al. (2016) model, while at stations like Tofino, Port Orford, and Crescent City, the model performs close or the same as the Gusman et al. (2016) model. On the other hand, Model 168 performs better at stations like Port Orford, Crescent City, and similar to Gusman et al. (2016) model at stations like DART 46404, DART 46411, and DART 46419 (see Appendix A for waveforms for Tofino).

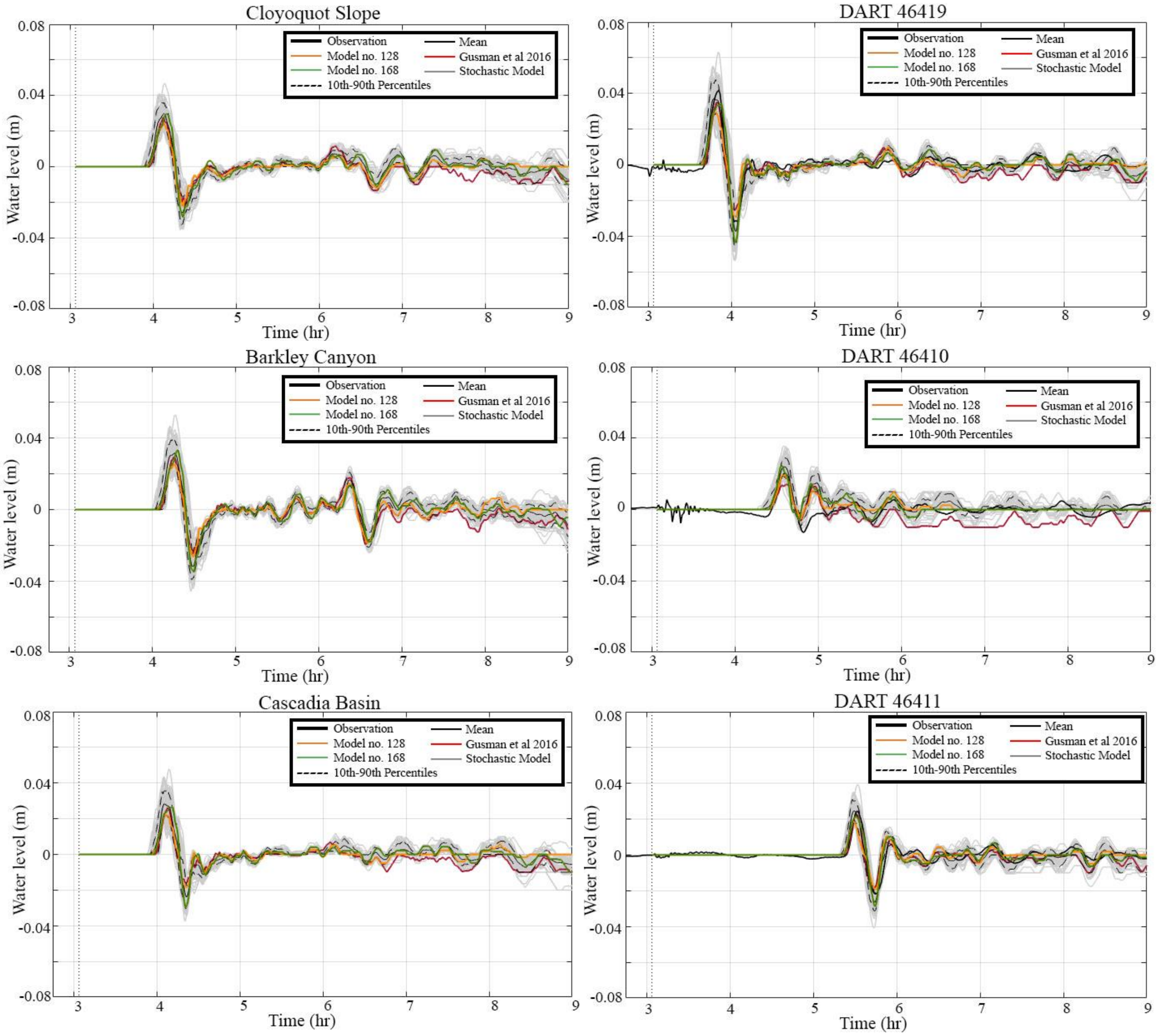

Figure 3.18 Comparison of time histories of tsunami wave for the 128 and 168 stochastic models (mean, 90th percentile, and 90th percentile) and the Gusman et al. (2016) model with the observations at different ONC BPRs and DART buoys

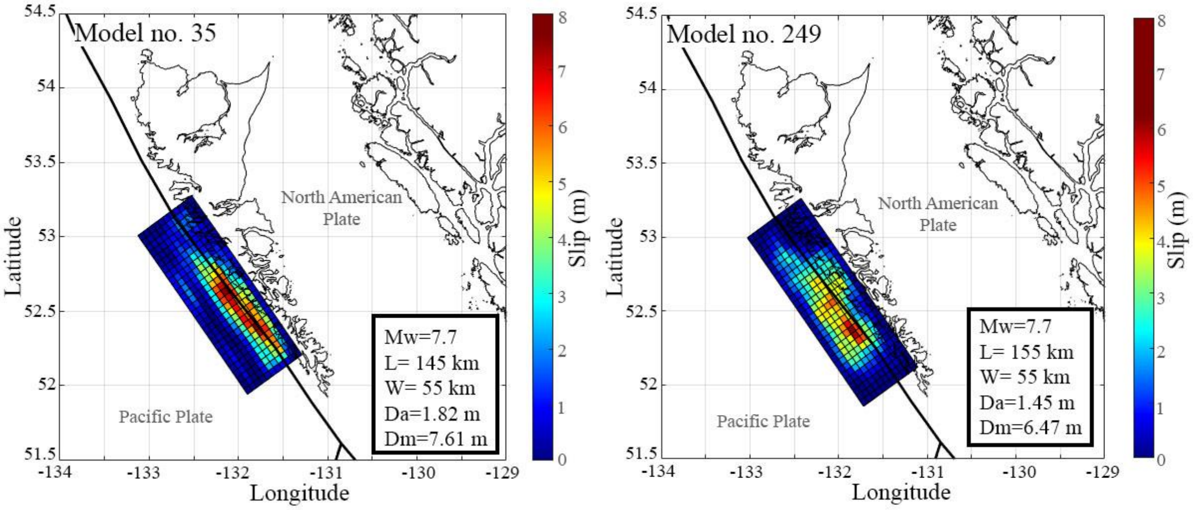

Figure 3.19 Figure 3.20 Stochastic source models for the 2012 Haida Gwaii earthquake with slip distributions

Neither of the models present abnormal values for the Queen Charlotte station; thus, the slip distributions do not extend too far beneath islands. The *sse* between the models and the observation is 0.753 for Model 128 and 0.511 for Model 168, while the *sse* for the Gusman model is 0.902.

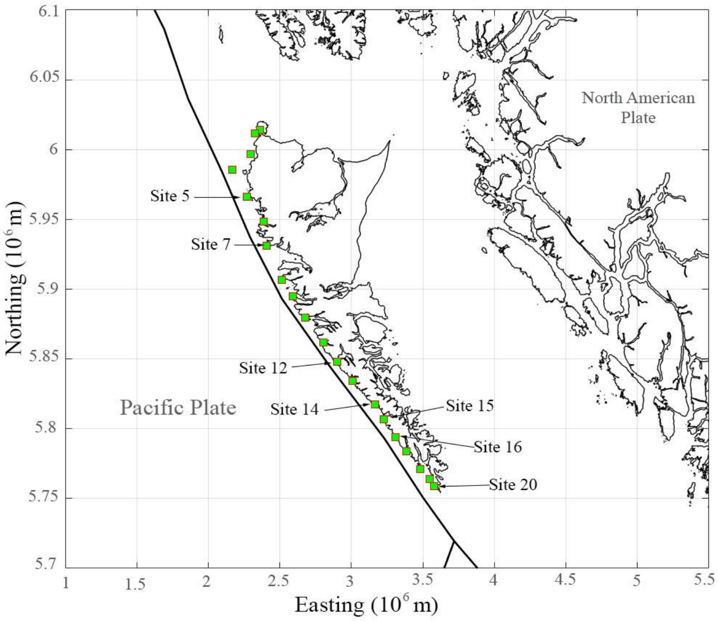

Figure 3.20 Sites near the coast of Haida Gwaii

The wave amplitudes for nearshore locations are calculated for the eight best models based on the ability of the models to match the offshore observations. For the analysis, 20 sites along the coast are chosen with depths of 30 m ± 10m (Figure 3.20). The sites are distributed all along the western coast of Haida Gwaii, close to the run-up observational sites. The results from the eight models are shown in gray, while the results from the Gusman model are presented in green (Figures 3.21-3.22; see Appendix A for all sites). The sites are chosen to explain further the variation of tsunami amplitudes due to the location of major asperities. As expected, the results show that sites like Site 5, 7, and 20, which are further away from the major asperity zone, have smaller wave amplitudes (i.e. northern sites, Figure 3.21a).

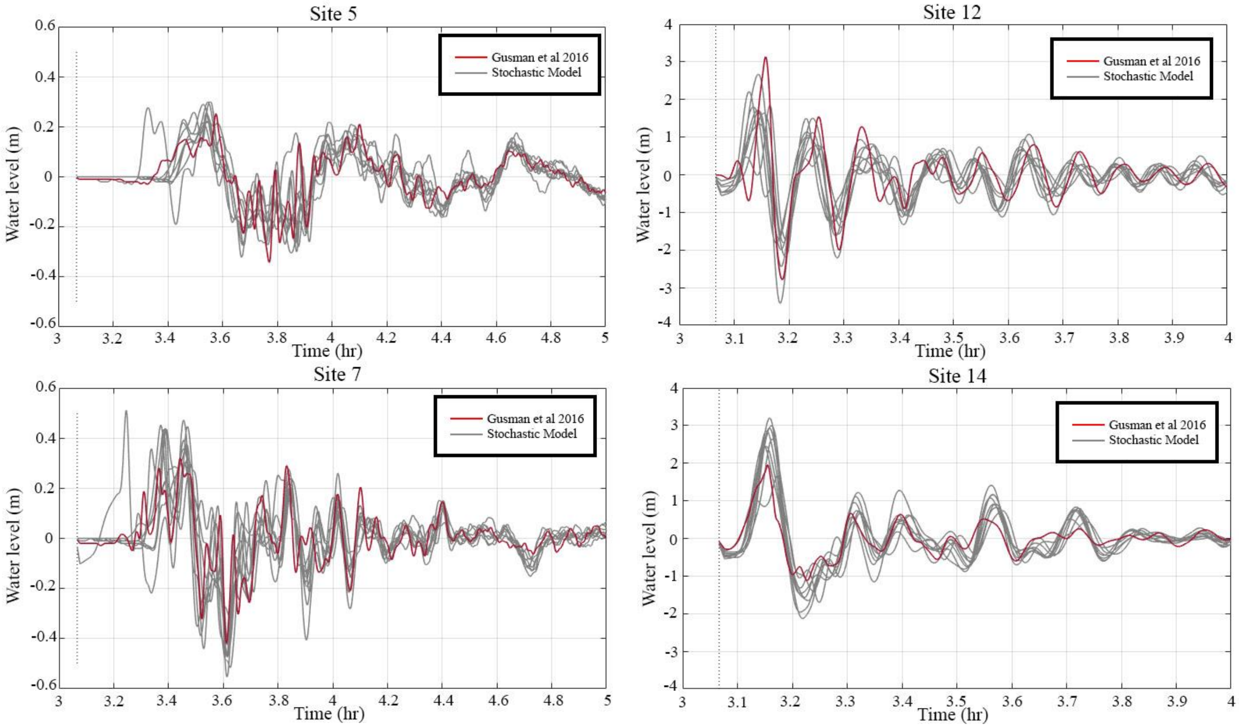

Figure 3.21 Time histories of tsunami waves for sites 5, 7,12, and 14

The amplitudes become significant as the sites get closer to the epicentre and major asperity regions. The largest amplitudes are recorded at sites like Sites 14, 15, and 16 (Figure 3.21b and Figure 3.22). Generally, the sites to the north have smaller amplitudes compared to the southern sites. Thus, the tsunami propagation path was mainly directed southward, consistent with the large amplitudes recorded in places like Hawaii (Lay et al., 2013). In addition, some models present earlier arrival times of the first wave's amplitude than other models, which is interpreted as the epicentre location of such models being too close to the coast.

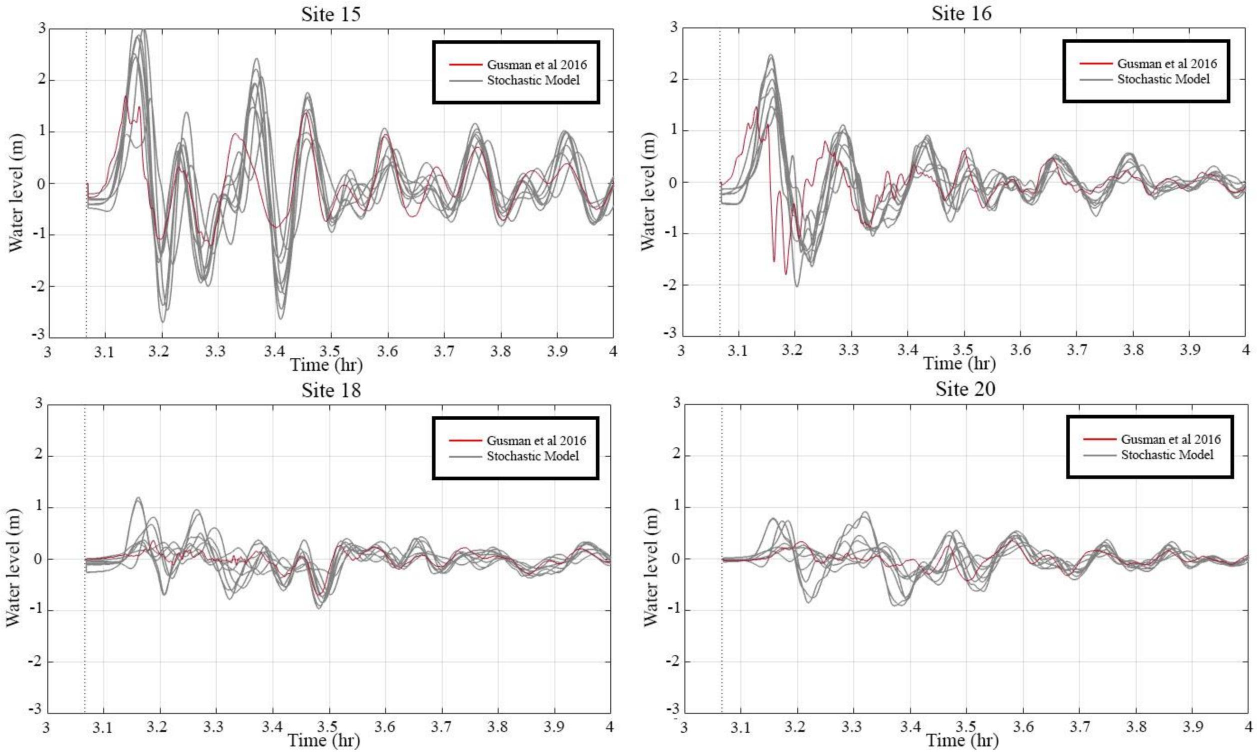

Figure 3.22 Time histories of tsunami waves for locations 15,16, 18, and 20

The maximum coastal tsunami wave heights along the coastline of Haida Gwaii are generated by the eight stochastic models and the Gusman et al. (2016) model (Figure 3.23). Note that the tsunami wave height that is discussed in this study is the height of water flow above mean sea level. The maximum heights are calculated at 217 sites along the western coastline of Haida Gwaii with approximately 10 m (±5m) depth. The results are shown in gray in Figure 3.23 alongside the Gusman et al. (2016) model in green. The maximum tsunami wave heights range from less than 1.0 m to 5.5 m. The maximum tsunami heights for the southern part are higher than the northern part due to large slip areas on the southern part (Figure 3.14), which are determined by the asperity region (Figure 3.9). The Gusman et al. (2016) model has larger heights at coordinates $5.85x10^6$, while the stochastic models have the largest heights at coordinates $5.82x10^6$. Both stochastic and Gusman et al. (2016) models have similar amplitudes on the northern and southern limits.

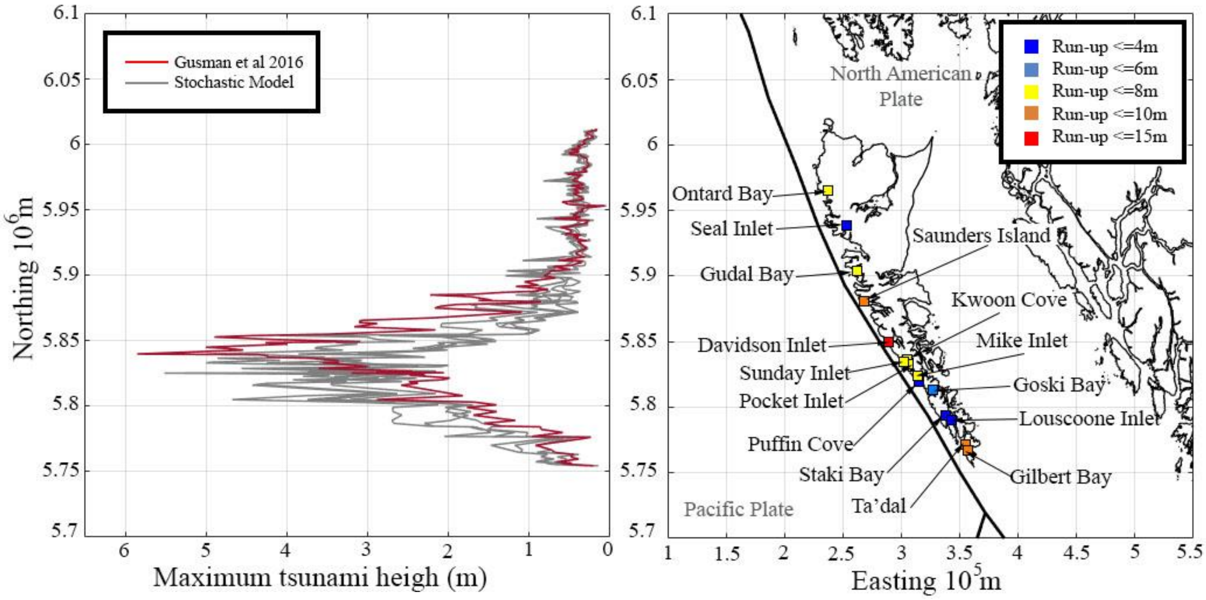

Figure 3.23 a) Maximum coastal tsunami wave heights generated by the eight stochastic models and the Gusman et al. (2016) model, and b) sites along the shoreline of Haida Gwaii

Figure 3.24 shows the maximum wave amplitudes for the stochastic source models in Figure 3.14 (See Appendix A for Model no. 300). Since no models had slip values on the northern side of the QCF, the amplitudes for the models are relatively low in the northern region, with wave heights less than 2 m. In comparison, zones directly in front of the rupture have larger tsunami wave heights. Consequently, larger tsunami run-ups are expected in the region. The run-up measurements in the zone differ significantly between sheltered sites and exposed sites from storm waves (see Section 3.3.4). Exposed sites reported run-ups of up to 7.37 m (Leonard & Bednarski, 2014, Table 3.4), whereas sites sheltered from storm waves reported run-ups of 3.59 m, which agree more with the simulated maximum water heights; this will be further discussed on the next section. Since most models had major asperity areas on latitude 52.5º (Northing 5.83x10^6 m), the largest heights for most of the models are on those areas (see Figure 3.24). The largest run-up reported is also within this zone (i.e. 12m at Davison Inlet, Leonard & Bednarski, 2014); however, it is important to note that the site was exposed to storm waves, which could result in such a high value.

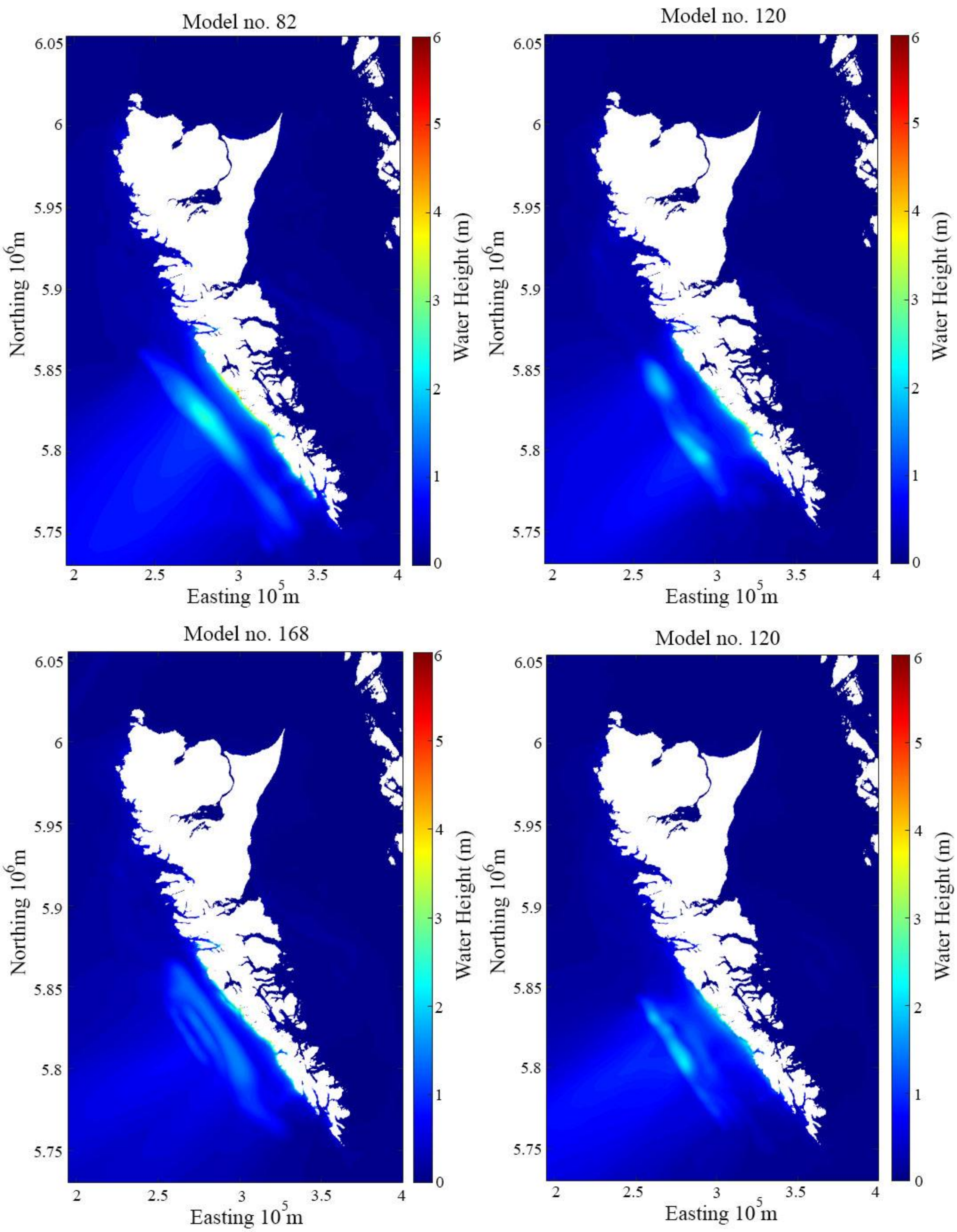

Figure 3.24 Maximum wave height for the Haida Gwaii region

3.9.4 Onshore Tsunami Results: Comparison with Run-up Observations

To study the variability of tsunami inundation with changing asperity zones, the tsunami inundation for different bays and inlets, where run-up observations were collected (see Section 3.3.4), is calculated for the eight best matching models from the previous section. Tsunami inundation in coastal areas is affected by three main factors: the source (large slip) characteristics, the bathymetry features of the coastal area, and the shape of the bay (Mori et al., 2017b, Momeni et al., 2020). The Haida Gwaii topography consists of cliffs and fjords, which could amplify the tsunami inundation within the bays and inlets. The tsunami inundation is calculated from different points along the bays and inlets. The inundation average for the bay or inlet is compared against the run-up reported by the field surveys. Overall, the highest inundations are observed on sites near the epicentre, where the highest slip values are concentrated, with inundation heights of up to 4.56 m (i.e. Kwoon Cove and Pocket Inlet, see Figure 3.6 for the locations). On the other hand, sites north of the Haida Gwaii region, which have small or no areas of concentrated slip, have lower inundations than the southern sites. The differences correlate to the water heights from Figure 3.24.

The run-up observation sites are divided into sites sheltered from storm waves and sites exposed to storm waves (Leonard & Bednarski, 2014). The highest run-up heights were generally at sites exposed to storm waves (Table 3.4). The comparison of the simulation results against the observations shows a significant difference, particularly at sites exposed to storm waves. Overall, the simulation results are lower than those reported by Leonard and Bednarski (2010; Table 3.10), with differences ranging from 3 m to 7 m. It is important to note that there is some uncertainty in the run-up observations, especially at sites exposed to storm waves, because the field surveys were conducted several weeks after the 2012 event, right after a major storm hit the region. Thus, making the differentiation between tsunami and storm effects difficult, especially for exposed sites. The six models from the literature also presented lower values at the sites exposed to storms, with Lay et al. (2013) model having the highest inundation profiles (see Appendix A).

Table 3.10 Run-up values for nine stochastic sources along the Haida Gwaii region

Sites	Model 82	Model 120	Model 128	Model 168	Model 185	Model 300	Model 685	Model 828
Otard Bay	0.98	0.82	0.89	0.97	0.96	0.95	0.97	0.88
Seal Inlet	0.39	0.31	0.32	0.34	0.42	0.40	0.48	0.27
Gudal Bay	0.95	0.64	0.96	0.87	1.12	1.09	1.17	0.65
Saunders Island	0.76	0.66	0.66	0.82	0.77	0.56	0.77	0.46
Davidson Inlet	3.25	2.10	2.60	2.53	1.78	1.96	1.78	1.97
Sunday Inlet	4.06	2.77	3.21	3.02	3.13	2.88	3.13	2.98
Kwoon Cove	4.38	3.30	3.83	3.69	3.10	2.98	3.10	3.69
Pocket Inlet	4.56	3.24	3.91	3.84	3.23	3.05	3.23	3.83
Mike Inlet	4.71	3.12	3.40	3.98	3.69	3.58	3.69	4.26
Puffin Cove	3.92	3.35	2.78	3.41	3.22	3.74	3.22	3.77
Goski Bay	1.72	1.80	1.46	1.50	1.47	2.03	1.47	1.87
Staki Bay	2.06	0.76	1.09	1.24	1.24	1.56	1.24	1.38
Louscoone Inlet	0.99	0.46	0.55	0.58	0.73	0.73	0.73	0.53
Ta'dasl	2.00	1.26	0.54	1.50	1.51	1.52	1.51	0.88
Gilbert Bay	2.00	1.26	0.54	1.50	1.51	1.52	1.51	0.88

At sites sheltered from storm waves, the simulation results present closer run-up heights to those of the observations, with differences between 1 m and 3 m. Out of the eight models used for calculating run-up, Model 82 (Figure 3.14a) yields the best results and has the smallest differences between the observed and simulated run-up. The spatial variability of the maximum tsunami inundation height along the coastal line in the Haida Gwaii region is shown in Figure 3.24 for Model 82. It is observed that the inundation heights are governed by slip concentration in the asperity areas by comparing the inundation heights and wave amplitudes. Thus, models with higher slip values generated higher inundation and wave profiles. It is also important to note that some range of error in the DEM data can also affect the tsunami simulations, especially close to the coast.

3.10 Conclusions

The stochastic tsunami simulations for Mw 7.7-7.8 scenario were calculated for the Haida Gwaii region. The uncertainties were considered for the source geometry and slip distributions during the stochastic source models synthesis. The variability of source parameters and fault geometries for the region based on global scaling relationships highlighted the sensitivity of the tsunami waves and tsunami inundation to the areas with a high slip concentration. Therefore, the more concentration of slip in the areas of interest will result in higher amplitudes. Moreover, the usage of multiple observations to constrain such parameters validates the results.

Furthermore, a set of models that match the observations can better represent the uncertainty of the events and help better understand the tsunami hazard of the region. The inclusion of uncertainty and variability and the usage of multiple observations are important improvements to the approaches used by previous studies. This is further shown by lower squared errors (i.e. 0.511 and 0.753 of Model 168 and Model 128 respectively; Table 3.9) than the previous source models of the region (i.e. lowest of 0.902 from Gusman et al. model; Table 3.9). Thus, the comparison against the Gusman et al. (2016) model and the Monte Carlo tsunami simulations shows that the stochastic source models can produce realistic tsunami results similar to those of the 2012 Haida Gwaii tsunami. However, the run-up values for the stochastic source models were lower than those reported by the post-tsunami field surveys. This discrepancy between run-up values could be the result of severe storms overprinting the tsunami observations. This overprinting can be shown by the larger differences between the simulated run-up and the run-up on sites exposed to storm waves and lower differences at sheltered sites. Nevertheless, the stochastic method and Monte Carlo tsunami simulations can provide important information about possible tsunami outcomes for the Haida Gwaii region, thus quantifying uncertainties in the prediction of tsunami hazards.

Chapter 4

4 Future Tsunami Scenarios for the Haida Gwaii Region

Historically, the Haida Gwaii region experienced Mw 8 (i.e. 1949 earthquake) strike-slip earthquakes on the north side of the fault, while an Mw 7.8 (i.e. 2012 earthquake) thrust earthquake occurred on the southern part of the fault. Although the 1949 earthquake was a pure strike-slip event, it generated a small tsunami. The lack of tsunami observations might be due to the fault’s strike-slip mechanism or the lack of settlements and observation stations along the coast of Haida Gwaii (Cassidy et al., 2014). Apart from those events, another event (i.e. 2001 Mw 6.1 earthquake) caused a tsunami in the region. The 2001 earthquake generated a larger than expected tsunami. The larger tsunami waves might have resulted from the 30 km length of the effective seismic source, which is larger than the 15 km length from the actual seismic source expected for the magnitude and the aftershock sequences (Rabinovich et al., 2008). An explanation for this more extensive effective seismic source is that the rupture extended into the soft sediments of the Queen Charlotte Terrace (QCT), amplifying the displacement of the earthquake (Rabinovich et al., 2008). The QCT is an irregular terrace extending from the south end of the Haida Gwaii islands to their north end and has a depth of 1000m (Hyndman, 2015; Figure 4.1). Furthermore, the QCT runs parallel to the margin between the Pacific-North American Plates. As it moves northwest along the margin, the convergence component decreases as it reaches the eastward part of the Queen Charlotte Fault (QCF) on the western side of Graham Island. Thus, on the southwestern side, the underthrusting and convergence follow pre-existing fractures and thrusts at the base of the terrace.

The 2012 earthquake only ruptured half of the available fault area (Allen et al., 2015). Moreover, Kao et al. (2015) suggested that most of the elastic strain along the QCF was not released during the 2012 earthquake. This is suggested based on the 2012 Haida Gwaii earthquake’s aftershocks distribution extending no further than the seismic gap, and none were larger than Mw 4.8. Additionally, there is a possibility of the slip extending toward the northern part of the fault, given the locations of the relocated aftershock distributions, which show that the 2012 source region correlates with the southern part of the 1949 event.

Therefore, this information supports the likelihood of a major strike-slip earthquake on the northern part of the region that can extend to the southern part and release the thrust component of the QCF in the future, causing a larger tsunamigenic event than the 2012 Mw 7.8 earthquake. Consequently, the 2012 Haida Gwaii event provides important information about the region's seismicity, which allows studying possible future events and creating proper risk mitigation strategies for the region.

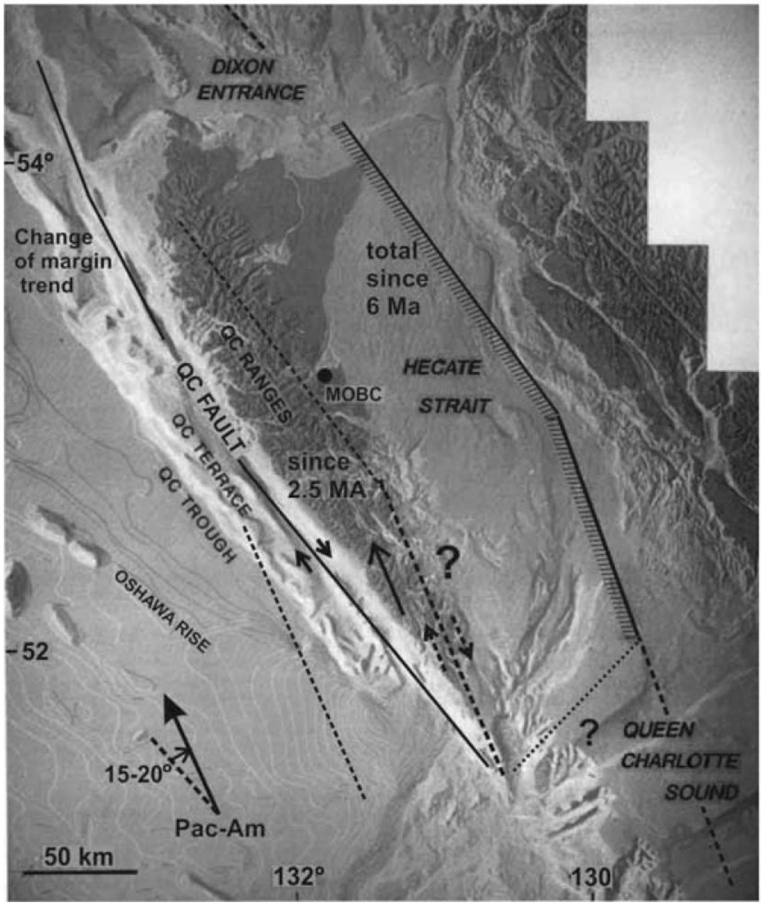

Figure 4.1 The Oshawa rise, Queen Charlotte Trough (trench), Queen Charlotte terrace (accretionary sedimentary prism), and Queen Charlotte ranges (uplifted edge of continent). The dashed lines show the model extent of the underthrust plate for 2.5 and 6 million years, that is, for the triple junction at Brooks Peninsula (from 6 Ma) and at the Wilson Knolls (from 2.5 Ma). It is assumed that there has been no significant crustal shortening in these estimates. (Hyndman, 2015)

The chapter is organized as follows. First, the methodology for the stochastic source modelling and the Monte Carlo tsunami simulation for future larger events is explained. The present scenario considers events with Mw ranging from 7.9 to 8.1. Furthermore, a broader asperity zone is considered to produce larger magnitudes. Historical events, such as the M8.1 event, motivate applying the stochastic method (if slip extends toward the northern part of the fault) and Monte Carlo tsunami simulation to a slightly larger event and without strict constraints based on the observations from 2012. Finally, the results of the tsunami analysis of future larger events are explained in detail for offshore and onshore observations.

4.1 Procedure

Following the same methodology from Chapter 3, the earthquake scenario is first defined by specifying the target Mw, fault model, and asperity zone (Figure 4.2). An Mw range of 7.9 to 8.1 is considered based on the existence of the QCT and oblique movement of the fault, which can release the thrust component in the region, thus, rupturing both the strike-slip mechanism on the north and thrust mechanism on the south of the fault. Then, the synthetic fault model is developed based on the geometry of the fault plane (strike and dip).

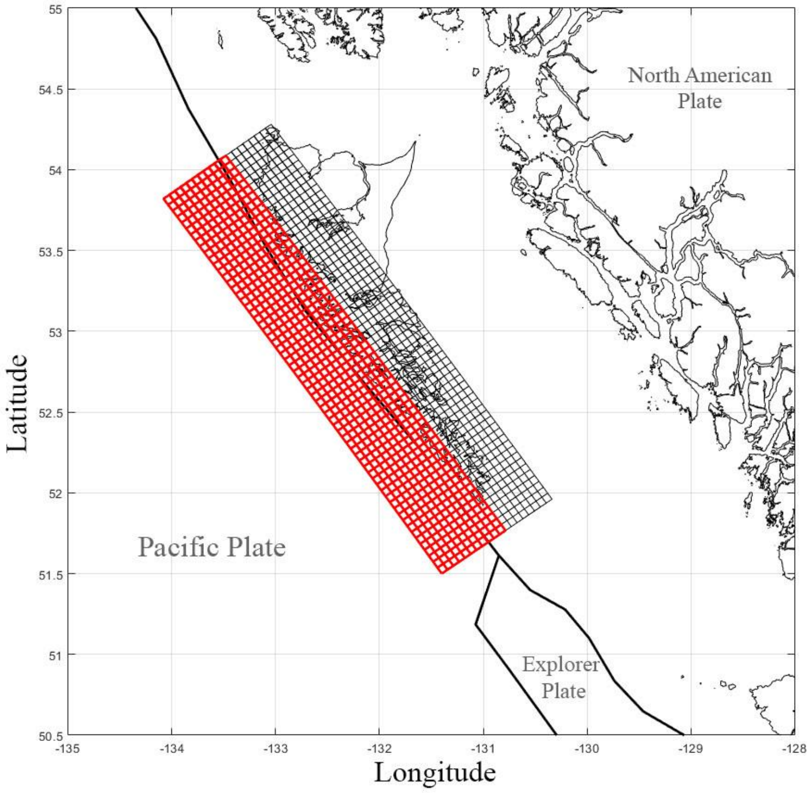

Figure 4.2 Map showing the synthetic fault plane (black) and the asperity zone (red) defined for this study

The fault model from Chapter 3 (Figure 3.8) is also used for this case since it covers the entire length of the QCF. The width is based on the QCT (Hyndman, 2015); however, it is larger to allow different geometry during the stochastic synthesis. The synthetic fault covers an area spanning 315 km along strike and 95 km along dip, with a constant strike of 325° and dip angle of 20°. The asperity region is a sub-region within the fault that has a significant amount of earthquake slip. In this scenario, an asperity zone different from that of the 2012 Haida Gwaii earthquake is considered. The asperity is larger than that of the 2012 event and is based on the extension of the QCT (Hyndman, 2015) and the thermal constraints of the fault (Wang et al., 2015; Figure 4.2). The present scenario's parameters reflect the hypothesis that all parts of the QCT can simultaneously rupture.

Secondly, earthquake source parameters (width W, length L, slip average Da, slip maximum Dm, Box-Cox parameter λ, correlation length along strike Ax, correlation length along dip Az, and Hurst number H) are calculated using scaling relationships by Goda et al. (2016; Equations 3.4-3.9). The uncertainty and the correlation associated with regression models should be taken into account in sampling the values of the source parameters. Thus, the sampling regression prediction errors of the scaling relationships avoid unrealistic combinations of source parameters and are sampled from the multivariate normal distribution function in a logarithmic space (Table 3.7).

Third, a Fourier integral method generates a random slip field based on the generated slip distribution parameters (Pardo-Iguzquiza & Chica-Olmo, 1993). Then, the synthesized slip distribution is converted via Box-Cox transformation to achieve a slip distribution with realistic positive skewness (Goda et al., 2014). The resulting slip distribution is then adjusted to the target Da and Dm to avoid undesirable slip values. Subsequently, the location of the fault plane is determined randomly within the synthetic fault plane, and the simulated values are constrained by comparing the target and simulated moment magnitude ($M_o = \mu W L D_a$, where μ is the rock rigidity and is set to 40 GPa; Gusman et al., 2016). Only models that fit the set criteria are accepted; thus, the steps are repeated until a model that falls within the criteria is generated. Finally, further constraints are applied to ensure a realistic synthesized slip distribution (Table 4.1). The first one is that the ratio between the average fault area and the fault area (Sa/S) falls within a range of 0.194 to 0.286. The second constraint is that the ratios between the correlation lengths (Az or Ax) and the geometry parameters (W, or L) are in the ranges of 35 % to 50% and 20% to 60%, respectively, based on the extension of the QCT, and thermal constraints (i.e. 1949 M. 8.1 earthquake). The final constraint is that 70 % to 100% of the simulated earthquake slip must concentrate on asperity regions.

Table 4.1 Summary of stochastic earthquake slip simulation parameters

Model Parameter	[Lowe, Upper]
Mw	[7.9 8.1]
Slip ratio	[0.7,1.0]
Ratio L/W	[0.5,6.0]
Az to W range	[0.35,0.5]
Ax to L range	[0.2,0.6]

Fourth, the Monte Carlo tsunami simulation is carried out. The initial water surface elevation is calculated using Okada (1985) and Tanioka & Satake (1996) (Section 2.3). The tsunami wave propagation is calculated by solving the non-linear shallow-water equations with run-up (Equations 2.17-2.19; Goto et al., 1997). A bathymetry 2020 dataset is obtained from the Geometry Bathymetric Chart of the Oceans (GEBCO) for deep to shallow water regions, while digital elevation models (DEM) are obtained for the onshore topography. The Canadian Digital Elevation Model (CDEM) is used for the Canadian coasts, whereas the Shuttle Radar Topography Mission (STRM) DEM is used for the American coasts. Moreover, the bottom friction is evaluated using Manning’s formula, and the fault rupture is assumed to occur instantaneously. Computational domains are used for the tsunami propagation simulations and follow a 1/3 ratio (i.e. 810 m, 270 m, 90 m, 30 m; see Section 3.8.2). The grid nesting from coarse to fine resolution is done so the large to small-scale tsunami waves can be considered based on changes in water depth. For the present scenario, the finer resolution used is 270m, which is coarse to evaluate the run-up in coastal areas. Therefore, an extensive inundation calculation is excluded in this study, and error range should be considered for the nearshore results. The vertical displacement of water due to earthquake rupture (Okada, 1985) and the horizontal effects of steep slopes on the vertical displacement of water (Tanioka &Satake, 1996) are computed at the 810-m resolution. Then, the numerical tsunami calculation is performed for 6 hours with an integration time step of 1 s to satisfy the Courant-Friedrichs-Lewis condition. Finally, the above procedure is repeated until sufficient source models are generated, and the tsunami simulations are evaluated.

4.2 Results

4.2.1 Simulated Stochastic Source Models

The magnitude range of Mw 7.9 to 8.1 was considered for the stochastic source models. A total of 326 stochastic source models were generated with a diverse set of source parameters and slip characteristics to account for uncertainties and variabilities. Overall, the models are consistent with global scaling relationships, as presented in Figure 4.3, and mostly fall within the prediction intervals (16th and 84th percentiles). However, some models had larger L and Az than earthquakes for similar magnitudes. These larger values are expected since the fault is rupturing entirely.

Figure 4.4 shows stochastic source examples and the variability of the fault's geometry and asperity regions. This highlights the ability of the stochastic source modelling method to generate variable source models for a given scenario. It can be observed that both the plane size and slip values increase with Mw, and the location and size of the asperity areas also change. These features have a significant influence on tsunami simulation results. They are controlled by the target slip, Mw, and stochastic synthesis parameters (Goda et al., 2016, Mori et al., 2017b, Momeni et al., 2020). Moreover, the hypocentre is likely to be located near the fault's shallow side and around subfaults with relatively large slip. Thus, the hypocentre is more likely to be in the asperity areas. In this case, since the asperity zone was set up to cover the entire length of the fault plane, the slip concertation varies more widely across models, which differs from the more constrained 2012 scenario. This variability allows accounting for different possibilities of slip concentration in future events. The overall Da is 1.67 m which falls within the ranges of the global scaling relationships. The overall Dm for all 326 slip distributions is 8.97 m and is similar to the scaling relationships. The overall Mw is 7.98 and represents possible larger events in the region. The average L is 241 km, whereas the average W is 82 km. The L of some models is larger than the global scaling relationships, whereas the W of other models is smaller than expected. For the present scenario, no slip distribution was constrained by deformation observations, as was done for the 2012 Haida Gwaii event. The present stochastic source models can then generate realistic earthquake scenarios and the effects of the corresponding tsunamis. Figure 4.4f shows the overall average slip model, generated by calculating the mean slip of subfaults of the 326 stochastic sources with the large slip areas concentrated to the shallow part of the fault plane. For this scenario, the best model is not chosen, but instead, the results and 2012 tsunami observations are compared.

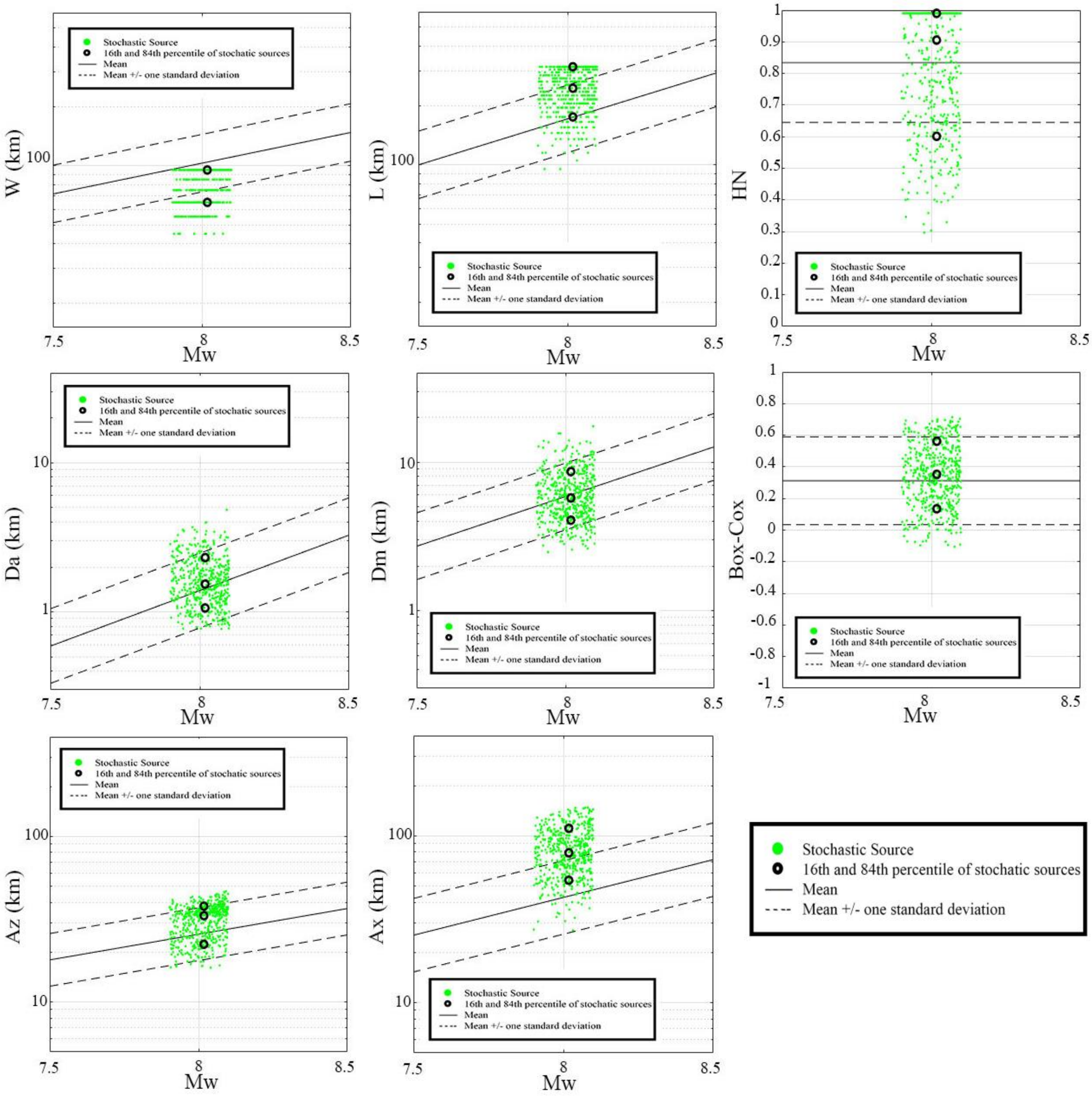

Figure 4.3 Comparison of 326 stochastic source parameters (green dots) with the corresponding scaling relationships.

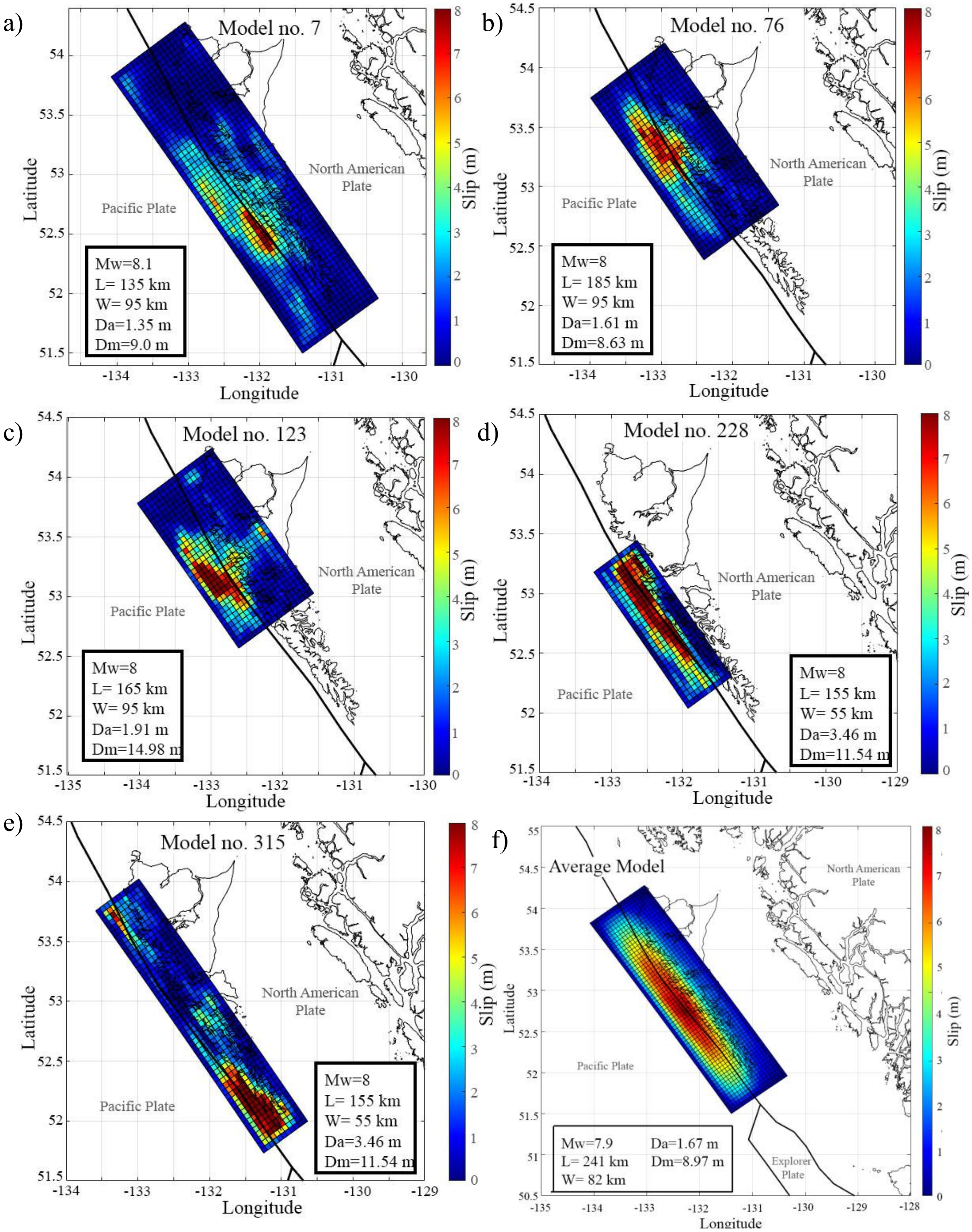

Figure 4.4 (a-e) Five stochastic models (Mw 7.9-8.1), and (f) overall average slip models based on the 326 stochastic sources

4.2.2 Far-Field Results

A total of 326 stochastic source models are used for the Monte Carlo tsunami simulations. The tsunami wave characteristics of the stochastic models are examined for the far-field locations. The tsunami waves amplitudes are simulated for the far-field results on tide gauges, DART stations, and ONC BPRs that recorded the 2012 tsunami. The amplitudes of the larger tsunami are compared against the observations of the 2012 event to evaluate the difference between tsunami wave amplitudes of the observations (Mw 7.8) and larger Mw events (Mw 7.9-8.1). In Figures 4.5 and 4.6, the individual tsunami wave profiles for different stations (i.e. Henslung Cove, Queen Charlotte, Winter Harbour, La Push, Port Orford, Crescent City, Barkley Slope, Clayoquot Canyon, Cascadia Basin, DART 46419, DART 46410, and DART 46411; see Figure 3.2 for locations) are shown in gray, the statistics are shown in black (mean, 10th, and 90th percentiles), while and the observations of the 2012 Haida Gwaii tsunami are shown as a thick black line (see Appendix B for tsunami wave profiles of all the stations).

Stations on the north (i.e. Henslung Cove, DART 46410, and Ketchikan), middle (Winter Harbour, Queen Charlotte, and Cascadia Basin, Barkley Slope, Clayoquot Canyon, and DART 46419), and south (i.e. La Push, Port Orford, Crescent City, and DART 46411) are chosen to demonstrate the variability of tsunami wave amplitude based on the proximity to the asperity regions and to show the effects of regional slip patterns on tsunami profiles. As expected, the results show that the wave amplitudes are larger than those observed during the 2012 Haida Gwaii tsunami. The tsunami profiles at these different locations are variable. The average of the wave profiles is close to the observations of the 2012 events and does not vary significantly. However, some tsunami waves are several times greater than the average tsunami amplitudes and observations and exceed the 90th percentile. Stations like Cascadia Basin and DART 46411 (Figure 4.6) have wave amplitudes almost twice as large as the 90th percentile. There is more variability in both tsunami amplitudes and time arrivals depending on the location of the asperity areas since the asperity zone for this scenario extended along the entire fault’s length. Deep-ocean observations present higher values than those recorded for the smaller 2012 event. For stations like Cascadia

Basin, DART 46410, and DART 46411, the tsunami waves have amplitudes that are three times as large as the observations.

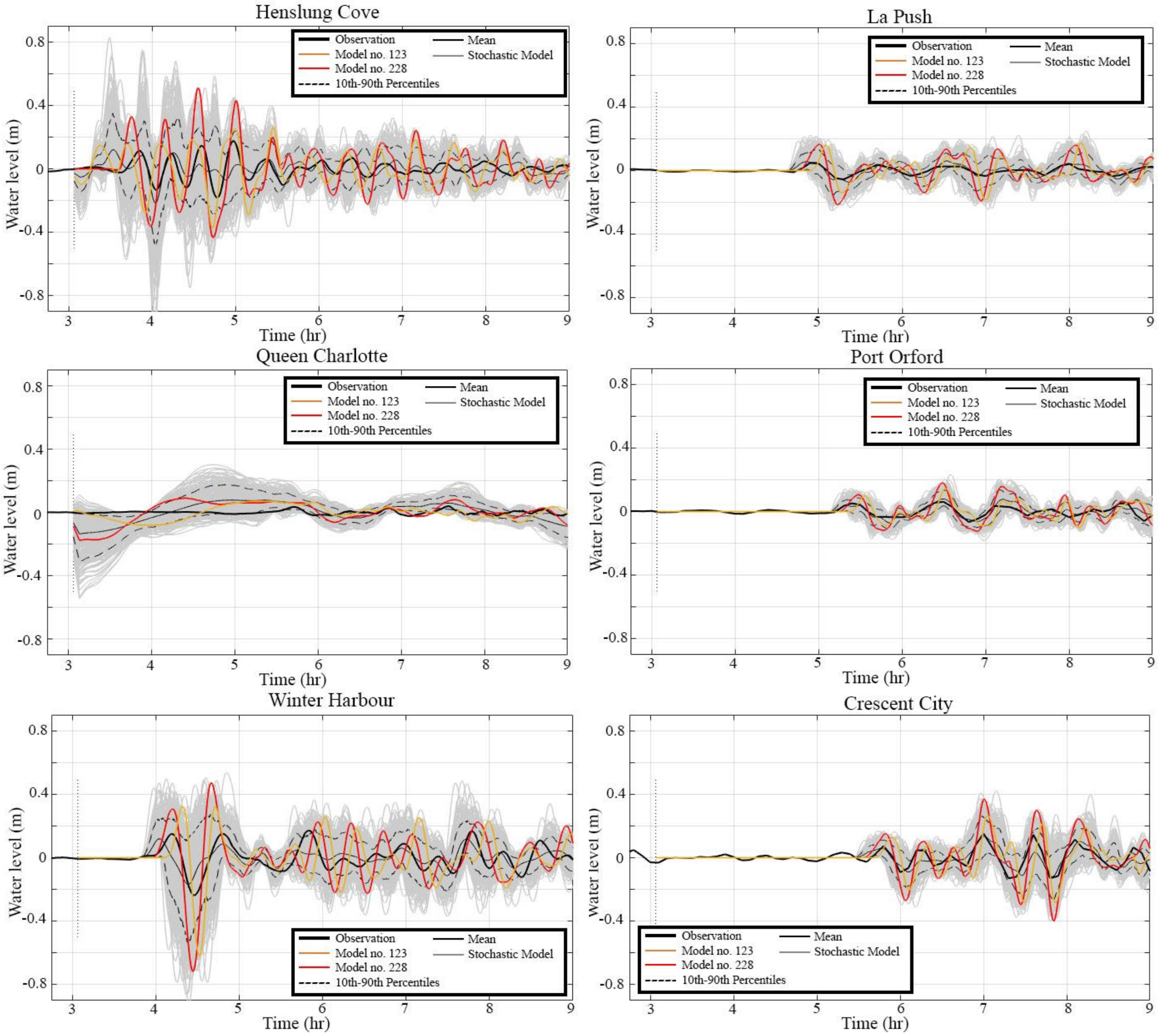

Figure 4.5 Comparison of time histories of tsunami wave for the 326 stochastic models (mean, 90th, and 10th percentile) and observations

Tsunami wave profiles are affected by proximity to the asperity areas. Stations closer to the rupture zone have the highest amplitudes, like Queen Charlotte, Winter Harbour and Henslung Cove (Figure 4.4). Some simulations start with a trough at northern stations like Henslung Cove and Ketchikan (see Appendix B). The reason might be that the extension of the fault rupture lengths extended too far north. Slip distributions like Model 228 (Figure 4.4d) do not present this trough at the Ketchikan station, whereas for the Henslung Cove station, it only presents a slight trough. Models, such as Model 123 (Figure 4.4c), presented both troughs at such stations. Therefore, the results can help limit the extent of the fault length on the northern part.

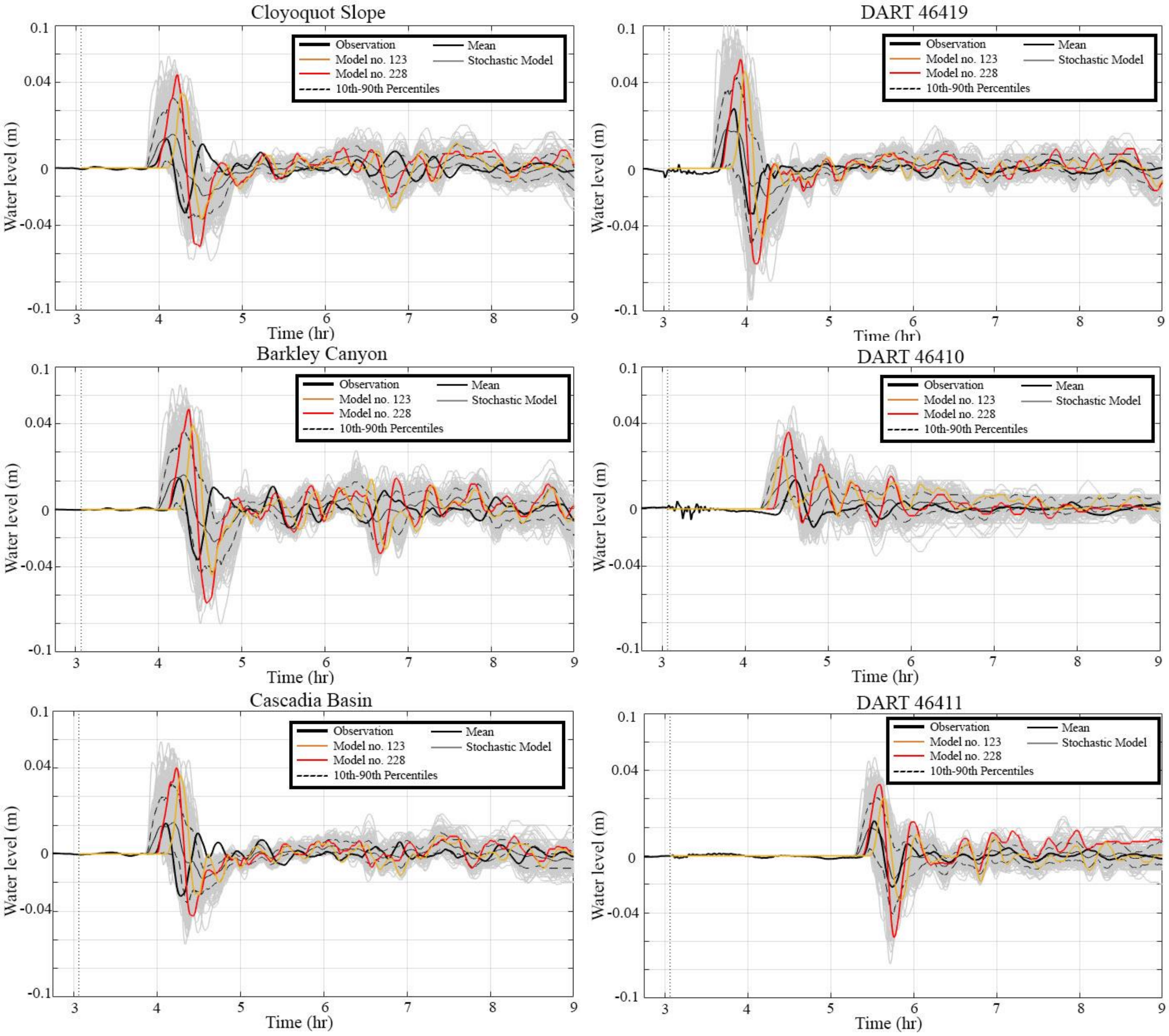

Figure 4.6 Comparison of time histories of tsunami wave for the 326 stochastic models (mean, 90th, and 10th percentile) and observations

The Queen Charlotte station (Figure 4.5) presents a trough at the beginning of the tsunami waveforms, just like stations Henslung Cove and Ketchikan. However, for the station, the slip distributions of some stochastic models extend too far beneath the islands. For example, although the length of Model 123 (Figure 4.4c) does not extend to the south, the width covers most of the island, and some subfaults with significant slip are beneath the islands.

Thus, at the Queen Charlotte station, the first wave is a trough. The same can be said for model 228 (Figure 4.4d) since it also has a slip concentration beneath the islands. Therefore, the results can help limit the extent of the fault width underneath the islands.

The tsunami wave profiles also provide information on the arrival times of the first wave and maximum waves. The arrival times of the first tsunami wave are different from those observed in the 2012 event. For larger events, the arrival times of the first wave can be earlier than those of the 2012 observations. For instance, the simulated first waves at Cascadia Basin arrive 10 minutes earlier than the observations, while at the Queen Charlotte station, the difference can be as long as 3 hours. For all other stations, the differences are approximately 20 minutes. Arrival times of the maximum amplitude waves range from 10 minutes (i.e. Cascadia Basin) to 2 hours (i.e. Crescent City) after the first wave. The differences in arrival times are caused by the proximity to the asperities (which are variable for this scenario) and region’s topography. These differences in arrival times are important to note in the zone’s evacuation strategies of populated areas. Hence, stochastic simulations can convey the prediction uncertainties when planning risk mitigation strategies.

4.2.3 Near field Results

The sensitivity of the tsunami wave amplitudes to the location and amount of slip can be further observed in Figure 4.7, in which the maximum wave heights for the Haida Gwaii region are shown. Comparison of the maximum wave heights suggests that the local features of the slip distributions for each of the models (Figure 4.3) and the near-shore bathymetry significantly influence the tsunami waves along the shoreline. Figure 4.7 shows that the amplification of tsunami heights along the western side of the Haida Gwaii region due to shallow water is significant inside bays and inlets (See Appendix B for Model no. 315). Tsunami wave heights differ depending on the location of the asperity zone of each of the models. Therefore, the maximum tsunami heights and run-ups are expected within that region. If the asperity regions are located near the locations of interest, larger tsunami wave amplitudes and inundations are expected. The results show the variability of the inundation height depending on the source models. The tsunami heights are influenced by the source, tsunami path and topography. Hence, the tsunami wave heights are spatially variable.

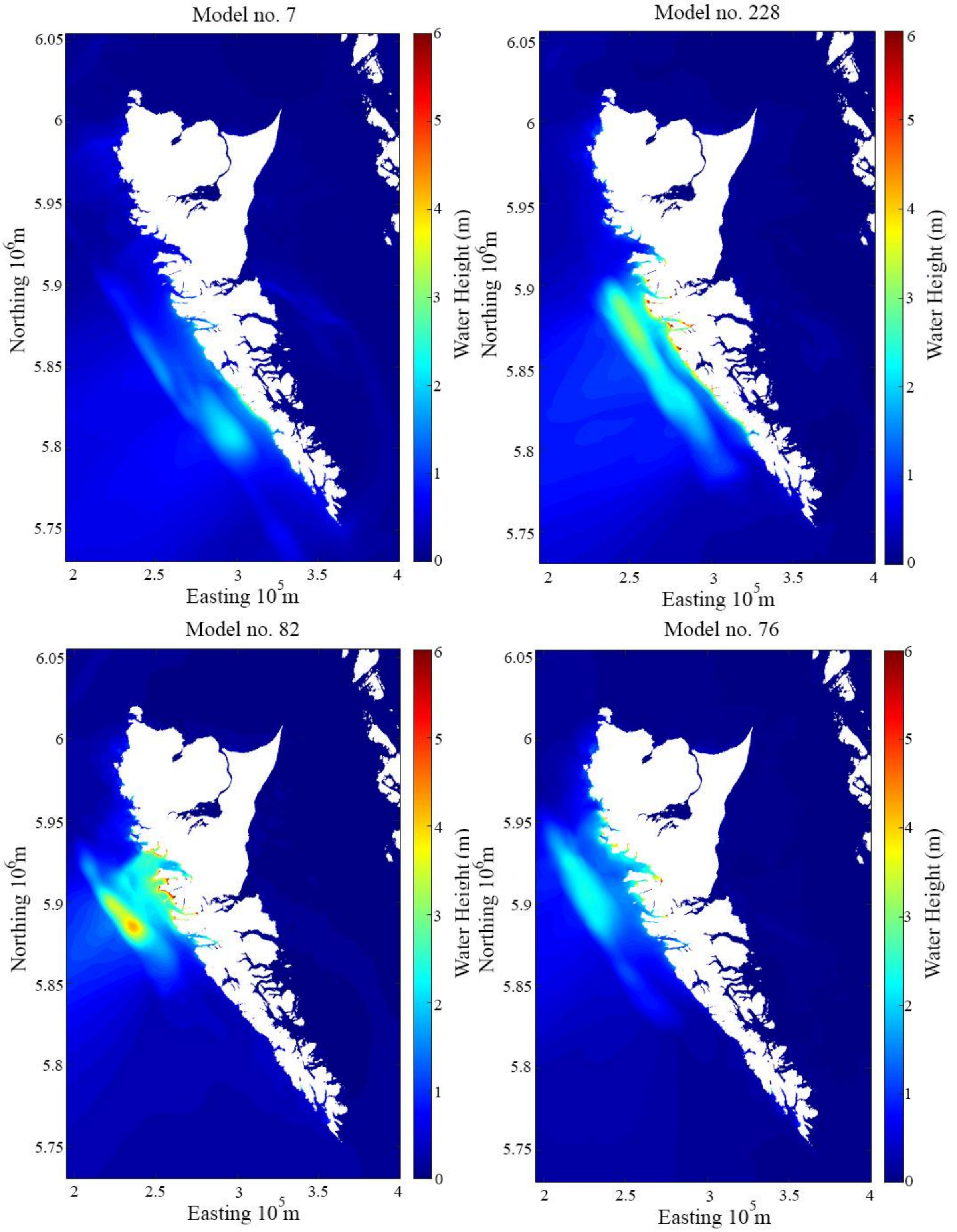

Figure 4.7 Maximum wave height for the Haida Gwaii region

4.3 Conclusions

Stochastic earthquake source models in Monte Carlo tsunami simulations are useful in including the uncertainties of tsunami simulations and show the variability and sensitivity of tsunami wave amplitudes depending on slip values and asperity regions. The stochastic source models for possible Mw 8 earthquakes in the Haida Gwaii region took into account uncertainties of the location and source parameters of the fault. This is shown in the variability of the slip distributions of the source parameters used in Monte Carlo tsunami simulations and the maximum wave heights and the time series at different stations. The results highlighted the method's usefulness to explore different possible tsunami amplitudes and inundations for a given scenario, which can help predict possible tsunami hazards to coastal communities and make informed decisions in risk mitigation strategies. The tsunami analysis of future larger events is challenging because of the uncertainties in how the next scenario will happen and the various assumptions made. For the given scenario, various improvements can be made, like finer computational domains to assess better the inundation of coastal areas, and the tsunami simulation of more stochastic source models. The following points can further improve some of the limitations of the present study:

1. The use of higher-resolution bathymetry and DEM datasets to reduce errors in the tsunami simulation.
2. The use of geological evidence of past events in the region to better predicts the fault's mechanism.

Finally, the results of the tsunami simulations can be used in future work to constrain possible parameters like the possible slip concentration and validate the models based on the inundation of areas of interest for larger events in the zone, like the ones from the Cascadia Subduction Zone.

Chapter 5

5 Conclusions

The thesis objectives were to develop stochastic slip models for Haida Gwaii earthquakes and analyze the tsunami hazard along the western North Pacific coastline due to such events in terms of tsunami wave profiles at observation stations and maximum tsunami wave heights along the Haida Gwaii using Monte Carlo tsunami simulations. An extensive tsunami simulation was performed by developing many stochastic source models for both the 2012 Haida Gwaii event (i.e. 128 stochastic source models) and future larger events (i.e. 326 stochastic source models) with magnitude ranges of 7.7-7.9 and 7.9-8.1, for each earthquake scenario, respectively.

For the 2012 Haida Gwaii scenario, the earthquake source regions from six inversion models from the literature were first evaluated and compared against global scaling relationships (Goda et al., 2016). Then a synthetic fault model was defined for stochastic source synthesis. The same synthetic fault plane was used for both Mw scenarios. The asperity zone was then defined. For the 2012 scenario, the asperity zone was based on the region's aftershock sequence and thermal constraints. In contrast, the asperity zone for larger events was based on the extension of Queen Charlotte Terrance, significant slip areas from the 1949 Mw 8.1 earthquake, and the oblique seismic movement that might release the fault's thrust component. Deformation observations were used as a constraint during the synthesis of the stochastic sources for the 2012 scenario, while no such constraint was used for the larger future events. Uncertainty and variability of earthquake source parameters were accounted for when producing the stochastic source models.

Both tsunami simulation results were compared against the 2012 observations recorded on Canadian and American tide gauges, Ocean Network Canada bottom pressure sensors, and DART buoys. Furthermore, the simulated tsunami wave profiles from the 2012 scenario were compared against the Gusman et al. (2016) model to test the performance of the simulations. The tsunami wave amplitudes were further evaluated using the tsunami wave profiles at 20 sites at 30 m depth along the coastline. The maximum tsunami wave height at 217 sites at 10 m depth. Moreover, the run-up was calculated for the best eight models and compared to the run-up reported by field surveys (Leonard and Bednarski, 2014). The tsunami wave profiles produced from the stochastic source models for the 2012 scenario are in good agreement with those of the 2012 Haida Gwaii event and are comparable to those of the Gusman et al. (2016) model. The results from the future events show larger amplitudes than those of the 2012 events and earlier arrival times of the first wave. The evaluation of tsunami run-up was not possible for the larger events since the grid system used during tsunami simulations was too coarse.

The results show that the stochastic method can help constrain the source characteristics of a given event and how different geometries and parameters can produce similar results. Furthermore, the method helps to have a broader picture of the possible future scenarios and provides important information that can be used for risk mitigation planning as it helps constrain parameters that can be used for forecasting future events.

5.1 Limitations

The results show the importance of incorporating uncertainty when modelling earthquake source models since the location and amount of slip greatly affects the tsunami heights and concentration. Furthermore, the stochastic method allows constraining the source parameters for possible future events useful in tsunami forecasting and risk mitigation planning. However, it is important to note the limitations of the present study. One limitation is the distance range to simulate tsunami propagation. The present method and computational code used can only estimate tsunami propagation to relatively close distances (couple of thousand kilometres) from the source, since larger distances would need the use of spherical coordinates and take into account the curvature of the Earth’s surface.

Another limitation depending on the type of analysis, is that the method is computationally demanding. This limitation is notable in the present study since many simulations for both earthquake scenarios (offshore and onshore) would have been preferred. Moreover, a more accurate Digital Elevation Model (DEM) is needed to reduce the run-up simulation errors further because the simulations need to take into account the topography of the ocean bottom.

5.2 Future Work

In future studies, tsunami simulations for the finer grid system (i.e. 30m) should be run more extensively to further analyze the run-up extension in the Haida Gwaii region. In addition, more simulations for offshore and nearshore locations are needed to constrain better source parameters. This is especially true for future events since the coarse grid used in the present simulations is too large to calculate run-up locations.

Furthermore, an extensive sensitivity analysis needs to be carried out for the source region parameters by changing some parameters and evaluating the effects of the changes in the tsunami simulations. The occurrence probability might also be included to extend this work to a complete probabilistic tsunami hazard analysis. A more detailed study can be done with more simulations for Haida Gwaii events for special areas of interest like cities of towns, based on proximity to areas with likely slip clustering. Furthermore, Cascadia Subduction Zone simulations events can use the inundation patterns of the larger events' results to constraint the possible parameters for future subduction events.

References

AECOM. (2013). Modeling of potential tsunami inundation limits and run-up. report for the capital region district. (Project Number: 60242933).

Allen, T.I., Adams, J., Halchuk, S., & Rogers, G.C. (2015). 5th Generation Seismic Hazard Model for North-Western Canada. *The 11th Canadian Conference on Earthquake Engineering.* (Paper Number: 937982)

An, C., Liu, H., Ren Zhiyuan, Y., & Yuan. (2018). Prediction of tsunami waves by uniform slip models. *Journal of Geophysical Research: Oceans*,123, 8366–8382. https://doi.org/10.1029/2018JC014363

Atwater, B.F., Musumi-Rokkaku, S., Satake, K., Tsuji, Y., Ueda, K., & Yamaguchi, D.K. (2015), The orphan tsunami of 1700—Japanese clues to a parent earthquake in North America, 2nd ed.: Seattle, University of Washington Press, U.S. *Geological Survey Professional Paper* 1707, 135 p

Barth, S., Geertsema, M., Bevington, A. R., Bird, A. L., Clague, J. J., Millard, T., Bobrowsky, P. T., Hasler, A., & Liu, H. (2020). Landslide response to the 27 October 2012 earthquake (MW 7.8), southern Haida Gwaii, British Columbia, *Canada. Landslides*, 17(3), 517–526. https://doi.org/10.1007/s10346-019-01292-7

Bernard, E., & Titov, V. (2015). Evolution of tsunami warning systems and products. Philosophical Transactions of the Royal Society A: Mathematical, *Physical and Engineering Sciences*, 373, 20140371. https://doi.org/10.1098/rsta.2014.0371

Bird, A. L., & Lamontagne, M. (2015). Impacts of the October 2012 magnitude 7.8 earthquake near Haida Gwaii, Canada. *Bulletin of the Seismological Society of America*, 105, 1178–1192. https://doi.org/10.1785/0120140167

Blaser, L., Krüger, F., Ohrnberger, M., & Scherbaum, F. (2010). Scaling relations of earthquake source parameter estimates with special focus on subduction environment. *Bulletin of the Seismological Society of America*, 100, 2914–2926. https ://doi.org/10.1785/0120100111

Brothers, D. S., Miller, N. C., Barrie, J. V., Haeussler, P. J., Greene, H. G., Andrews, O., BrianD., Zielke, Watt, J., & Dartnell, P. (2020). Plate boundary localization, slip-rates and rupture segmentation of the queen charlotte fault based on submarine tectonic geomorphology. *Earth and Planetary Science Letters*. 530, 115882. https://doi.org/10.1016/j.epsl.2019.115882

Cassidy, J. F., Rogers, G. C., & Hyndman, R. D. (2014). An overview of the 28 October 2012mw 7.7 earthquake in Haida Gwaii, Canada: A tsunamigenic thrust event along a predominantly strike-slip margin. *Pure and Applied Geophysics*. 171(12), 3457–3465. https://doi.org/10.1007/s00024-014-0775-1

Causse, M., Dalguer, L. A., & Mai, P. M. (2014) Variability of dynamic source parameters inferred from kinematic models of past earthquakes, *Geophysical Journal International*, 196 (3). 1754–1769, https://doi.org/10.1093/gji/ggt478

Dao, M. H., & Tkalich, P. (2007). Tsunami propagation modelling - a sensitivity study. *Natural Hazards and Earth System Sciences*. 7. https://doi.org/10.5194/nhess-7-741-2007

Davies, G., Horspool, N., & Miller, V. (2015), Tsunami inundation from heterogeneous earthquake slip distributions: Evaluation of synthetic source models, *Journal of Geophysical Research. Solid Earth*. 120, 6431– 6451, https://doi.org/10.1002/2015JB012272

Davies, G., (2019) Tsunami variability from uncalibrated stochastic earthquake models: tests against deep ocean observations 2006–2016, *Geophysical Journal International*, 218 (3), 1939–1960. https://doi.org/10.1093/gji/ggz260

Fine, I. V., Cherniawsky, J. Y., Thomson, R. E., Rabinovich, A. B., & Krassovski, M. V. (2015). Observations and numerical modeling of the 2012 Haida Gwaii tsunami off the coast of British Columbia. *Pure and Applied Geophysics*, 172(3), 699–718. https://doi.org/10.1007/s00024-014-1012-7

Fine, I. V., Thomson, R. E., Lupton, L. M., & Mudschutz, S. (2018). Numerical modelling of a Cascadia subduction zone tsunami at the Canadian coast guard base in seal cove, prince Rupert, British Columbia. *Hydrography and Ocean Sciences*, 322, 34.

Frankel, A., Chen, R., Petersen, M., Moschetti, M., & Sherrod B. (2019). 2014 update of the Pacific Northwest portion of the U.S National Seismic Hazard Maps. *Earthquake Spectra,* 31 (S1), S131-S148. https://doi.org/10.1193/111314EQS193M

Geist, E. L. (2002). Complex earthquake rupture and local tsunamis, *Journal of Geophysical Research: Solid Earth*, 107(B5), ESE 2-1-ESE 2-15. https://doi.org/10.1029/2000JB000139

Geist, E. L. (2005). Local tsunami hazards in the pacific northwest from Cascadia subduction zone earthquakes. *U.S Geological Survey, Professional Paper*, (1661-B). https ://doi.org/10.3133/pp1661B

Geist, E. L., & Dmowska, R. (1999). Local tsunamis and distributed slip at the source. *Pure and Applied Geophysics*,154, 485–512. https://doi.org/10.1007/s000240050241

Geist E.L. & Oglesby D.D. (2014) Tsunamis: Stochastic Models of Occurrence and Generation Mechanisms. In: Meyers R. (eds) Encyclopedia of Complexity and Systems Science. Springer, New York, NY. https://doi.org/10.1007/978-3-642-27737-5_595-1

Ghobarah, A., Saatcioglu, M., & Nistor, I. (2006). The impact of the 26 December 2004 earthquake and tsunami on structures and infrastructure. *Engineering Structures*, 28, 312–326. https://doi.org/10.1016/j.engstruct.2005.09.028

Gisler, G. R. (2008). Tsunami simulations, *Annual Review of Fluid Mechanics*.40 (1), 71-90. https://doi.org/10.1146/annurev.fluid.40.111406.102208

Goda, K., Mai, P. M., Yasuda, T., & Mori, N. (2014). Sensitivity of tsunami wave profiles and inundation simulations to earthquake slip and fault geometry for the 2011

Tohoku earthquake. *Earth, Planets and Space*, 66, 105. https://doi.org/10.1186/1880-5981-66-105

Goda, K., & Song, J. (2016). Uncertainty modeling and visualization for tsunami hazard and risk mapping: A case study for the 2011 Tohoku earthquake. Stochastic *Environmental Research and Risk Assessment*, 30(8), 2271–2285. https://doi.org/10.1007/s00477 -015-1146-x

Goda, K., Petrone, C., De Risi, R., & Rossetto, T., (2017a). Stochastic coupled simulation of strong motion and tsunami for the 2011 Tohoku, Japan earthquake. *Stochastic Environmental Research Risk Assessment,* 31, 2337–2355. https://doi.org/10.1007/s00477-016-1352-1

Goda, K., Yasuda, T., Mai, P. M., Maruyama, T. & Mori, N. (2017b). Tsunami simulations of mega-thrust earthquakes in the Nankai-Tonankai Trough (Japan) based on stochastic rupture scenarios. *Geological Society, London, Special Publications*. 456, 55-74. https://doi.org/10.1144/SP456.1

Goda, K., Yasuda, T., Mori, N., & Mai, P. M. (2015), Variability of tsunami inundation footprints considering stochastic scenarios based on a single rupture model: Application to the 2011 Tohoku earthquake, *Journal of Geophysical Research. Oceans*, 120, 4552– 4575, doi:10.1002/2014JC010626.

Goda, K., Yasuda, T., Mori, N., & Maruyama, T. (2016). New scaling relationships of earth-quake source parameters for stochastic tsunami simulation. Coastal *Engineering Journal,* 58(3), 1650010–1–1650010–40. https://doi.org/10.1142/S0578563416500108

Goto C., Ogawa Y., Shuto, N., & Imamura, F. (1997). Numerical Method of Tsunami Simulation with the Leap-Frog Scheme. *IOC Manuals and Guides*, 35. UNESCO, Paris, France

Griffin, J. D., Pranantyo, I. R., Kongko, W., Haunan, A., Robiana, R., Miller, V., Davies, G., Horspool, N., Maemunah, I., Widjaja, W. B., Natawidjaja, D. H., & Latief, H.

(2017). Assessing tsunami hazard using heterogeneous slip models in the Mentawai islands, Indonesia. *Geological Society, London, Special Publications*, 441(1), 47–70. https ://doi.org/10.1144/SP441.3

Grilli, S.T., Harris, J.C., Tajalli Bakhsh, T.S. Masterlak, T. L., Kyriakopoulos, C., Kirby, J.T., & Shi, F. (2013). Numerical Simulation of the 2011 Tohoku Tsunami Based on a New Transient FEM Co-seismic Source: Comparison to Far- and Near-Field Observations. *Pure and Applied Geophysics.* 170, 1333–1359. https://doi.org/10.1007/s00024-012-0528-y

Gusman, A. R., Sheehan, A. F., Satake, K., Heidarzadeh, M., Mulia, I. E., & Maeda, T. (2016). Tsunami data assimilation of Cascadia seafloor pressure gauge records from the 2012haida Gwaii earthquake: Dense array for tsunami warning. *Geophysical Research Letters*, 43(9), 4189–4196. https://doi.org/10.1002/2016GL068368

Haeussler, P. J., Witter, R. C., & Wang, K. (2015). Intertidal biological indicators of coseismic subsidence during the mw 7.8 Haida Gwaii, Canada, earthquake. *Bulletin of the Seismological Society of America*, 105(2), 1265–1279. https://doi.org/10.1785/0120140197

Hayes, G. (2013). Updated finite fault results for the oct 28, 2012 mw 7.8 141 km s of Masset, Canada earthquake (version2). http://comcat.cr.usgs.gov/earthquakes/eventpage/pde2012102803040882014#scientificfinite-fault

Hayes, G. P. (2017). The finite, kinematic rupture properties of great-sized earthquakes since1990. *Earth and Planetary Science Letters*, 468, 94–100. https://doi.org/10.1016/j.epsl.2017.04.003

Heidarzadeh, M., Pirooz, M. D., & Zaker, N. H. (2009). Modeling the near-field effects of the worst-case tsunami in the Makran subduction zone. *Ocean Engineering*, 36, 368–376. https://doi.org/10.1016/j.oceaneng.2009.01.004

Hobbs, T. E., Cassidy, J. F., & Dosso, S. E. (2015). Rupture process of the 2012 Mw 7.8 Haida Gwaii earthquake from an empirical green's function method. *Bulletin of the Seismological Society of America*,105(2), 1219–1230. https://doi.org/10.1785/0120140175

Hyndman, R. D. (2015). Tectonics and structure of the queen charlotte fault zone, Haida Gwaii, and large thrust earthquakes. *Bulletin of the Seismological Society of America*, 105(2), 1058–1075. https://doi.org/10.1785/0120140181

James, T., Rogers, G. C., Cassidy, J. F., Dragert, H., Hyndman, R. D., Leonard, L., Nykolaishen, L., Riedel, M., Schmidt, M., & Wang, K. (2013). Field studies target 2012 Haida Gwaii earthquake. *American Geophysical Union*, 94 (22).

Ji, C., Wald, D., & Helmberger, D. (2002). Source description of the 1999 hector mine, California, earthquake, part i: Wavelet domain inversion theory and resolution analysis. *Bulletin of the Seismological Society of America*,92, 1192–1207. https://doi.org/10.1785/0120000916

Kao, H., Shan, S.-J., & Farahbod, A. M. (2015). Source characteristics of the 2012 Haida Gwaii earthquake sequence. *Bulletin of the Seismological Society of America*,105(2), 1206–1218. https://doi.org/10.1785/0120140165

Lapusta, N. et al., (2019), Modeling Earthquake Source Processes: from Tectonics to Dynamic Rupture, *Report to the National Science Foundation*.

Lavallee, D., Liu P., & Archuleta, R. J. (2006) Stochastic model of heterogeneity in earthquake slip spatial distributions. *Geophysical Journal International*, 165: 622–640. 10.1111/j.1365-246X.2006.02943.x

Lay, T., Ye, L., Kanamori, H., Yamazaki, Y., Cheung, K. F., Kwong, K., & Koper, K. D. (2013). The October 28, 2012 mw 7.8 Haida Gwaii under thrusting earthquake and tsunami: Slip partitioning along the queen charlotte fault transgressional plate boundary. *Earth and Planetary Science Letters*, 375, 57–70. https://doi.org/10.1016/j.epsl.2013.05.005

Leonard, L. J., & Bednarski, J. (2014). Field survey following the 28 October 2012 Haida Gwaii tsunami. *Pure and Applied Geophysics*, 171(12), 3467–3482. https://doi.org/10.1007/s00024-014-0792-0

Leonard, L. J., Rogers, G. C., & Mazzotti, S. (2014). Tsunami hazard assessment of Canada. *Natural Hazards*, 70(1). https://doi.org/10.1007/s11069-013-0809-5

Leonard, M. (2010). Earthquake fault scaling: Self-consistent relating of rupture length, width, average displacement, and moment release earthquake fault scaling: Self-consistent relating of rupture length, width, average displacement. *Bulletin of the Seismological Society of America*, 100, 1971–1988. https://doi.org/10.1785/0120090189

Levin, B., & Nosov, M. (2009). Physics of tsunamis. Springer Netherlands

Løvholt, F., Pedersen, G., Bazin, S., Kühn, D., Bredesen, R. E., & Harbitz, C. (2012). Stochastic analysis of tsunami runup due to heterogeneous coseismic slip and dispersion. *Journal of Geophysical Research: Oceans,* 117. https://doi.org/10.1029/2011JC007616

Mai, P. M., & Beroza, G. C. (2002). A spatial random field model to characterize complexity in earthquake slip. *Journal of Geophysical Research: Solid Earth,* 107, ESE 10-1-ESE 10–21. https://doi.org/10.1029/2001JB000588

Mai, P. M., & Thingbaijam, K. (2014). SRCMOD: An online database of finite-fault rupture models. *Seismological Research Letters*, 85, 1348–1357.

Melgar, D., Williamson, A. L., & Salazar-Monroy, E. F. (2019). Differences between heterogenous and homogenous slip in regional tsunami hazards modelling. *Geophysical Journal International*, 219, 553–562. https://doi.org/10.1093/gji/ggz299

Momeni, P., Goda, K., Heidarzadeh, M., & Qin, J. (2020). Stochastic Analysis of Tsunami Hazard of the 1945 Makran Subduction Zone Mw 8.1–8.3 *Earthquakes. Geosciences*, 10(11), 452. doi:10.3390/geosciences10110452

Mori, N., Goda, K., & Cox, D. (2018). Recent process in probabilistic tsunami hazard analysis (PTHA) for mega thrust subduction earthquakes [Series Title: Advances in Natural and Technological Hazards Research]. The 2011 japan earthquake and tsunami: Reconstruction and restoration (pp. 469–485). *Springer International Publishing*. https: //doi.org/10.1007/978-3-319-58691-5 27

Mori, N., Mai, P. M., Goda, K., Yasuda, T. (2017a). Tsunami inundation variability from stochastic rupture scenarios: Application to multiple inversions of the 2011 Tohoku, Japan earthquake. *Coastal Engineering,* 127, 88-105. https://doi.org/10.1016/j.coastaleng.2017.06.013

Mori, N., Muhammad, A., Goda, K., Yasuda, T., & Ruiz-Angulo, A. (2017b). Probabilistic tsunami hazard analysis of the pacific coast of Mexico: Case study based on the 1995 Colima earthquake tsunami. *Frontiers in Built Environment*, 3. https://doi.org/10.3389/fbuil.2017.00034

Motazedian, D., Zhang, Y., Ma, S., & Chen, Y. (2016). Further studies on the focal mechanism and source rupture process on the 2012 Haida Gwaii, Canada, 7.8 moment magnitude. *Canadian Journal of Earth Sciences*, 53, 129–139. https://doi.org/10.1139/cjes2015-0119

Mueller, C., Power, W., Fraser, S., & Wang, X. (2015). Effects of rupture complexity on local tsunami inundation: Implications for probabilistic tsunami hazard assessment by example. *Journal of Geophysical Research: Solid Earth*, 120, 488–502. https://doi.org/10.1002/2014JB011301

Murotani, S., Satake, K. & Fujii, Y. (2013) Scaling relations of seismic moment, rupture area, average slip, and asperity size for M9 subduction-zone earthquakes, *Geophysical Research Letters*, 40(19), 5070-5074. https://doi.org/10.1002/grl.50976

Nakata, K., Hayashi, Y., Tsushima, H. Fujita, K., Yoshida, & Y. Katsumata A. (2019). Performance of uniform and heterogeneous slip distributions for the modeling of the November 2016 off Fukushima earthquake and tsunami, Japan. *Earth Planets Space*, 71**,** 30 https://doi.org/10.1186/s40623-019-1010-1

Nykolaishen, L., Dragert, H., Wang, K., James, T. S., & Schmidt, M. (2015). GPS observations of crustal deformation associated with the 2012 Mw 7.8 Haida Gwaii earthquake. *Bulletin of the Seismological Society of America*, 105(2), 1241–1252. https://doi.org/10.1785/0120140177

Oglesby, D. D., & Day, S. M. (2002) Stochastic Fault Stress: Implications for Fault Dynamics and Ground Motion. *Bulletin of the Seismological Society of America*; 92 (8), 3006–3021. https://doi.org/10.1785/0120010249

Okada, Y. (1985). Surface deformation due to shear and tensile faults in a half-space. *Bulletin of the Seismological Society of America*, 75(4), 1135-1154. https://doi.org/10.1785/BSSA0750041135

Park, H., Cox, D. T., Alam, M. S., & Barbosa, A. R. (2017). Probabilistic seismic and tsunami hazard analysis conditioned on a megathrust rupture of the Cascadia subduction zone. *Frontiers in Built Environment*, 3. https://doi.org/10.3389/fbuil.2017.00032

Petersen M. D., Frankel A. D., Harmsen S. C., Mueller C.S., Haller K. M., Wheeler R. L., Wesson R. L., Zeng Y., Boyd O. S., Perkins D. M., Lucco N., Field E. H., Willis C. J., Ruskstales. (2008). Documentation for the 2008 Update of the United States National Seismic Hazard Maps, *United States Geological Service*, Open-File Report 2008-1128. https://doi.org/10.3133/ofr20081128

Priest, G. R., Myers, E., Baptista, P., A.M. & Fleuck, Wang, K., & Peterson, C. (2000). Source simulation for tsunamis; lessons learned from fault rupture modeling of the Cascadia subduction zone, North America, *Science of Tsunami Hazard*, 18, 77–105.

Rohr, K. M. M. (2015). Plate boundary adjustments of the southern most queen charlotte fault. *Bulletin of the Seismological Society of America*, 105, 8147–8172. https://doi.org/10.1785/0120140162.

Rabinovich, A.B., Thomson, R.E., Titov, V.V., Stepheson, F.E., & Rogers, G.C. (2008). Locally generated tsunamis recorded on the coast of British Columbia. *Atmosphere-Ocean,* 46(3), 343-360 doi:10.3137/ao.460304

Sánchez-Linares, C., de la Asunción, M., Castro, M.J., Gonzalez-Vida, J.M., & Macias, J., Mishra S. (2016). Uncertainty quantification in tsunami modeling using multi-level Monte Carlo finite volume method. *Journal of Mathematics in Industry*, 6**,** 5 https://doi.org/10.1186/s13362-016-0022-8

Satake, K., Fujii, Y., Harada, T., & Namegaya, Y. (2013). Time and space distribution of coseismic slip of the 2011 Tohoku earthquake as inferred from tsunami waveform data time and space distribution of coseismic slip of the 2011 Tohoku earthquake. *Bulletin of the Seismological Society of America,* 103. https://doi.org/10.1785/0120120122

Satake, K., Wang, K., & Atwater, B. F. (2003). Fault slip and seismic moment of the 1700 Cascadia earthquake inferred from Japanese tsunami descriptions. *Journal of Geophysical Research*, 108, 2535. https://doi.org/10.1029/2003JB002521

Schmedes, J., Archuleta, R. J., Lavallée, D., (2013) A kinematic rupture model generator incorporating spatial interdependency of earthquake source parameters, *Geophysical Journal International*, 192 (3), 1116–1131. https://doi.org/10.1093/gji/ggs021

Selva, J., Tonini, R., Molinari, I., Tiberti, M., Romano, F., Grezio, A., Melini, D., Piatanesi, A., Basili, R., & Lorito, S. (2016). Quantification of source uncertainties in seismic probabilistic tsunami hazard analysis (SPTHA). *Geophysical Journal International*, 205, 1780–1803. https://doi.org/10.1093/gji/ggw107

Shao, G., & Ji, C. (2012). Preliminary result of the oct 28, 2012 Mw 7.72 Canada. http://www. geol.ucsb.edu/faculty/ji/big earthquakes/2012/10/canada.html (accessed: 20.05.2021)

Shuto, N. (1991) Numerical simulation of tsunamis — Its present and near future. *Natural Hazards*, 4**,** 171–191. https://doi.org/10.1007/BF00162786

Steketee, J.A. (1958) On Volterra's dislocations in a semi-infinite elastic medium, *Canadian Journal of Physics*, 36, 192-205, https://doi.org/10.1139/p58-024

Strasser, F. O., Arango, M. C., & Bommer; J. J. (2010) Scaling of the source dimensions of interface and intraslab subduction-zone earthquakes with moment magnitude. *Seismological Research Letters*, 81 (6), 941–950. https://doi-org.proxy1.lib.uwo.ca/10.1785/gssrl.81.6.941

Suppasri, A., Imamura, F., & Koshimura, S. (2010). Effects of the rupture velocity of fault motion, ocean current and initial sea level on the transoceanic propagation of tsunami. *Coastal Engineering Journal*, 52, 107–132. https://doi.org/10.1142/S0578563410002142

Szeliga, W. (2013). 2012 Haida Gwaii quake: Insight into Cascadia’s subduction extent. *Eos, Transactions American Geophysical Union*, 94, 85–86.

Takabatake, T., St-Germain, P., Nistor, I., Stolle, J., & Shibayama, T. (2019). Numerical modelling of coastal inundation from Cascadia subduction zone tsunamis and implications for coastal communities on western Vancouver Island, Canada. *Natural Hazards*, 98(1), 267–291. https://doi.org/10.1007/s11069-019-03614-3

Tanioka, Y., & Satake, K. (1996). Tsunami generation by horizontal displacement of ocean bottom. *Geophysical Research Letters*, 23, 861–864. https://doi.org/10.1029/96GL00736

Titov, V., Rabinovich, A. B., Mofjeld, H. O., Thomson, R. E., & Gonzalez, F. I. (2005). The global reach of the 26 December 2004 Sumatra tsunami. *Science*, 309, 2045–2048. https: //doi.org/10.1126/science.1114576

Tréhu, A. M., Scheidhauer, M., Rohr, K. M. M., Tikoff, B., Walton, M. A. L., Gulick, S. P. S., &Roland, E. C. (2015). An abrupt transition in the mechanical response of the upper crust to transpression along the queen charlotte fault an abrupt transition in the mechanical response of the upper crust to transpression along the QCF. *Bulletin of the Seismological Society of America*, 105, 1114–1128. https://doi.org/10.1785/0120140159

Yolsal-Çevikbilen, S. & Taymaz, T. (2012) Earthquake source parameters along the Hellenic subduction zone and numerical simulations of historical tsunamis in the Eastern Mediterranean. *Tectonophysic*. 536–537, 61-100. https://doi.org/10.1016/j.tecto.2012.02.019

Walsh, T., Caruthers, C., Heinitz, A., Mayers, E., Baptista, A., Erdakos, G., & Kamphaus, R. (2000). Tsunami hazard map of the southern Washington coast–modeled tsunami inundation from a Cascadia subduction zone earthquake, *Washington State Department of Natural Resources*, geologic map GM-49.

Walton, M. L., Roland, E., S.S., G., G.L., H., Christeson, G., & H.J., V. A. (2013). New mapping and structural constraints on the queen charlotte-Fairweather fault system, southeast Alaska. *American Geophysical. Union: Annual Meeting, San Francisco, California,* December 2013.

Wang, K., He, J., Schulzeck, F., Hyndman, R., & Riedel, M. (2015). Thermal condition of the 27 October 2012 mw 7.8 Haida Gwaii subduction earthquake at the obliquely convergent queen charlotte margin. *Bulletin of the Seismological Society of America*, 105, 1290– 1300. https://doi.org/10.1785/0120140183

Wang, X., & Liu, P. L.-F. (2006). An analysis of 2004 Sumatra earthquake fault plane mechanisms and Indian ocean tsunami. *Journal of Hydraulic Research*, 44, 147–154. https: //doi.org/10.1080/00221686.2006.9521671

Wei, S. (2012). Oct./28/2012 (Mw 7.8), Masset, Canada. source models of large earthquakes. http://www.tectonics.caltech.edu/sliphistory/2012 Masset/index.html (accessed: 20.05.2021)

Wells, D. L., & K. J. Coppersmith (1994). New empirical relationships among magnitude, rupture length, rupture width, rupture area, and surface displacement. *Bulletin of the Seismological Society of America*. 84 974–1002.

Appendix A

Offshore results from literature models

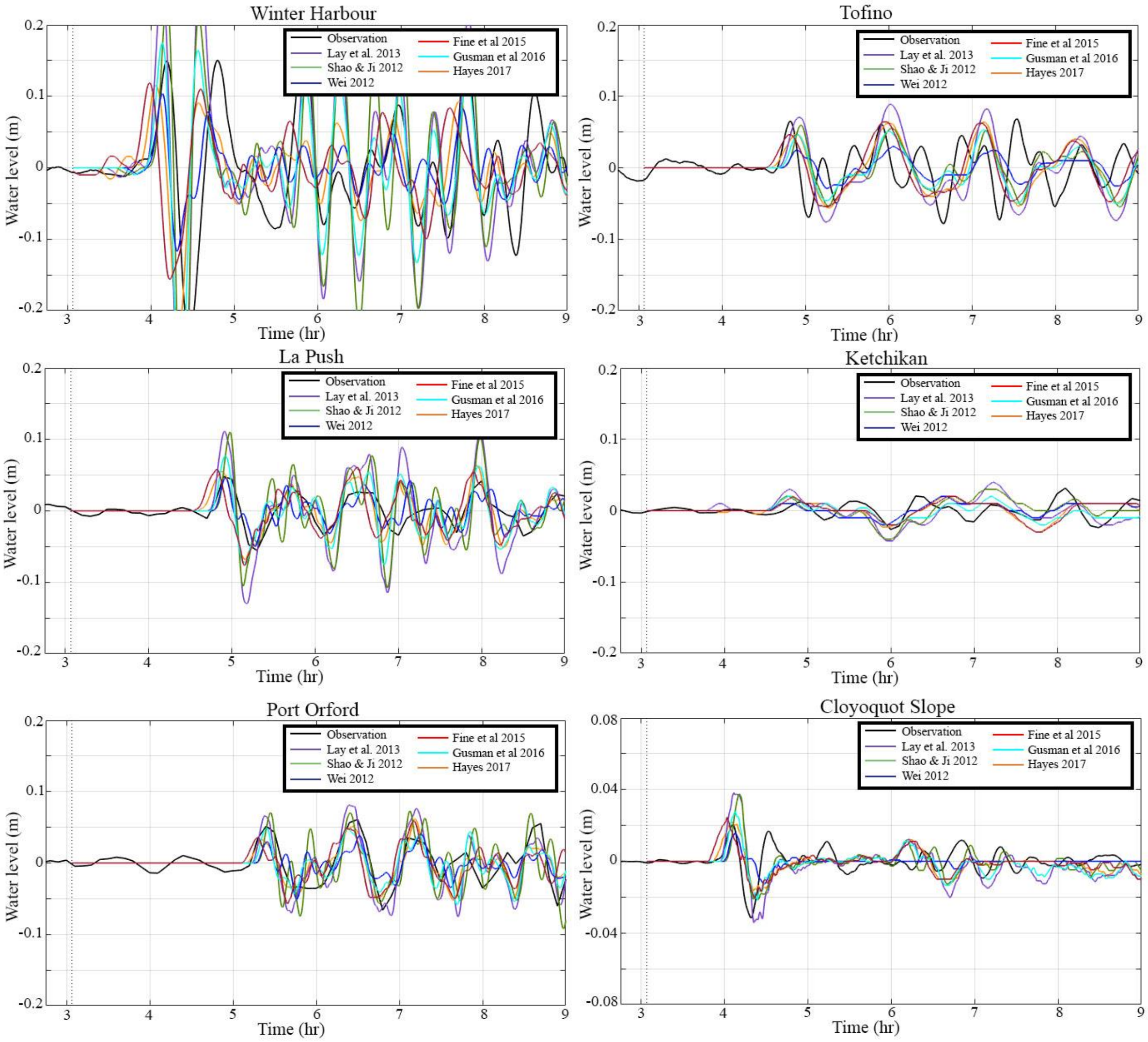

Appendix A:1 Time histories of the six literature models against observations

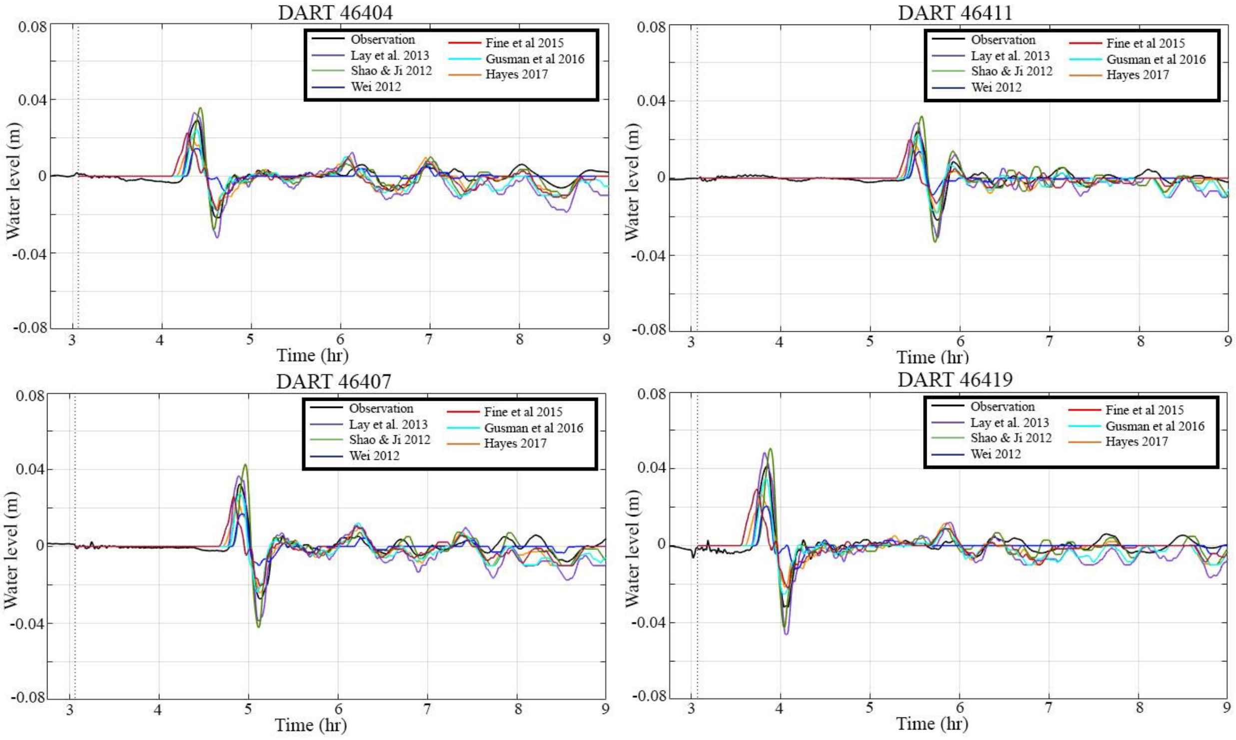

Appendix A:2 Time histories of the six literature models against observations

Lay et al. (2013)

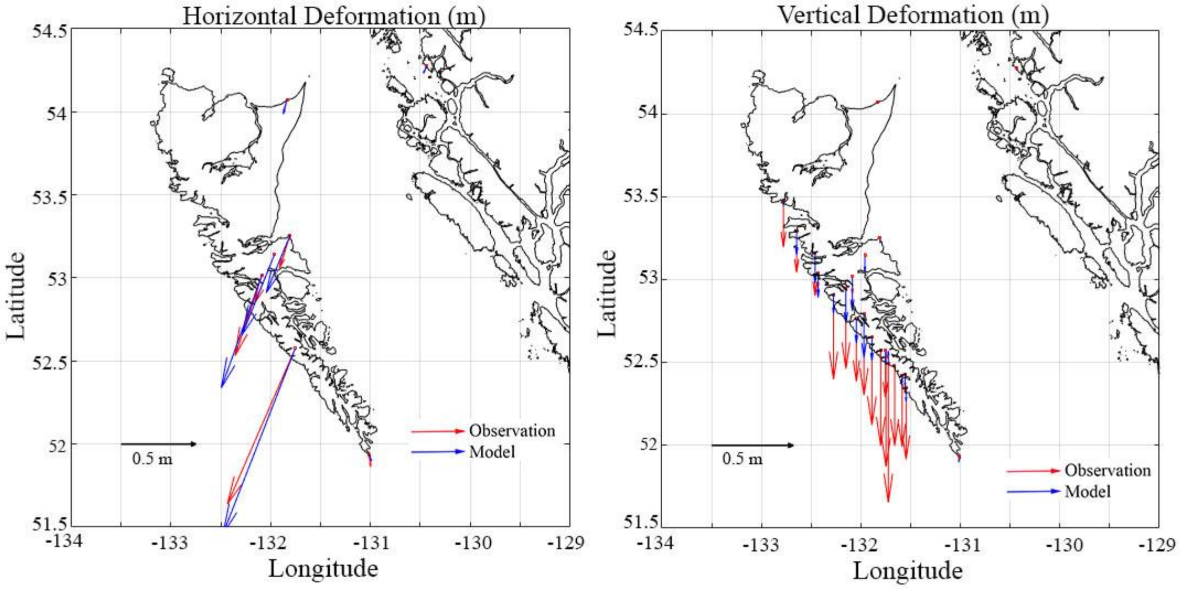

Hayes (2017)

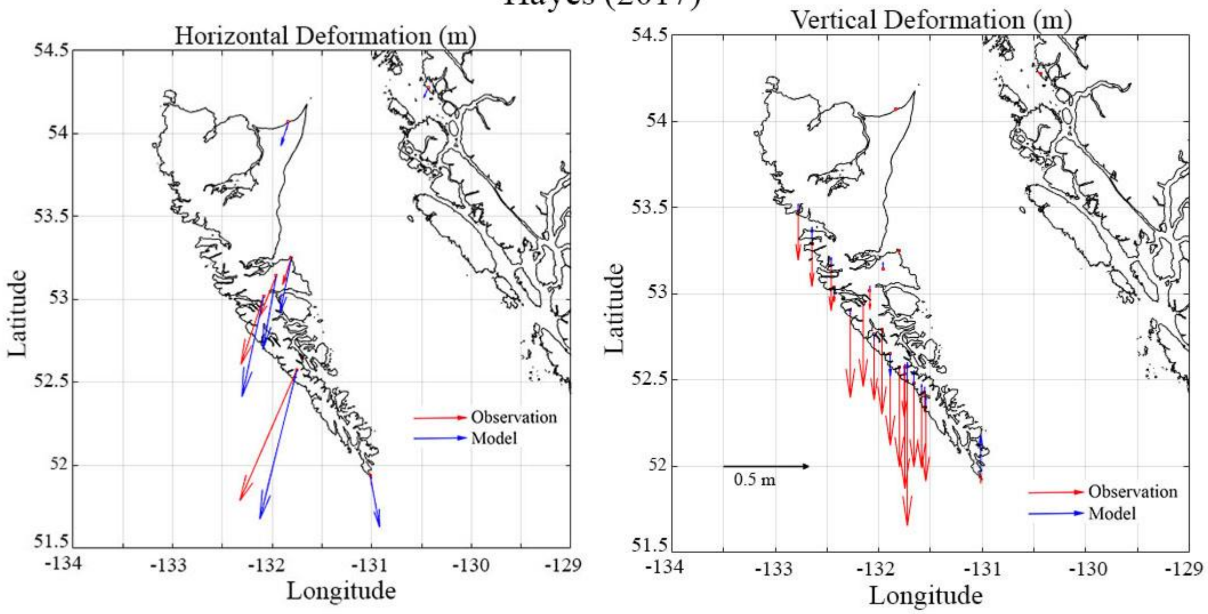

Appendix A: 3 Horizontal and Vertical deformation vectors of the observations and source models from the literatures

Wei (2012)

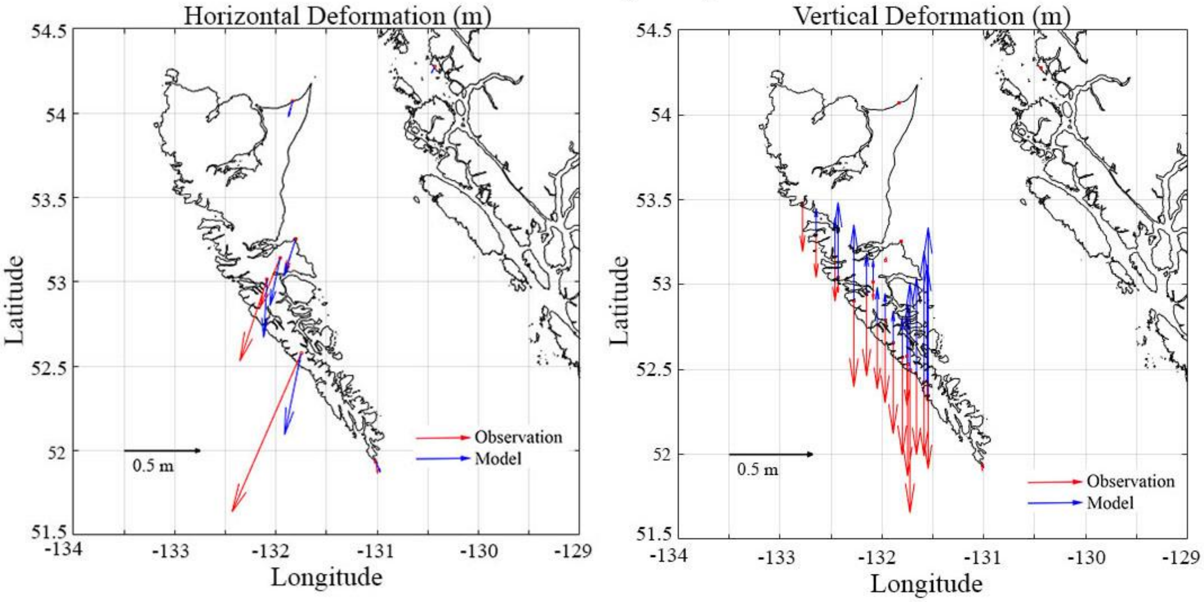

Fine et al. 2015 [Hayes (2013)]

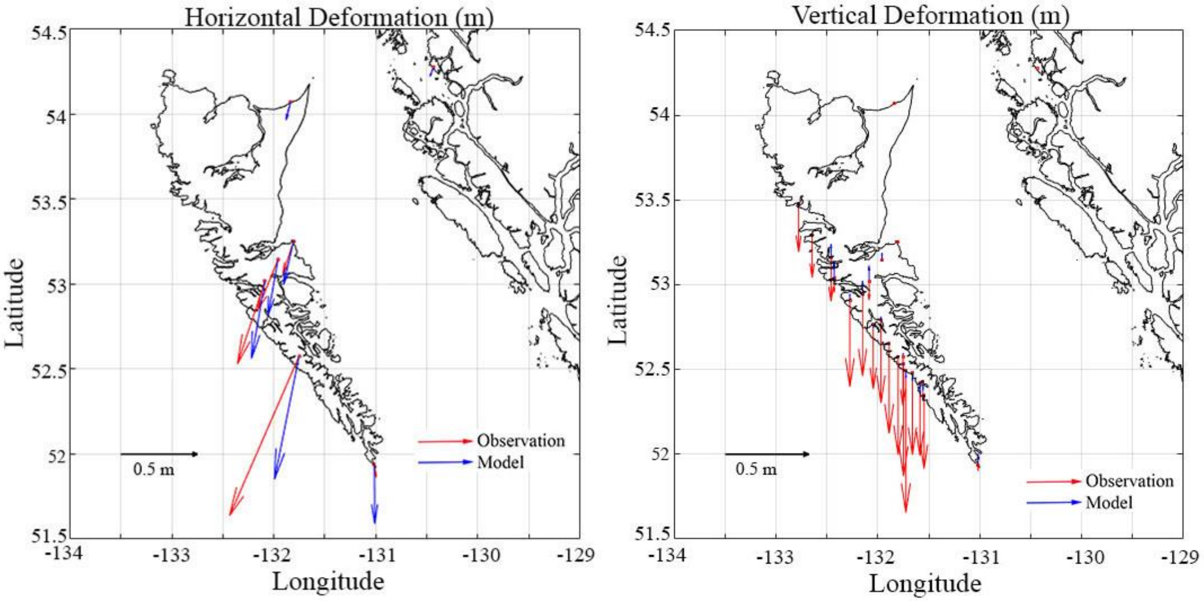

Appendix A: 4 Horizontal and Vertical deformation vectors of the observations and source models from the literatures

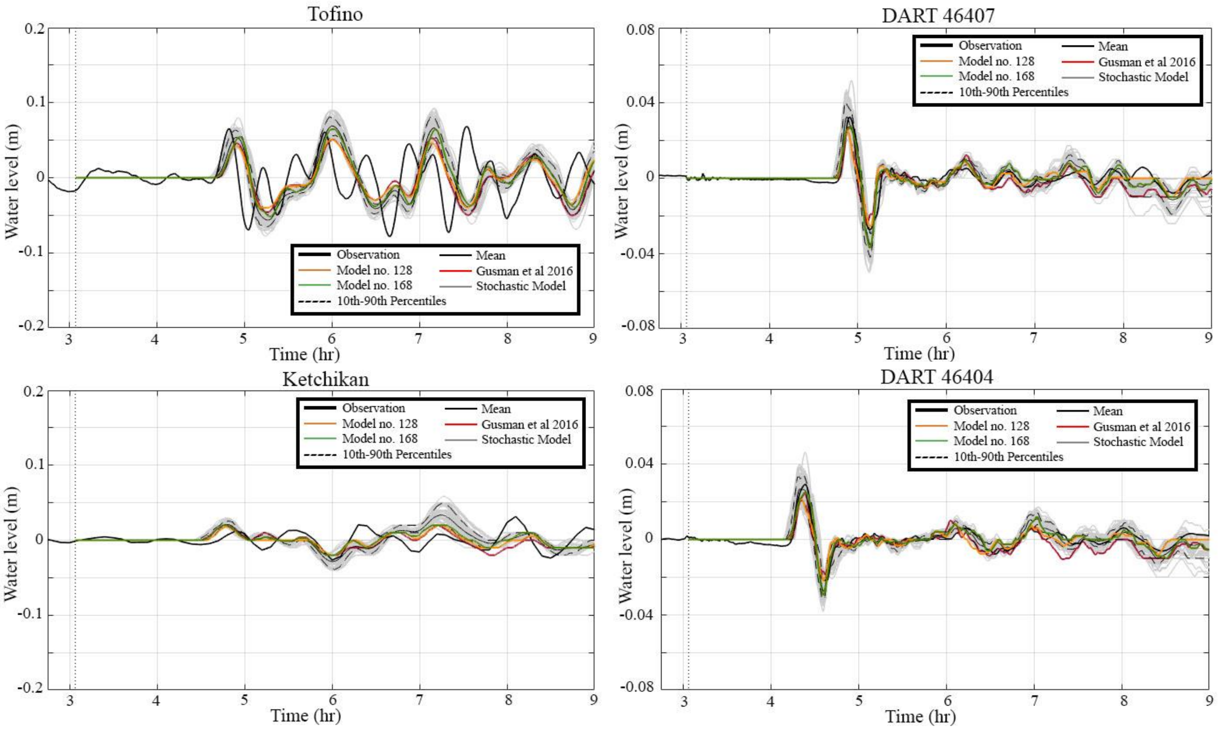

Appendix A: 6 Tsunami waveforms at Tofino, Ketchikan, DART 46404, DART 46407 stations and literature models

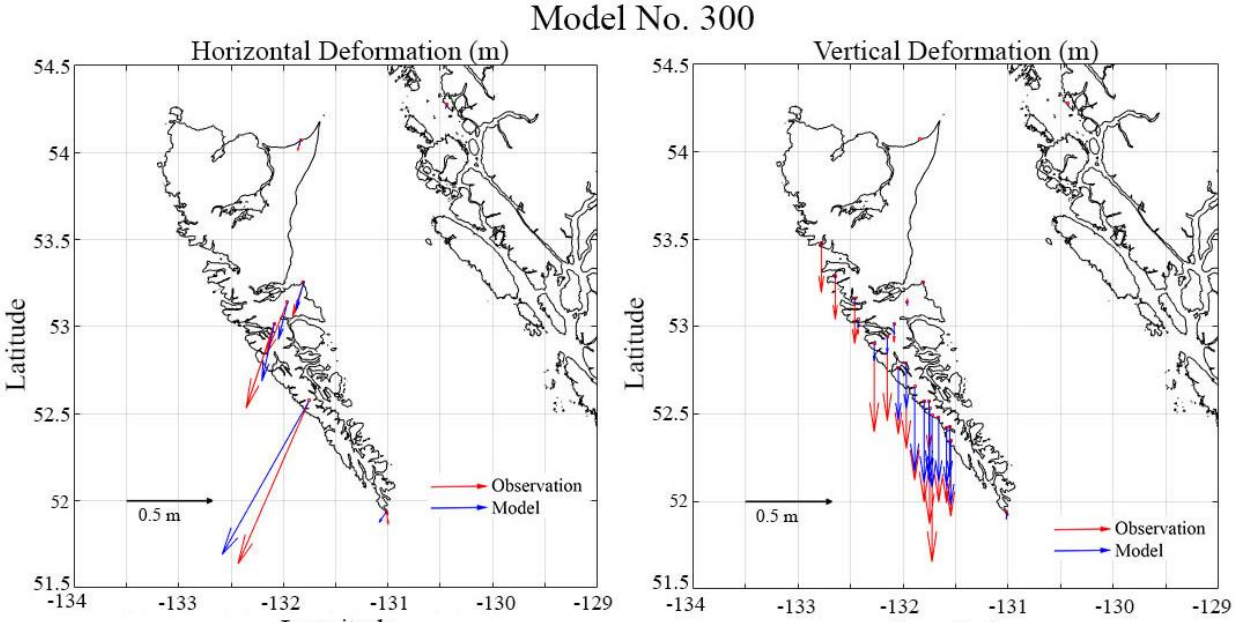

Appendix A: 5 Horizontal and vertical deformations of observations and stochastic models

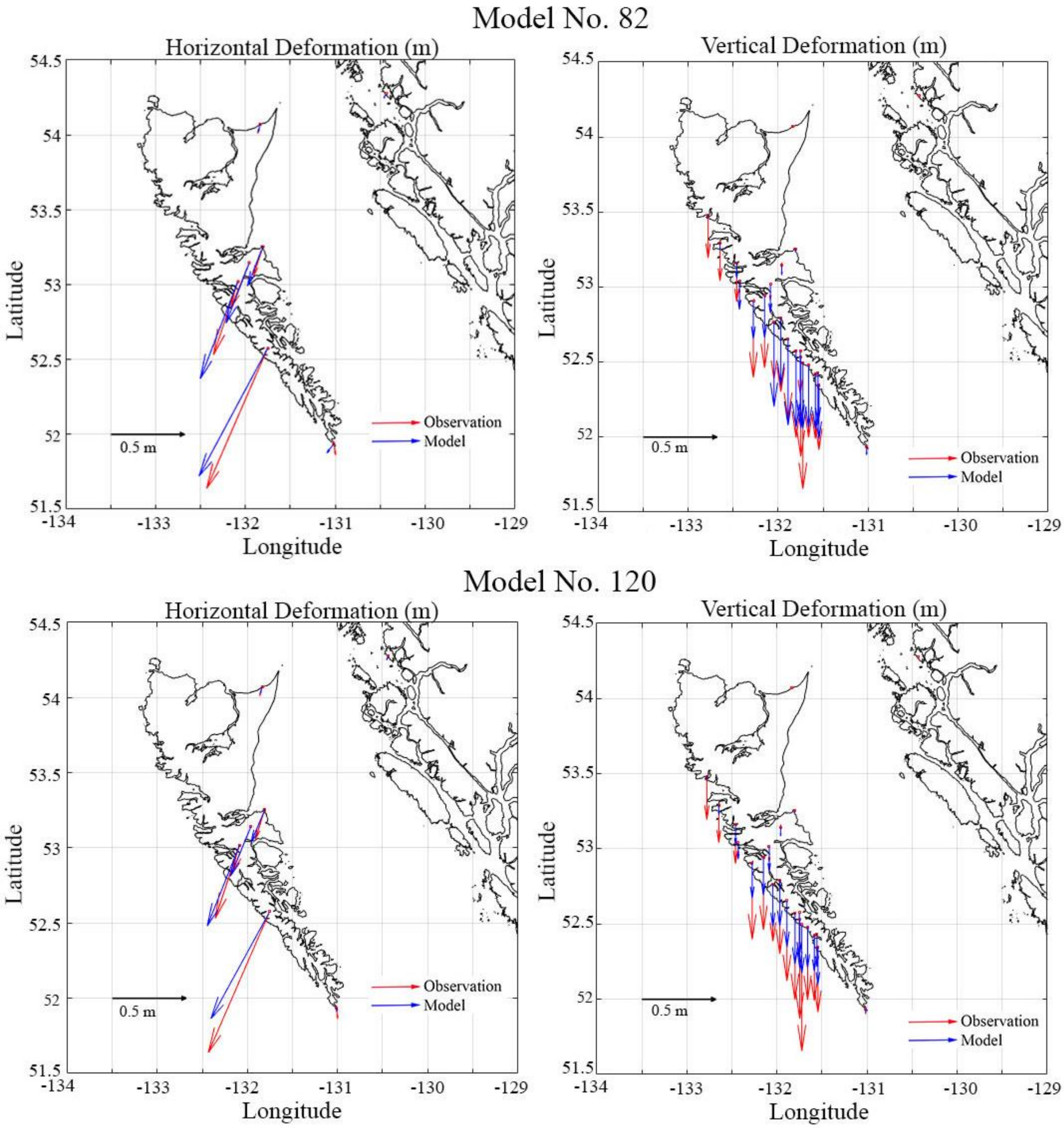

Appendix A: 7 Horizontal and vertical deformations of observations and stochastic models

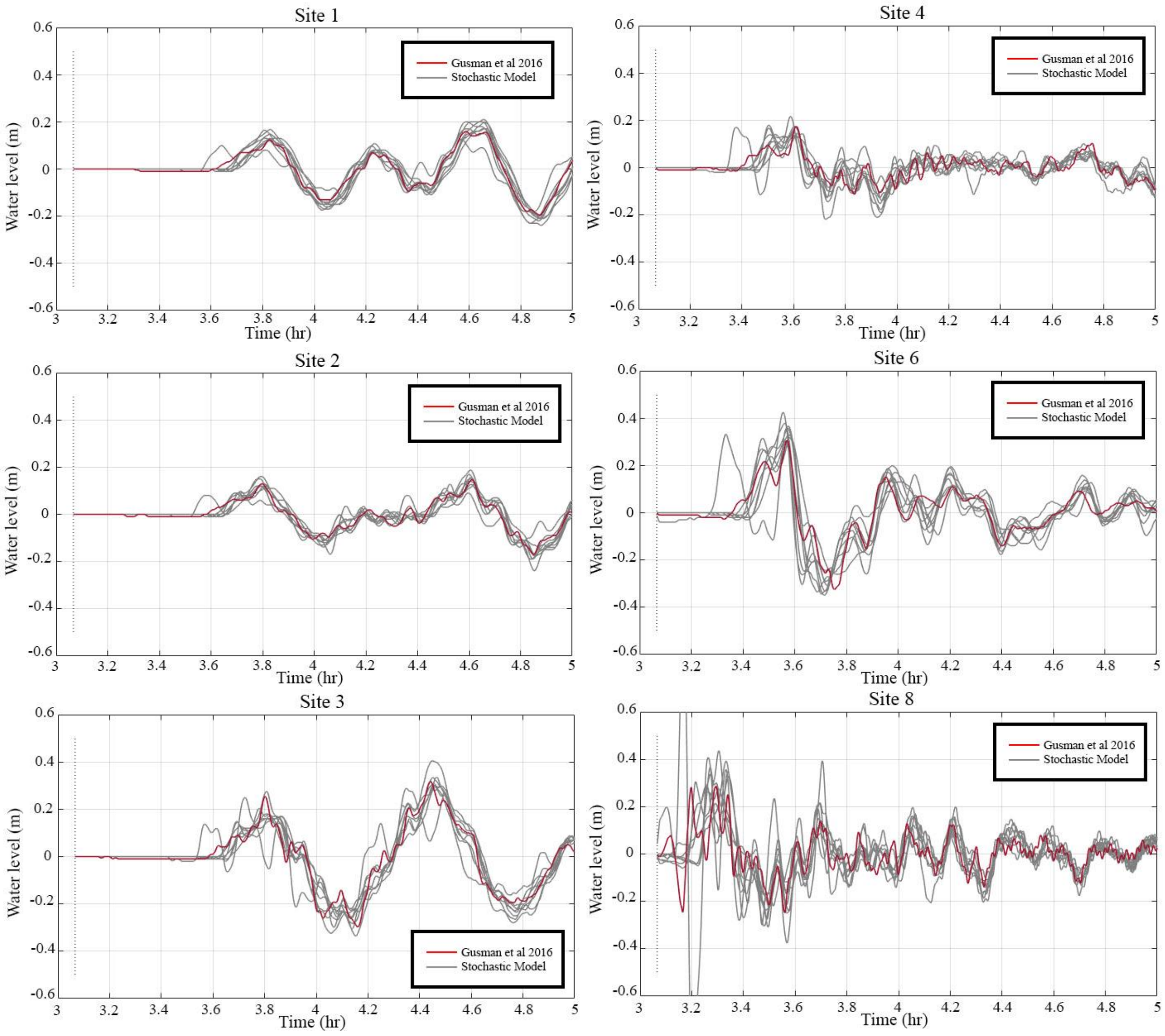

Appendix A:8 Time histories of tsunami waves for sites 1, 2, 3, 4, 6, 8

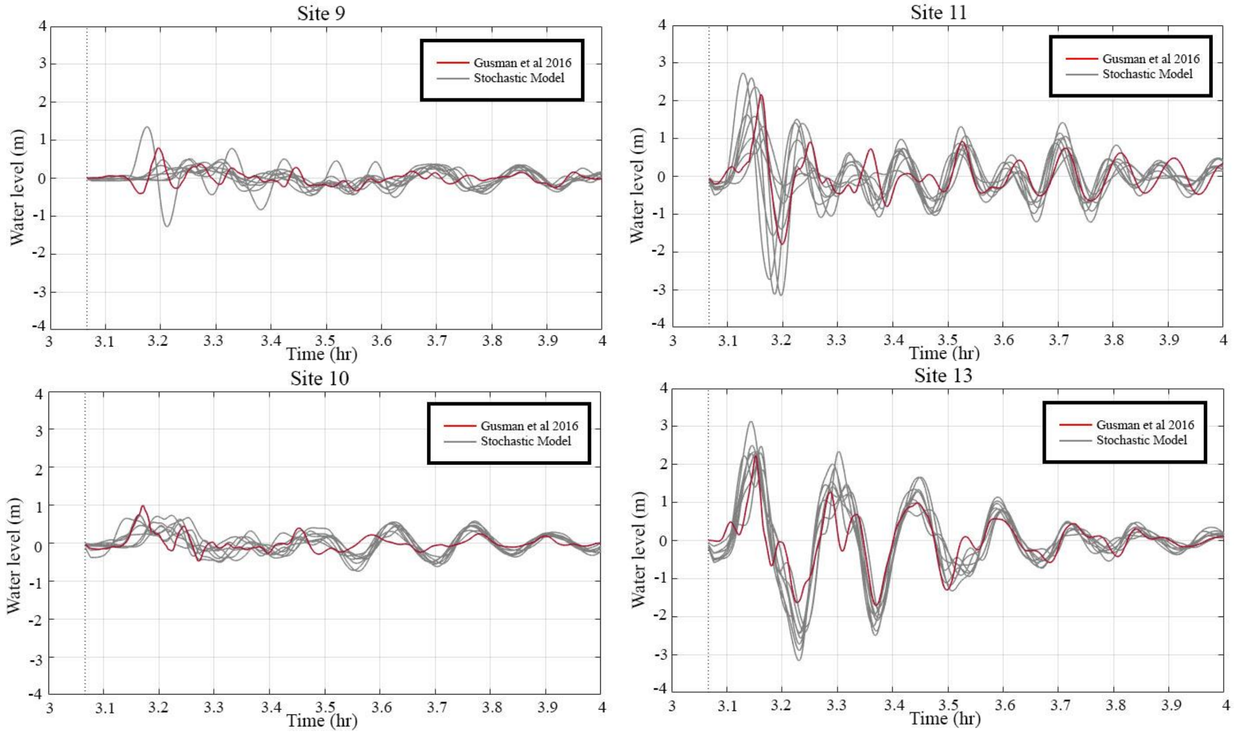

Appendix A:9 Time histories of tsunami waves for sites 9, 10, 11, 13

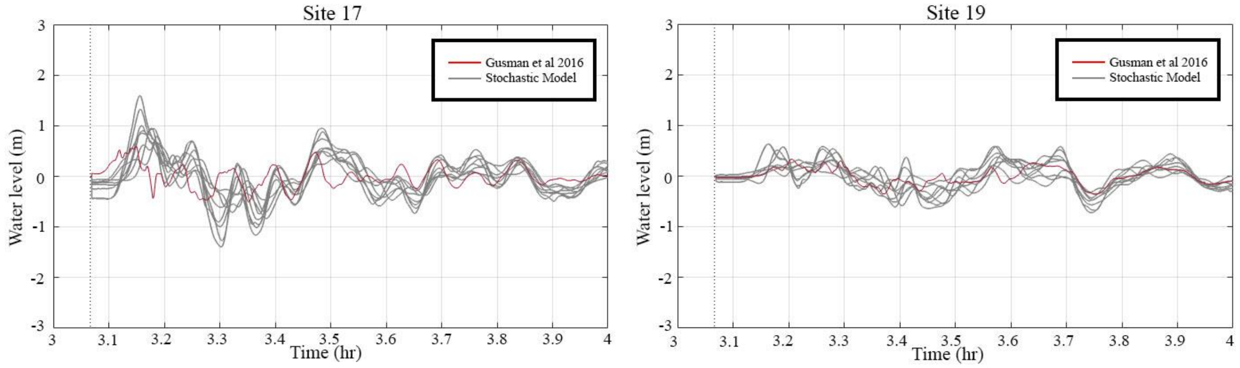

Appendix A:10 Time histories of tsunami waves for sites 17-19

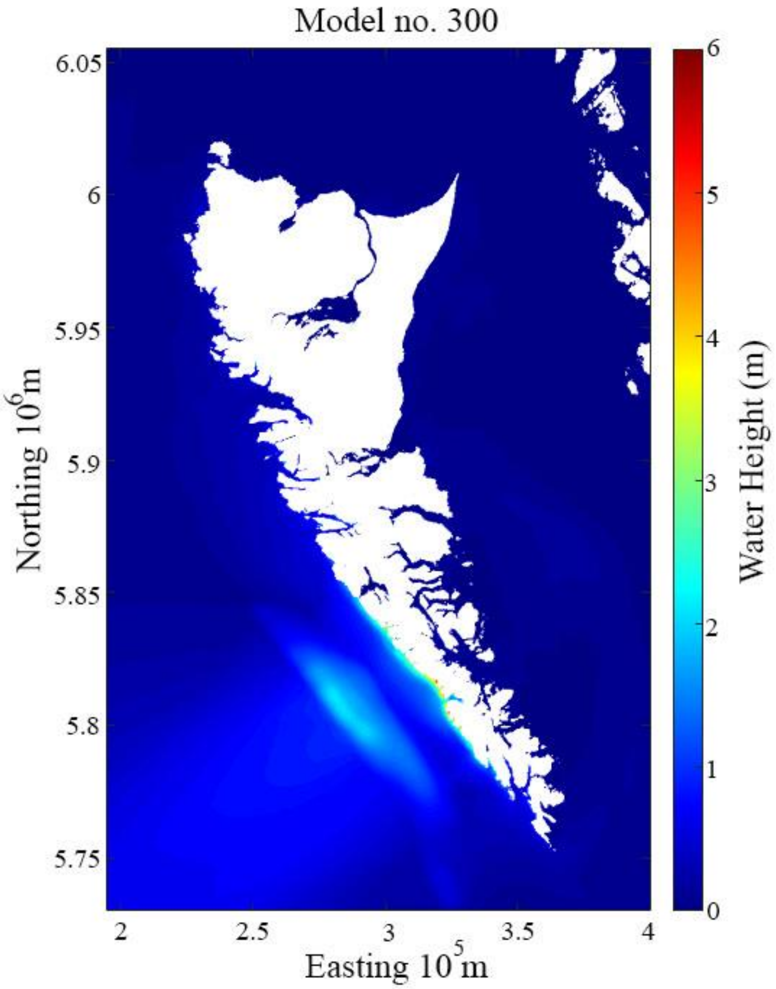

Appendix A:11 Maximum wave height for the Haida

Appendix A:12 Run-up values for six literature sources along the Haida Gwaii region

Sites	Hayes (2017)	Lay et al. (2013)	Sha & Ji (2012)	Wei (2012)	Gusman et al. (2016)	Hayes (2013) Fine et al. (2015)
	Run-up (m)	Run-up (m)	Run-up (m)	Run-up (m)	Run-up (m)	Run-up (m)
Otard Bay	0.308	1.24	1.147	0.313	0.860	0.296
Seal Inlet	0.304	0.657	0.379	0.162	0.224	0.190
Gudal Bay	1.374	2.927	1.008	1.186	0.688	0.805
Saunders Island	0.982	2.146	0.636	0.270	1.161	0.283
Davidson Inlet	1.705	4.209	0.934	0.067	4.198	1.245
Sunday Inlet	3.186	4.061	3.055	0.209	3.191	1.826
Kwoon Cove	3.604	5.041	2.327	0.681	3.296	2.710
Pocket Inlet	3.433	5.760	2.621	0.570	3.238	2.721
Mike Inlet	2.513	6.244	2.336	0.573	2.535	4.561
Puffin Cove	1.325	5.242	0.386	0.231	1.483	4.137
Goski Bay	1.003	2.359	0.831	0.830	1.204	1.618
Staki Bay	0.662	1.009	0.974	0.676	0.725	1.320
Louscoone Inlet	0.427	0.623	0.713	0.358	0.397	0.762
Ta'dasl	0.399	0.729	0.913	0.340	0.512	1.516
Gilbert Bay	0.626	0.919	1.441	0.893	0.913	1.639

Appendix B

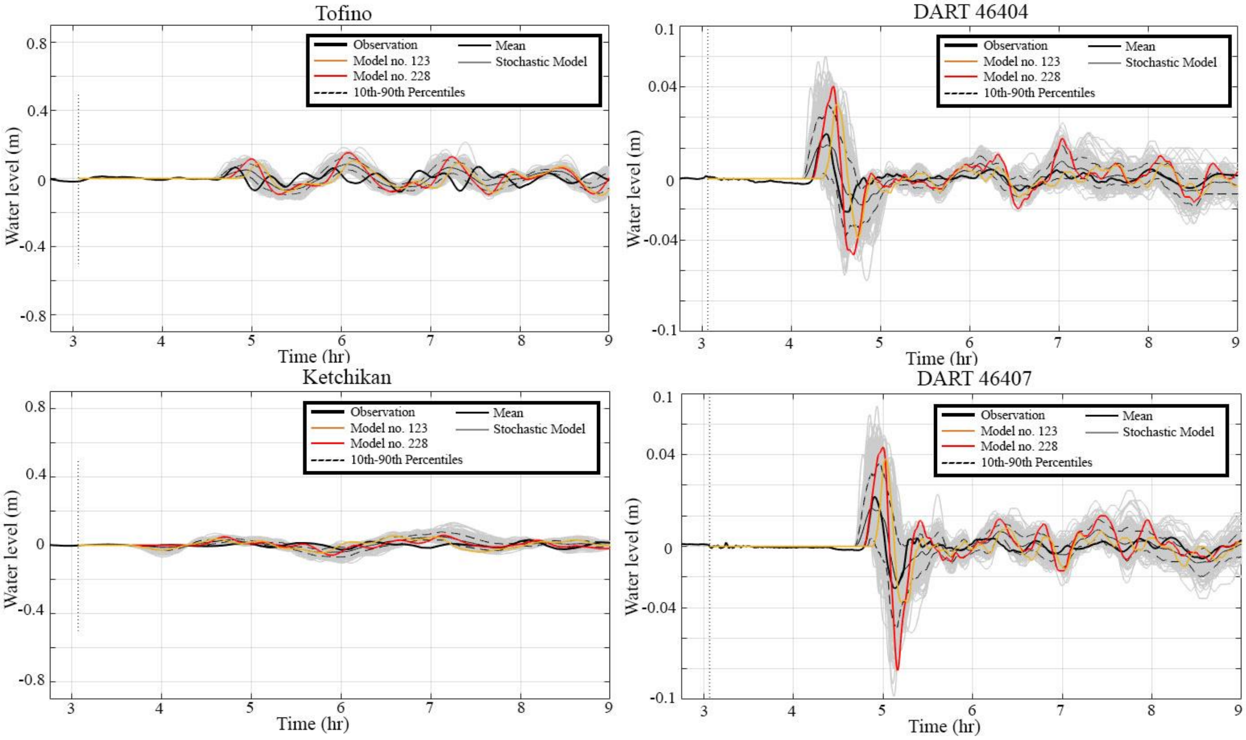

Appendix B:1 Comparison of time histories of tsunami wave for the 326 stochastic models (mean, 90th and 10th percentile) and observations

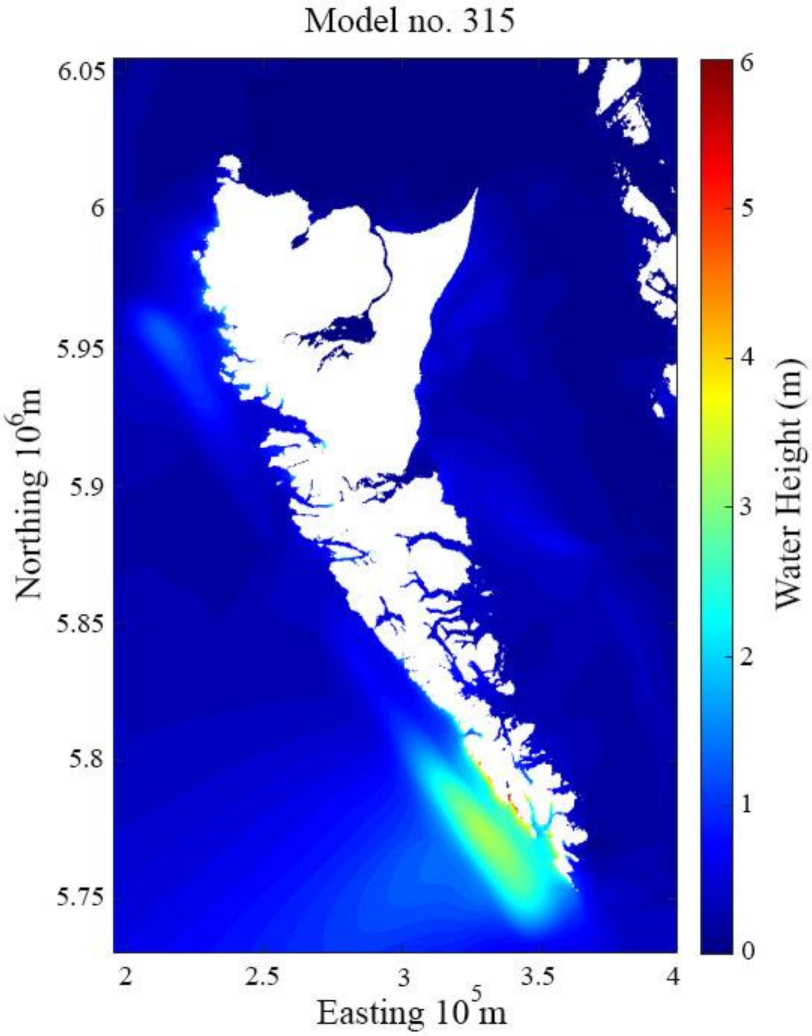

Appendix B:2 Maximum wave height for the Haida Gwaii region

Curriculum Vitae

Name:	Karina Martinez Alcala
Post-secondary Education and Degrees:	Universidad de Guanajuato Guanajuato, Guanajuato, Mexico 2015-2018 B.A.
Honours and Awards:	Geophysics Travel Scholarship The University of Western Ontario 2021
	Best Poster Presentation Award 30th International Tsunami Symposium at Sendai Japan 2021
Related Work Experience	Teaching Assistant The University of Western Ontario 2019-2021